A STUDY OF LOCALIZED CORROSION IN SUPER MARTENSITIC STAINLESS STEEL WELDMENTS

by

Jakob Enerhaug

A thesis submitted to
The Norwegian University of Science and Technology (NTNU) in partial fulfilment of the requirements for the degree of

Doktor Ingeniør

Trondheim,

May 2002

URN:NBN:no-2356

PREFACE

This work has been carried out at the Department of Machine Design and Materials Technology, The Norwegian University of Science and Technology. The author started on the doctor programme in autumn 1998.

Chief engineer Per Egil Kvaale, Statoil, initiated the work. The work has been financed by Den norske stats oljeselskap (Statoil) and by the EU-programme JOTSUP.

The main results presented in this thesis have been publish, or are in the process of being published, in international journals and conference proceedings, including Science and Technology of Welding and Joining, the Journal of the Electrochemical Society, NACE Corrosion/02, Denver, USA, 6-14 April 2002, and Supermartensitic Stainless Steel 2002, Brussels, Belgium, 3-4 October 2002.

Trondheim, 2002-05-28

Jakob Enerhaug

ACKNOWLEDGEMENTS

During the course of this work Professor Unni Steinsmo and Professor Øystein Grong have been my thesis supervisors. I am very grateful for their interest and active role in the project, as well as encouragement in all respect. The author also acknowledges the financial support from Statoil and from JOTSUP.

Thanks to Chief engineer Per Egil Kvaale (Statoil) for giving me the opportunity to carry out this work, to Specialist Stein Olsen (Statoil) for support and valuable advices, and to dr.ing. Alf Daaland (Statoil) for his support. I would also like to thank my friends and colleagues at Statoil and at SINTEF Materials Technology for many useful discussions during the course of this work.

In conjunction with this work, I have had the pleasure to supervise three students during their fulfilment of their graduate siv.ing. thesis at NTNU and two students during their fulfilment of their graduate ing. thesis at Høgskolesenteret i Trondheim. Torgeir Wenn (Statoil), Rune Østhus, Øystein Sævik, Monica Engen and Laila Olderøien are all acknowledged for their contributions.

I am also very grateful to Møyfrid, Elisabeth, Hanna and Solveig for their support and prayers over the last years. Most of all, I want to thank my lord and saviour Jesus Christ for his abundantly grace towards me. You gave me hope and peace also in the very difficult times.

ABSTRACT

This doctoral thesis is concerned with pitting corrosion in super martensitic stainless steel (SMSS) weldments in slightly sour service. The main objective with the present thesis has been to find out why pitting corrosion occurs in the heat affected zone (HAZ) at ambient rather than at elevated temperatures and how the corrosion mechanism depends on the welding process.

The thesis is divided into six parts. Part I gives a general introduction to martensitic stainless steels, focusing on the metallurgical and corrosion properties.

Part II is concerned with the conditions for initiating of pitting corrosion in two SMSS weldments. Optical microscopy in combination with sputtered neutral mass spectrometry has been used to examine the conditions, and it is shown that the corrosion resistance depends mainly on the nature of the surface oxide and less on the underlying microstructure. In the absence of H_2S the initiation is associated with spalling of the iron-enriched chromium oxide within a narrow region approximately 6mm from the fusion boundary, where the contaminated oxide layer is thinnest. As H_2S is introduced, the region close to the fusion boundary become susceptible to localised corrosion because of the more extensive metal oxidation. Thus, the high temperature oxidation and iron oxide scale formation accompanying the welding operation appears to be the main factor affecting the pitting corrosion initiation in SMSS weldments.

In Part III, a comparative study of the dissolution and repassivation behaviour of a Fe-12.3Cr-6.5Ni-2.6Mo SMSS alloy and other stainless grades has been carried out. The SMSS alloy is characterised by means of the so-called "artificial pit technique", and a diffusion model has been developed and employed for calculation of the pit surface concentration of dissolved species during the potential step experiments. For concentrations close to the saturation level, the dissolution kinetics are adequately described by a Tafel slope of approximately 57mV/dec and a current density of 0.5mA/cm^2 at –300mV SCE. On the other hand, repassivation of the active pit surface occurs when the concentration of the dissolved species drops below 30% of the saturation value. Based on a comparison with relevant literature data it is concluded that the observed response of the SMSS to localised corrosion is similar to that reported for other high-alloyed steels. This result is to be expected if the dissolution and repassivation kinetics are controlled by the content of Cr, Ni and Mo in the parent material.

In Part IV, the specific effects of H_2S on the pitting corrosion behaviour of a Fe-12.3Cr-6.5Ni-2.6Mo SMSS alloy have been examined by means of the

"artificial pit technique". Addition of a critical amount of H_2S is found to hinder repassivation and accelerate active dissolution in the SMSS pit within the stability domain of the adsorbed sulphur. Above the redox potential of H_2S/S, the effect of H_2S is found to cease, whereby dissolution and repassivation kinetics similar to H_2S-free solutions are observed. Activated pits show no signs of repassivation, not even at low surface concentration of dissolved species. It is concluded that the resistance to pitting corrosion depends both on the potential and the H_2S concentration and the effect of H_2S is most significant at low potentials.

Part V is concerned with the occurrence and appearance of pitting corrosion in SMSS girth welds in the presence of H_2S. Galvanostatic and potentiodynamic measurements were carried out at ambient temperature and pressure, using both a deaerated solution and a 1m*M* H_2S solution. In conjunction with this study, a descriptive pitting corrosion model is proposed to explain the effect of the root surface condition and the role of H_2S. The oxidized pipe surface close to the fusion boundary is found to be extremely vulnerable to pitting corrosion in the presence of H_2S, while the same zone appears to behave inert in the deaerated solution. In the latter case the oxidised surfaces were found to repassivate. In the H_2S solution, localized corrosion occurred in the most oxidized region of the HAZ, about 0 to 3mm from the fusion boundary. Moreover, it was found that a modification of the as-welded root surface by grinding hindered any initiation of pitting corrosion in this region, again highlighting the important role which high temperature oxidation and oxide scale formation play in controlling the corrosion properties of SMSS weldments.

Finally, in Part VI of the thesis, the practical implications of the above findings for choice and development of relevant corrosion test procedures have been considered. A key issue here is the effect of pre-exposure on the corrosion resistance of SMSS weldments in the presence of H_2S. Pre-exposures have been simulated in test solutions resembling the conditions in a flowline. It is shown that the quality (i.e. passivity) of SMSS root surfaces can be largely improved by the use of an appropriate pre-exposure procedure. It is therefore recommended that all samples in the future are pre-exposed to an H_2S-free solution before they are subjected to actual corrosion testing in solutions containing H_2S to avoid pitting corrosion in the oxidized part of HAZ. This is deemed to be important in order to achieve realistic results.

TABLE OF CONTENTS

PART I: METALLURGY AND H_2S CORROSION OF SUPER MARTENSITIC STAINLESS STEELS

URN:NBN:no-2356

1.1 INTRODUCTION

The demands for more environmentally friendly and more cost effective flowline solutions have been the driving force behind the development of the super martensitic stainless steel (SMSS) pipes. Statoil has been a pioneer in this development, together with and in close co-operation with pipe producers and research institutes. The demand for an alternative to duplex stainless steel as flowline material in the Åsgard offshore field development initiated the project early in 1995.

One of the main challenges has been the peculiar behaviour of SMSS weldments during corrosion testing in the presence of hydrogen sulphide (H_2S) at ambient temperature. The oil companies involved in the recent field development projects such as Gullfaks Satellites, Åsgard[1,2] and Tune demonstrated, in fact, satisfactorily pitting resistances of the SMSS weldments at elevated temperatures of 90-140°C, whereas corrosion tests at ambient temperature in the presence of H_2S revealed a low resistance against pitting corrosion[2,3] of the inner pipe surface close to the weld metal (i.e. fusion boundary). Such results contradict the normal temperature dependency of corrosion resistant alloys (CRA's), and reopen the whole question whether the corrosion properties of SMSS alloys differ in a fundamentally manner from those of other classes of CRA's. Consequently, it is of vital importance for the end-users of such flowlines to clarify whether this merely is a lab effect or if it represents a potential operational problem that needs to be considered in the future.

1.2 PHYSICAL METALLURGY OF MARTENSITIC STAINLESS STEELS

The so-called 13%Cr steels belong to the group of "martensitic stainless steels". The martensitic stainless steels generally have the lowest corrosion resistance among the stainless steels due to the relative low alloying content. The SMSS have an intermediate corrosion resistance between conventional martensitic stainless steel and 22%Cr duplex stainless steel[4]. These steels are temperable and can be annealed, and are used where a combination of high strength and a moderate corrosion resistance are needed[5]. Martensitic stainless steels with approximately 13%Cr have been in use for applications in the oil- and gas industry for several decades. The grades used have a relative high carbon content, and are not usable for welding. The grade F6NM (13%Cr, 4%Ni) is since many years used for valves. These materials are, however, usable with mechanical connections, and the oil companies have good experience with

martensitic stainless steel of the 13Cr-4Ni type as production tubing (screwed connections) since the nineteen seventies[6]. Later, modified or so-called super martensitic stainless steels (SMSS) low in carbon with improved weldability and corrosion resistance have been developed. These grades are now in commercial use, also as pipelines[1,7,8,9,10].

Welding of martensitic stainless steels with high carbon content requires, however, post weld heat treatment (PWHT) for several hours in order to achieve acceptable hardness and toughness properties in the HAZ. They have therefore been regarded as non-weldable for pipeline applications. The use of welded components has been limited to smaller parts that can be placed in heating ovens, like flow loops at subsea templates. The weldable SMSS alloys with an ultra low carbon content have proved to be weldable with no or only limited use of PWHT and are therefore particularly useful as pipeline materials in the oil- and gas industry. By lowering the carbon content to below 0.015%, a relatively soft and tough martensitic matrix is obtained in the HAZ. Acceptable weld metal properties have been achieved by using duplex and super duplex welding consumables[1].

The weldable SMSS contain 11-12%Cr and <0.015%C. A so-called lean grade contains 0.5%Ni and no Mo, while the high alloyed grades have up to 6.5%Ni and 2.5%Mo. Mo is added in order to improve the corrosion resistance of the steel, while Ni is added to balance the effect of Mo on the extension of the γ phase field. Table 1.1 shows representative chemical compositions of SMSS pipes used as flowline material in the Gullfaks Satellite and Åsgard Subsea projects.

Table 1.1. Typical chemical compositions of SMSS flowlines used in the Gullfaks Satellite and Åsgard Subsea field developments.

Steel*	C	Cr	Mo	Ni	P	S	Si	Mn	V	Cu	Nb	N	Al	Ti
A	0.010	11.94	2.06	5.29	0.016	0.001	0.14	0.54	0.020	0.02	<0.003	0.00076	0.023	-
B	0.01	12.14	2.11	6.13	0.014	0.001	0.25	0.45	0.06	0.02	-	0.00065	0.027	0.080
C	0.007	12.02	2.46	6.39	0.015	0.001	0.13	0.45	0.05	0.03	-	0.00074	0.021	0.11

*) A: Kawasaki, B and C: Sumitomo

In order to understand the properties of stainless steels and the associated phenomena that take place in the heat affected zone (HAZ), knowledge of the phase diagrams that relate to the alloying elements used in these steels are required. Many welding phenomena can be explained and in many cases even predicted with the aid of phase diagrams. In chapter 1.2.1 the phase diagrams for iron in combination with the main alloying elements C, Cr, Ni and Mo are presented. Included is also a short description of the effect of Ti and of Nb. The conditions existing in welding, however, are highly non-isothermal where the

temperature fluctuations are locally of the order of 10^3 °C s^{-1}. Also in pipe manufacturing the heating and cooling rates are too fast to achieve equilibrium. Hence, these aspects are discussed in chapter 1.2.2.

1.2.1 Microstructural effects of alloying elements

Folkard's book[11] about the welding metallurgy of stainless steels has been the main source of information. Many figures are taken from Ref. [11], where the original references can be found.

1.2.1.1 Chromium and nickel

Figure 1.1 shows the Fe-Cr phase diagram. The element Cr constricts the γ-iron (i.e. austenite) with increasing alloying content until it disappears completely at approximately 12%. This means that above 12%Cr, no $\gamma \rightarrow \alpha$ (i.e. ferrite) phase transformation occurs. Cr strongly promotes the ferrite formation, so that only δ-iron (i.e. ferrite) crystallises from the melt over the full alloying range. At approximately 820°C precipitation of the brittle σ-phase in δ-iron starts. It consists of approximately 45%Cr and is an intermetallic compound consisting of Cr and Fe. It can be seen from Figure 1.1 that with 13%Cr, no $\gamma \rightarrow \alpha$ phase transformation occurs. However, in order to get the unique properties of a martensitic stainless steel, the $\gamma \rightarrow \alpha$ phase transformation must take place. The following text will describe why alloying elements promoting ferrite and austenite, respectively, are added in order to control the γ–iron phase field.

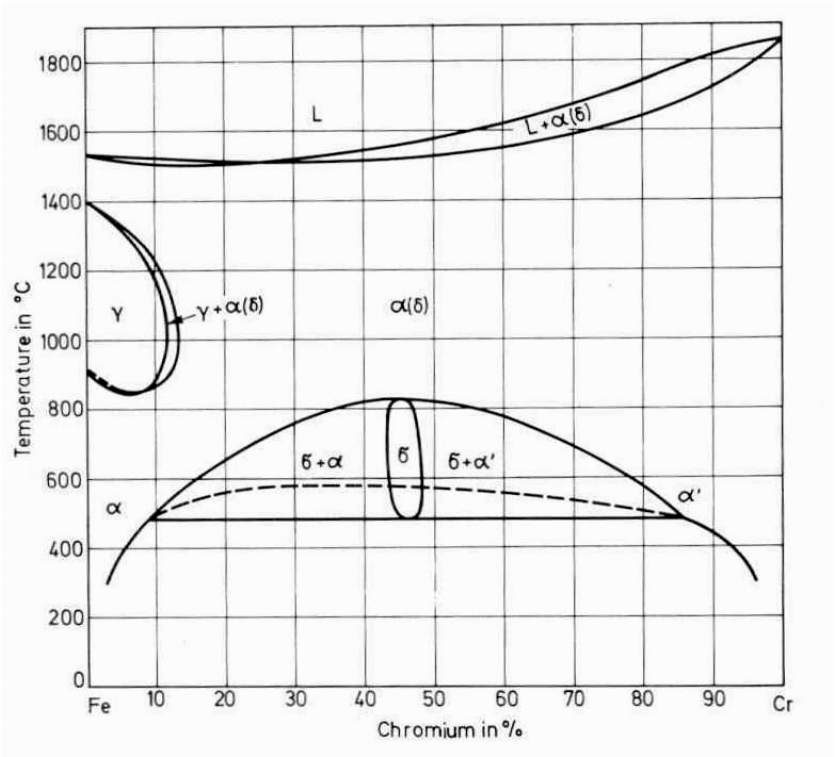

Figure 1.1. The Fe-Cr phase diagram[11].

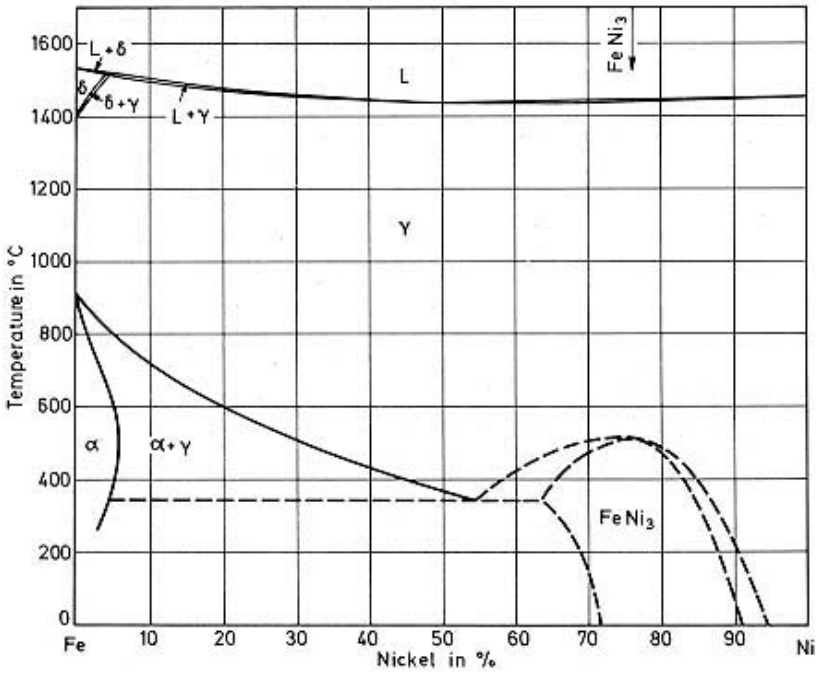

Figure 1.2. The Fe-Ni phase diagram[11].

Figure 1.2 shows the Fe-Ni phase diagram. Ni strongly promotes the austenite formation, and at approximately 5%Ni the melt does not solidify as δ but as γ-crystals. Ferrite formation from the melt is limited to the small δ-ferrite corner, with this ferrite being transformed back to austenite when cooling passes the temperature range of 1400-1450°C. Opposed to Cr, Ni does not constrict but will instead substantially expand the austenite phase field. With increasing Ni content, the $\gamma \rightarrow \alpha$ phase transformation is shifted to lower temperatures from about 900°C to 350°C.

Figure 1.3 shows various sections of the phase diagram at constant Cr:Ni ratios. Low carbon martensitic weld metal (and base metal) can be illustrated by means of Figure 1.3 (a). The melt precipitates primarily as δ-crystals. These crystals transform to γ-iron between 1400°C and 1100°C. The γ-crystals transform back into α-iron below 900°C.

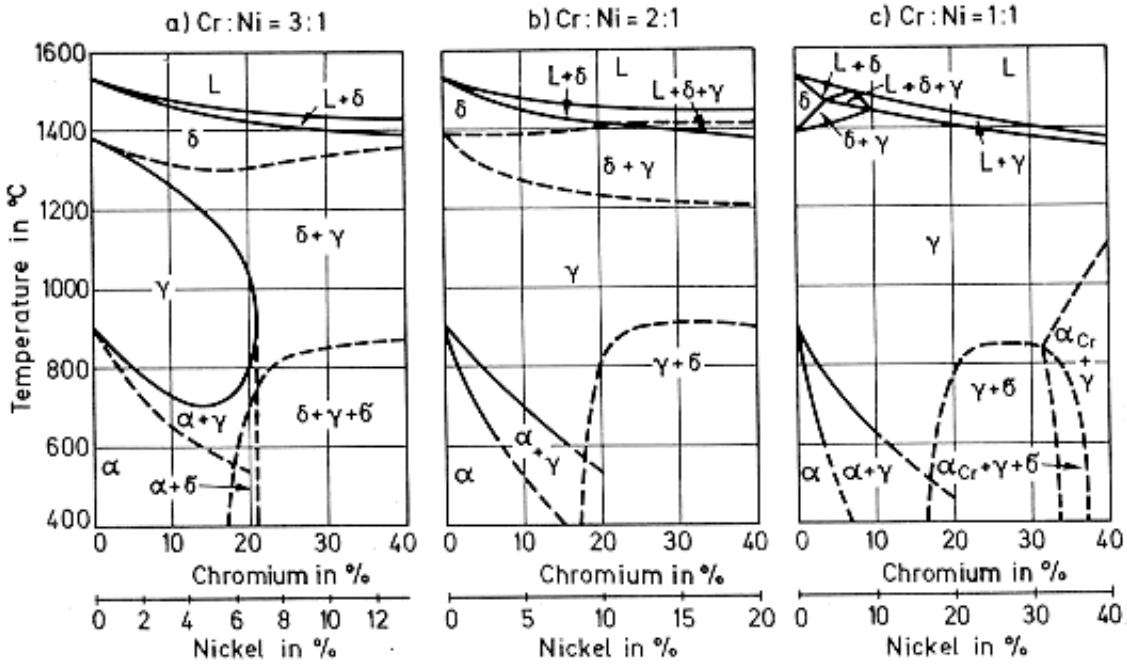

Figure 1.3. Sections of the ternary Fe-Cr-Ni phase diagrams for Cr:Ni ratios of 3:1, 2:1 and 1:1, respectively[11].

Figure 1.4 shows the influence of Ni on the extension of the γ phase field in the Fe-Cr system. The effect of Ni is important for the low carbon martensitic stainless steels, and Figure 1.5 shows very clearly how the γ-phase field is expanded by addition of Ni. The secondary γ–α-phase transformation is lowered from 900°C to 700°C. Due to the extension of the γ phase field the formation of undesirable δ–ferrite can be avoided.

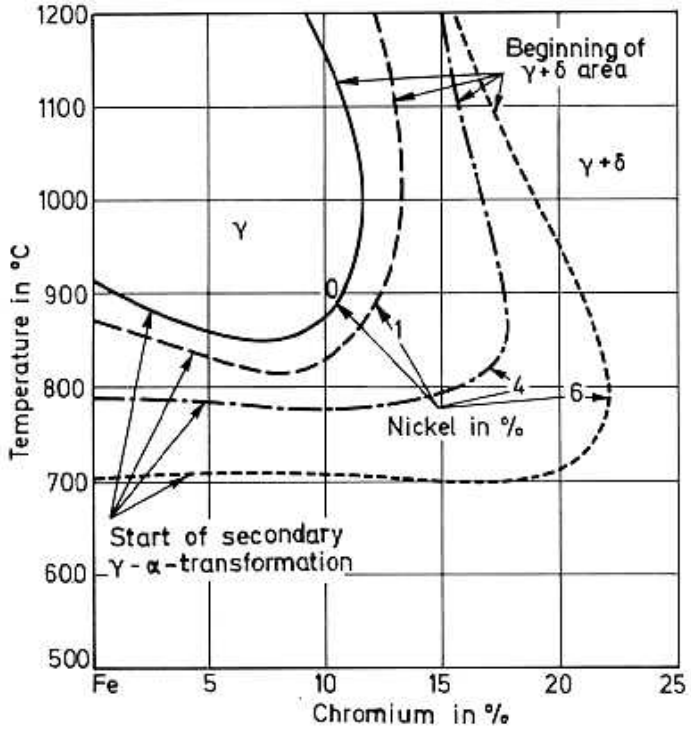

Figure 1.4. The influence of Ni on the extension of the γ phase field in the Fe-Cr system[11].

1.2.1.2 Carbon

The carbon content is usually kept lower than 0.015% in the new low carbon SMSS. This is done in order to make the steels weldable, i.e. to meet the current HAZ and weld metal hardness and toughness requirements. Cr is a strong carbide-forming element, with carbides such as $Cr_{23}C_6$, Cr_7C_3 and Cr_3C_2 being produced. The former two carbides may also form in stainless steels. In most cases, however, a mixed carbide $(Fe,Cr)_{23}C_6$ is formed. This is normally designated $M_{23}C_6$. Figure 1.5 shows a part of the ternary Fe-Cr-C phase diagram. It shows that the $M_{23}C_6$ carbide phase is stable above approximately 7%Cr. Figure 1.6 shows sections of the ternary Fe-Cr-C phase diagram at 13%Cr. It is apparent that the mixed carbide $M_{23}C_6$ (designated C_1 in Figure 1.6) already precipitates at temperatures below 700°C even at very low carbon contents (i.e. below 0.01wt%). Figure 1.6 also shows that C strongly promotes the austenite formation.

Ni does not form carbides. In the Ni-C system, the latter element always precipitates as graphite. In commercial stainless steel carbon is bound to Cr and secondly to Fe and practically never present as graphite.

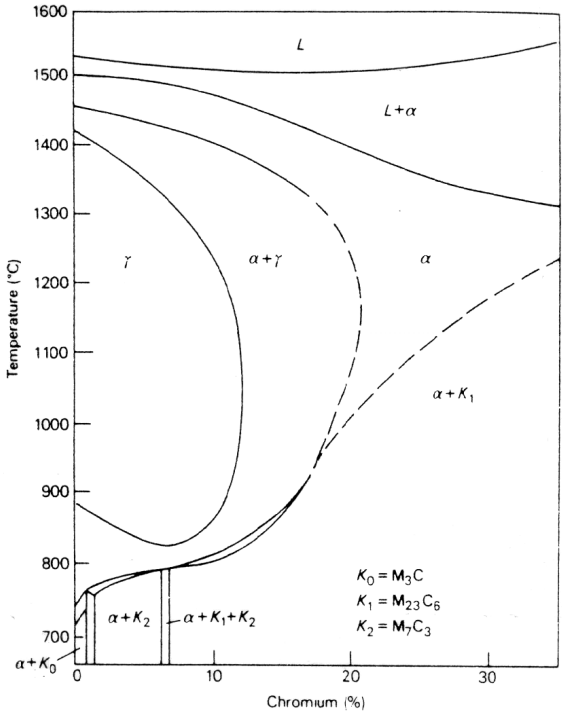

Figure 1.5. Effect of 0.05%C on the Fe-Cr phase diagram[12].

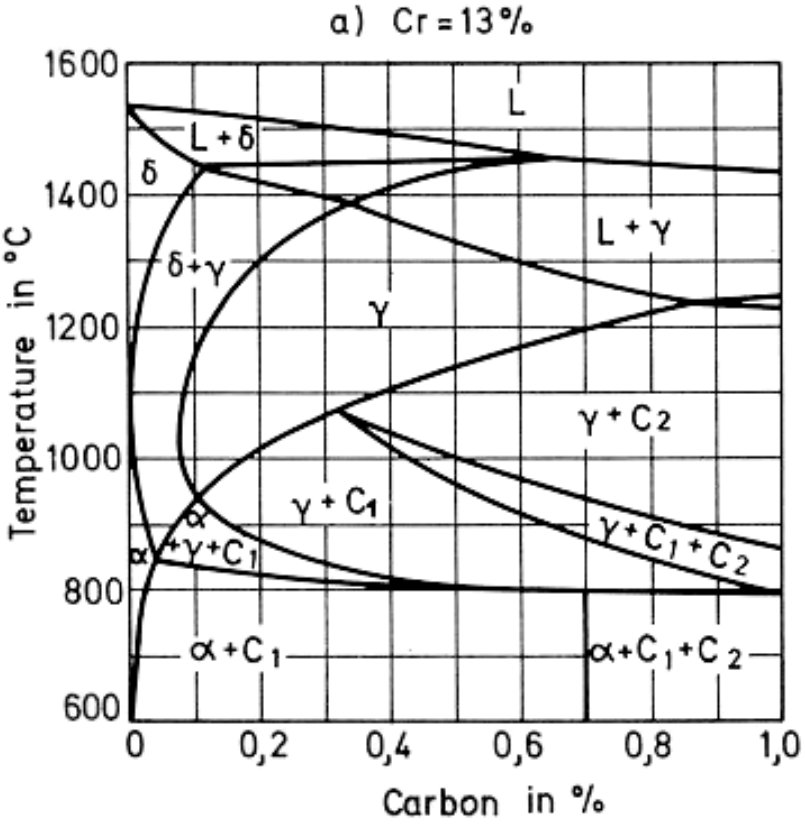

Figure 1.6. Sections of the ternary Fe-Cr-C phase diagram at 13%Cr[11].

1.2.1.3 Molybdenum

Mo is an important alloying element in stainless steels. It has the same effect as Cr and increases the corrosion resistance considerable. Mo alloyed austenitic stainless steels with 2.5-3% Mo are called "acid-proof", since they are corrosion resistant in some acids[13]. Mo strongly promotes the ferrite formation (i.e. the δ–phase) like Cr, and is therefore called a ferrite-forming element. It constricts the γ iron phase field as shown in Figure 1.7 where the combined effect of Cr, Mo and C is summarised. Together with Fe, Mo forms intermetallic phases. The most important one is Fe_2Mo with approximately 45%Mo. It already starts to precipitate at relatively low Mo contents of around 5%. In the martensitic stainless steels, however, the Mo contents are restricted to a maximum of approximately 3%, and these phases are therefore of no interest in the present context.

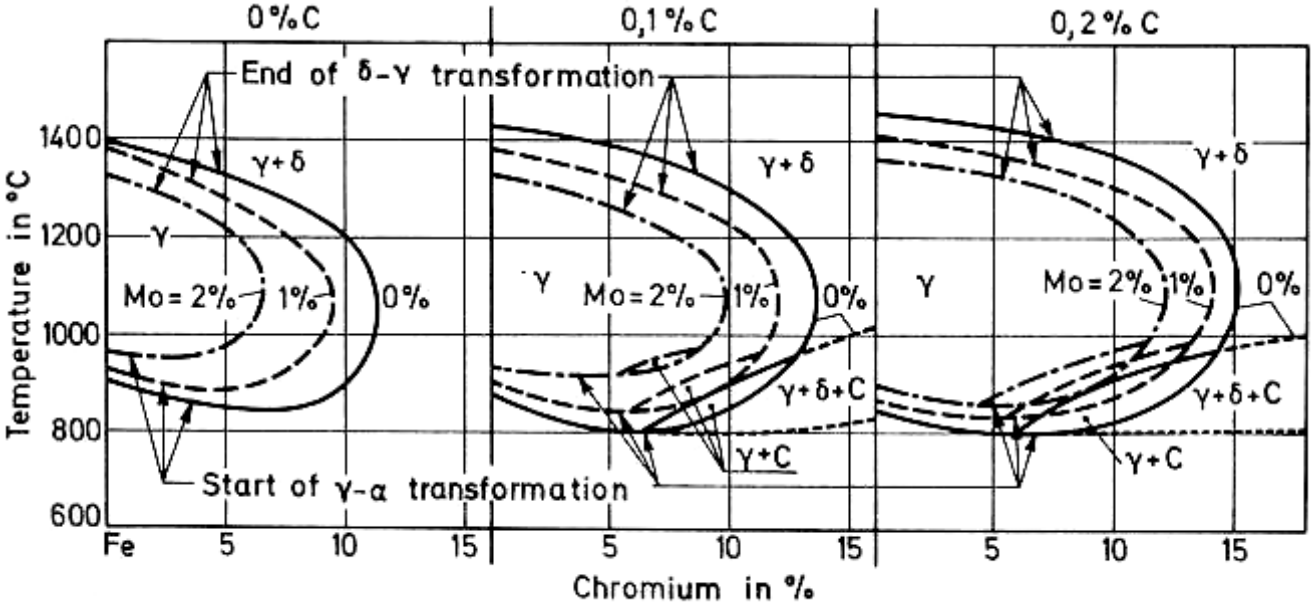

Figure 1.7. Influence of C and Mo on the extension of the γ phase field in the Fe-Cr system[11].

1.2.1.4 Other alloying elements

Manganese is an austenite former, and increasing additions therefore means that the $\gamma \rightarrow \alpha$ transformation is shifted towards lower temperatures. As a result, the austenite may become stable down to ambient temperatures. But contrary to Ni, Mn forms mixed carbides of the type $(Fe,Mn)_3C$. In stainless steels, however,

these carbides are of no great significance due to the fact that carbon is always associated with stronger carbide forming elements such as Cr or Nb.

Titanium is a ferrite former, and possesses a high affinity to carbon as well as to nitrogen. It is therefore used like Nb, to arrest free and form stable titanium carbide. With respect to SMSS, Ti is added in order to restrict grain growth in the fusion zone due to precipitation of small TiN particles.

Niobium is a ferrite former, and possesses a high affinity to C. This effect is used in steels and weld metals, to arrest C and form of niobium carbide (NbC), thereby improving the resistance to intergranular corrosion. This is the case for niobium stabilised stainless steels and weld metals.

1.2.2 Transformation kinetics

Phase diagrams, describing the thermodynamic equilibrium of different alloys, show the equilibrium properties of the actual steels. Thermodynamic equilibrium requires, however, infinite slow cooling rate. In practical, during steel manufacturing or in welding the maintenance of the thermodynamic equilibrium during cooling is neither possible nor desired. When e.g. a martensitic stainless steel cools from liquid to room temperature, the phase diagram predicts several structural changes, see Figure 1.3. At approximately 1450°C all liquid has solidified to δ-ferrite. At approximately 1230°C, δ-ferrite transforms to γ-iron. At approximately 700°C γ-iron transforms to α-ferrite, a phase which is stable down to room temperature. In reality, however, the γ-phase transforms to *martensite*. The reason for this is that structural changes require diffusion of atoms, which is a time- and temperature dependent process. If the alloy is sufficiently supercooled, the alloy may transform to metastable phases not predicted by the phase diagrams.

An important ingredient in the SMSS is retained austenite. The fine dispersed austenite that is formed during tempering contribute to the mechanical properties of the alloy, whereas other types of austenite phases may deteriorate its properties. The formation of various types of austenite is illustrated in Figure 1.10 for a 12%Cr-6%Ni-1.5%Mo steel[14]. It follows that some stable retained austenite, named Au_1, may be left over from the $\gamma \rightarrow$ martensite transformation. Secondly there is finely dispersed austenite, named Au_2, that may be formed during tempering at approximately 620°C. It is, according to Niederau[15], the cause of the high toughness of low carbon martensitic stainless steels. Finally, unstable austenite, named Au_3, is formed during tempering at temperatures above 620°C and is transformed into non-tempered, brittle martensite during

cooling. Figure 1.8 shows that the formation of the stable finely dispersed austenite increases the toughness, but reduces the yield strength.

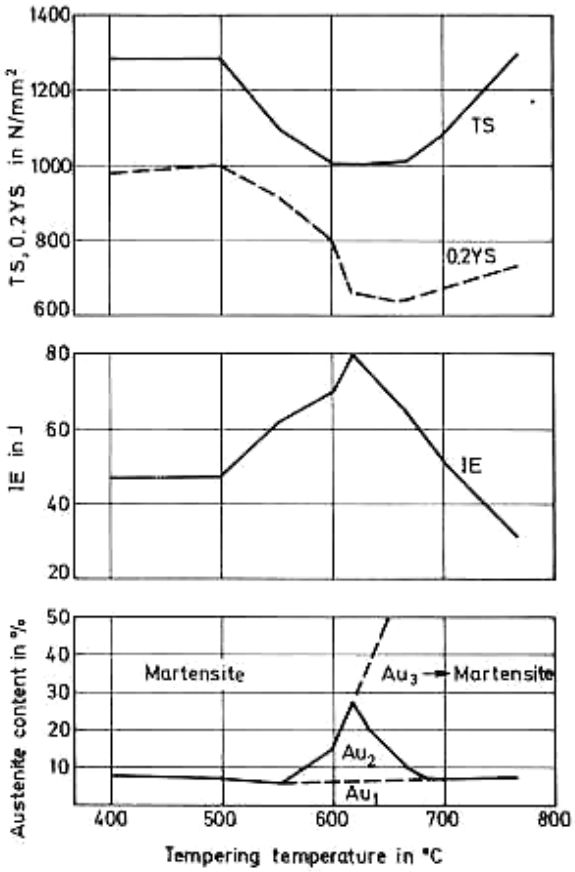

Figure 1.8. Influence of temperature on the yield strength (0.2 YS), tensile strength (TS), toughness and retained austenite content of steel grade 12Cr-6Ni-1.5Mo (Chemical composition in %: 0.039C, 0.35Si, 0.69Mn, 11.82Cr, 1.49Mo, 5.23Ni)[11,14].

The kinetics of diffusive ($\delta \rightarrow \gamma$ and $\gamma \rightarrow \alpha$) transformations and of displacive (γ-iron $\rightarrow$ martensite) transformations and the influence of the different alloying elements can best be illustrated by means of time-temperature-transformations (TTT) diagrams, or "C-curves". Figures 1.9 (a) and (b) show TTT curves for two standard martensitic stainless steels. These figures show the expected microstructures as a function of cooling rate. It illustrates why the structure is martensite and not bcc (α-iron). Even at slow cooling rates the γ-iron transforms to martensite. The thermodynamic equilibrium temperature for $\gamma \rightarrow \alpha$ transformation is in the range 750-800°C, while M_s is approximately 360-420°C. The new ultra low carbon SMSS have an even more "martensitic friendly" composition. The transformation "nose" (stable α-iron) for these steels is moved to longer time by several decades. According to Sumitomo and Kawasaki, it is not necessary to construct TTT diagrams for these steels, since

the structure becomes martensitic for all practical cooling rates, whereas M_s is approximately 200-220°C for SMSS, while M_f is more uncertain.

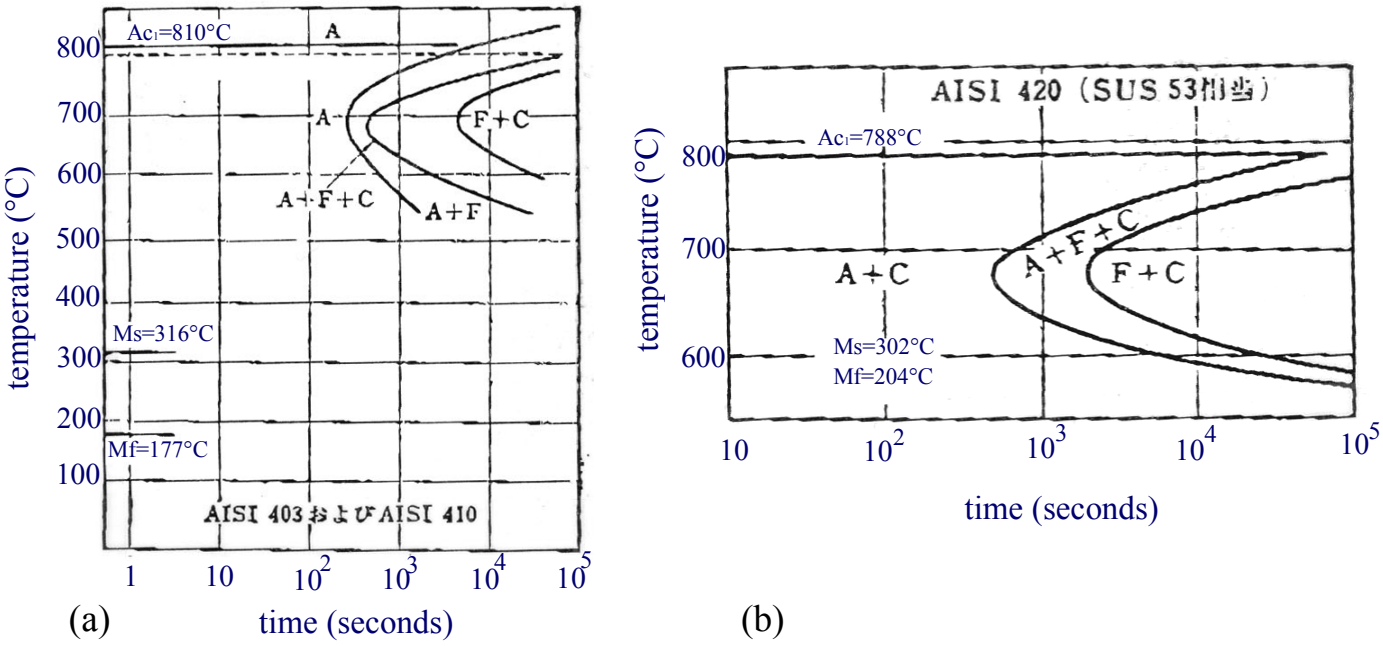

Figure 1.9. TTT curves for (a) AISI 410 and (b) AISI 420 martensitic stainless steels[16].

Alloying elements normally used in stainless steels reduce both M_s and M_f. Kulmburg *et* al.[17] have developed the following equation for the determination of the M_s temperature in °C which accounts for the influence of the alloying elements C, Mn, Cr and Ni:

$$M_s = 492 - 125 \cdot \%C - 65.5 \cdot \%Mn - 10 \cdot \%Cr - 29 \cdot \%Ni \text{ (in °C)} \qquad (1.1)$$

SINTEF measured M_s as a function of T_{max} for weld simulated base materials for some low carbon martensitic stainless steels[18]. The results from their investigation are presented in Figure 1.10. For the 12Cr-6.5Ni-2.5Mo steel (see Table 1.1), M_s varied between 200-300°C. This is somewhat higher than that calculated from the Kulmburg equation (i.e. Equation (1.1)), which predicts M_s of approximately 165°C.

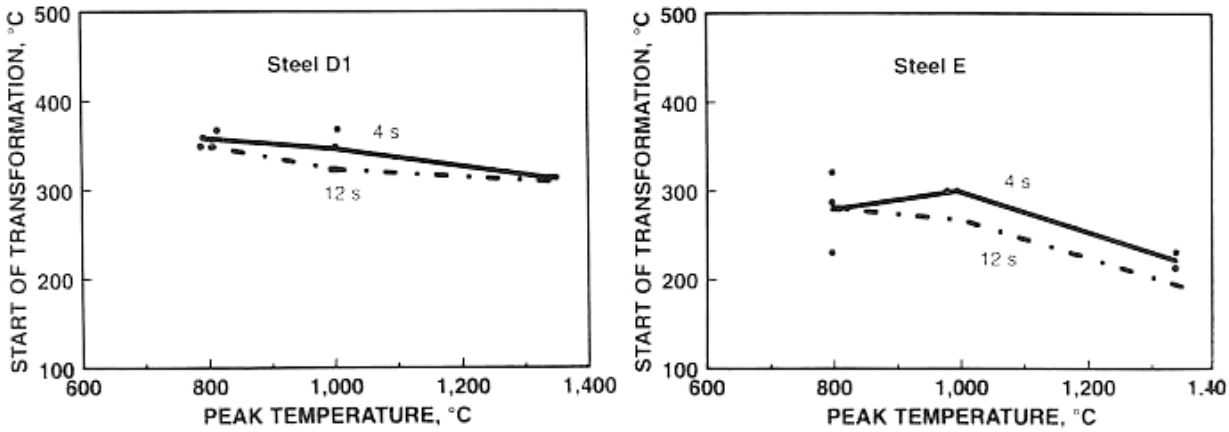

Figure 1.10. Effect of peak temperature on HAZ transformation temperatures (M_s)[18].

1.3 H_2S ASSISTED CORROSION OF MARTENSITIC STAINLESS STEELS

1.3.1 Introduction

The most detrimental corrosion mechanism associated with H_2S in SMSS flowlines is *Sulphide Stress Corrosion Cracking* (SSC). SSC requires hydrogen charging from the cathodic reaction at the steel surface and is basically a hydrogen embrittlement mechanism. However, in slightly sour service conditions with partial pressures of H_2S below 40mbar[2], nearly all incidents of SSC in SMSS weldments in laboratory testing are ascribed to preceding corrosion attacks, which indicate that SSC only occurs at conditions where the SMSS weldments are susceptible to pitting or general corrosion. The present study is therefore mainly concerned with the impact of H_2S on occurrence of corrosion in SMSS weldments.

Much of the focus in the various corrosion tests of low carbon martensitic stainless steels has been on "fit for purpose" testing, and less on gaining a more fundamental knowledge and understanding of the observed phenomenon. The end users are basically concerned whether the actual material can be used or not. The steel- and pipe producers are, on the other hand, focused on the requirements from the end user. There is hence limited literature data available that are concerned with a more fundamental approach on the impact of H_2S on corrosion in SMSS pipes and weldments. There is also a great scatter in the test results even for materials with identical alloy compostion[19]. Consequently, relevant literature data for other alloys are included in the present study.

1.3.2 Flowline corrosivity

A sound assessment of the flowline durability must account for variable operational conditions as well as the pre-history prior to exposure to the H_2S-containing well stream. Variations in the flowline corrosivity are associated with:

(a) Injection and transportation of acids, corrosion inhibitors, glycol etc.
(b) Variations in the operational conditions, such as flow, temperature, pressure, water cut, water composition, and H_2S and CO_2 contents.
(c) "Shut down" situations where the temperature drops towards the seabed temperature (i.e. 5°C) or to a temperature controlled by a flowline heating system (e.g. 25-30°C).

Unprocessed well stream is a mixture of hydrocarbons (i.e. oil, condensate, and gas phases), of carbon dioxide (CO_2), of H_2S, and of water. In the reservoir, the water phase is in equilibrium with the surrounding formation and contains hence considerable amounts of salts such as chloride, sodium, calcium etc. Consequently, the water phase stemming from the reservoir is denoted formation water (FW), while the water that condenses along the pipe as the temperature drops due to cooling from the surrounding seawater is denoted condensed water (CW).

The partial pressures of H_2S and CO_2 have similar impact on the *pH* in the water phase, but the contribution from H_2S can be neglected in most *pH* calculations due to the high CO_2 : H_2S ratios. The *pH* values in the flowline are calculated by means of thermodynamic based computer programs, and are found to be in the range of 3.5 to 4 in the CW phase. The FW phase contains, on the other hand, bicarbonate (HCO_3^-) of, let say, 100 - 1600mg/l and also various salts. Bicarbonate has a buffer effect, whereas the increased ionic strength reduces the *pH*. Generally, the *pH* values in the FW phase is found to be in the range of 4.5 to 6.5.

Above 200°C hydrocarbon phases containing naphtenic acid may be corrosive, whereas below 200°C corrosion requires water wetting of the pipe wall. Hence the corrosivity in SMSS flowlines is related to parameters such as temperature, chloride content (for stainless steels), dissolved CO_2 and H_2S, *pH*, flow rate, microbial activity and the pipe material. Local variations at the steel surface of species such as CO_2, H^+, HCO_3^-, metal ions and H_2S due to electrochemical reactions or flow may also influence the corrosion reactions. With respect to the pipe material, the susceptibility to corrosion depends on microstructure, chemical composition, which again depend on material processing, fabrication

and any surface modificications[20]. The effect of welding should also be considered. Microstructural variations or precipitations as well as modification of the root surface conditions may be critical on the corrosion resistance of stainless steels.

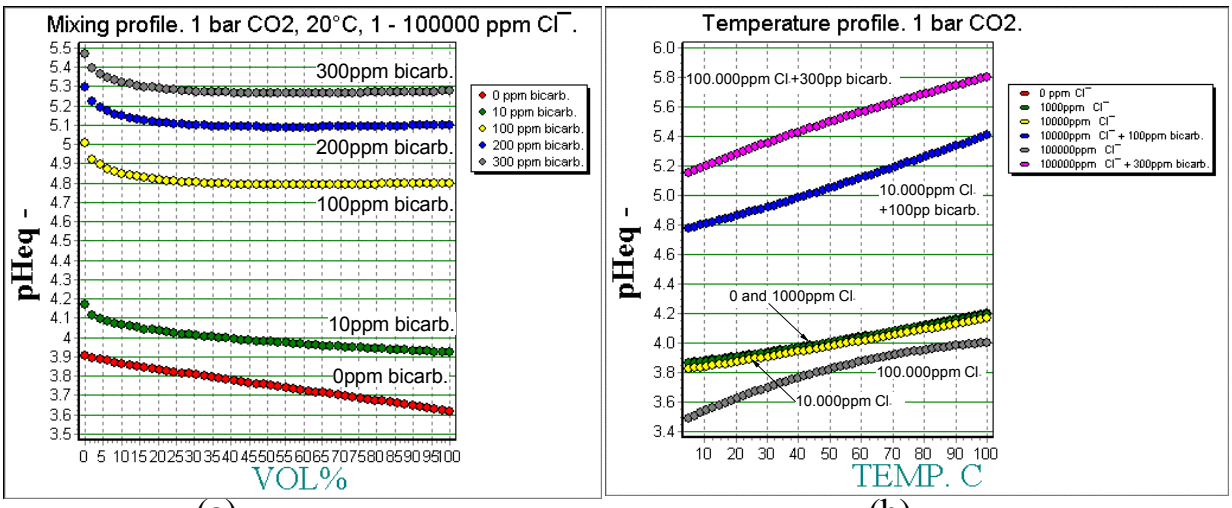

(a) (b)

Figure 1.11. (a) *pH vs.* ionic strength, where 100vol% is equivalent with ionic strength of 2.82*M* and 0vol% with 0*M*. (b) *pH vs. T* for various amounts of Cl^-. Notice that the 0ppm Cl^- is hidden behind the 1000ppm curve. Calculated by means of MultiScale[21].

To give an impression of how CO_2, ionic strength and bicarbonate influence the *pH* value, calculations are carried out by means of Multiscale[21]. Figure 1.11 (a) shows *pH vs.* ionic strength for various bicarbonate concentrations, where 100 and 0vol% are equivalent with ionic strengths of 2.82 and 0*M*, respectively. It follows that the *pH* is not very sensitive to variations in the ionic strength, while it is more sensitive to variations in the amount of bicarbonate. Figure 1.11 (b) shows *pH vs.* temperature for various chloride and bicarbonate concentrations. It follows that the *pH* increases in the order of 0.5 *pH*-units from 20 to 100°C.

1.3.3 The impact of H_2S on corrosion

H_2S is a very poisonous gas that often is a natural ingredient in the reservoir, whereas sulphate-reducing bacteria (SRB) may produce H_2S in oilfields with seawater injection. The well streams from the Statoil operated Gullfaks Satellite and Åsgard fields contain, e.g., in the range of 4 to 40ppm H_2S in their gaseous phases, whereas the Statfjord and Gullfaks fields experienced H_2S due to sea water injection and subsequent activities of SRB several years after production start-up.

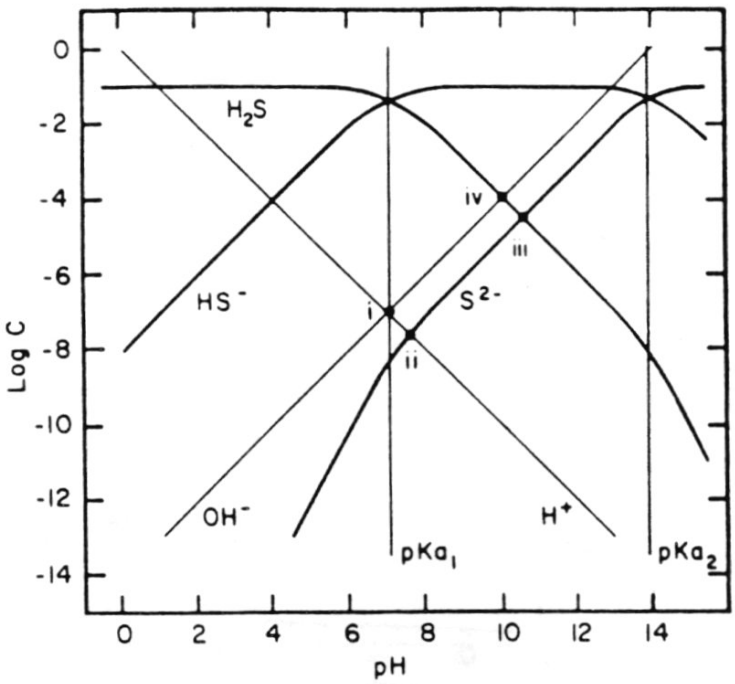

Figure 1.12. Log(*C*) *vs. pH* diagrams for H_2S dissolved in pure water. The figure shows the concentration distribution of species H_2S, HS^-, and S^{2-} *vs. pH* at ambient temperature and pressure[22].

H_2S is soluble in water and in equilibrium with S^{2-} and HS^-, depending on the *pH*. Figure 1.12 shows a log(*C*) *vs. pH* diagram of species H_2S, HS^-, and S^{2-} at ambient temperature and pressure. According to this figure, dissolved H_2S mainly remains non-dissociated in the actual *pH* range.

The impact of H_2S on corrosion of metals and alloys is ascribed to effects of atomic sulphur specifically adsorbed on the alloy surface (i.e. S_{ads}). This has several detrimental effects on the corrosion properties of stainless steels[23], which will be outlined in the following text.

1.3.3.1 Adsorption of sulphur on the steel surface

This chapter is concerned with *why* atomic sulphur stemming from H_2S tends to adsorb on metal surfaces. Thermodynamic calculations have shown that atomic sulphur specifically adsorbed on metal surfaces is thermodynamically stable, also under conditions where the sulphides are unstable. Marcus and co-workers have constructed *E vs. pH* diagrams for adsorbed species on single crystals of pure Ni[24], Fe[25] and Cr[26], and are plotted in Figures 1.13 (a), (b) and (c),

respectively. These diagrams are prepared for pure metals, but are useful as qualitative tools also for alloys. Their theoretical background can be found in Refs. [23,24,25,26], but some of the theory are presented in the following text[23, 24] to introduce this concept.

If pure Ni is used as an example, some of the reactions and the potential-*pH* relations for the equilibrium between water, the stable sulphur species, and the elements O and S adsorbed on Ni can be expressed as:

$$S_{ads}(Ni) + 5H_2O(l) \leftrightarrows SO_4^{2-} + O_{ads}(Ni) + 10H^+ + 8e^- \quad (1.14)$$

$$E = 0.50 + 0.007\log\left(HSO_4^-\right) + 0.007\log\left(\frac{\theta_0}{\theta_S}\right) - 0.074\,pH \quad (1.15)$$

$$H_2S(aq) + H_2O_{ads}(Ni) \leftrightarrows S_{ads}(Ni) + H_2O(l) + 2H^+ + 2e^- \quad (1.16)$$

$$E = -0.77 - 0.030\log(H_2S) + 0.030\log\left(\frac{\theta_S}{1-\theta_S-\theta_O}\right) - 0.059\,pH \quad (1.17)$$

$$HS^- + H_2O_{ads}(Ni) \leftrightarrows S_{ads}(Ni) + H_2O(l) + H^+ + e^- \quad (1.18)$$

$$E = -0.97 - 0.030\log(H_2S) + 0.030\log\left(\frac{\theta_S}{1-\theta_S-\theta_O}\right) - 0.030\,pH \quad (1.19)$$

Referring to Figure 1.13 (a), this diagram implies that S_{ads} atoms replace adsorbed H_2O molecules during anodic polarisation, where the replacement itself occurs within a narrow potential range of about 30mV. Further, the same figure suggests that adsorbed O atoms replace S_{ads} in the upper potential range. Such diagrams do not provide any kinetic information, but they substantiate possible occurrence of H_2S assisted corrosion at potentials and *pH* values experienced during corrosion tests in CW and FW.

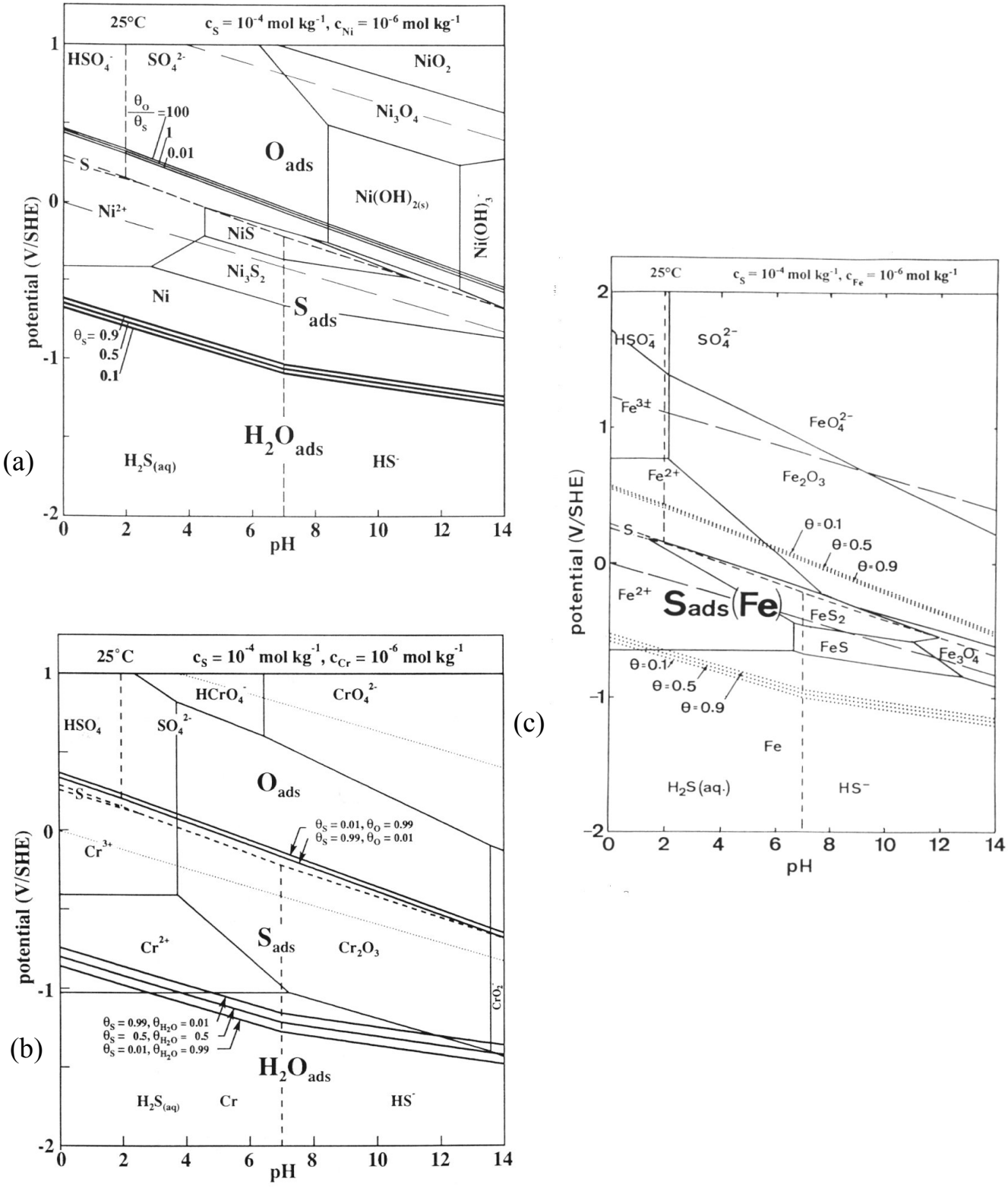

Figure 1.13. Potential-*pH* diagram for S_{ads} on (a) Ni[24], (b) on Fe[25], and (c) on Cr[26].

1.3.3.2 Impact of adsorbed sulphur on anodic dissolution

S_{ads} is reported to accelerate anodic dissolution[23] due to the catalytic nature of the accelerating effect of S_{ads}. This effect is demonstrated in Figure 1.14, where the polarisation diagrams for a Ni-Fe single-crystal alloy [Ni-25Fe (100)(at%)] with and without pre-adsorbed sulphur are shown[23]. These results show firstly that a monolayer of S_{ads} accelerates the anodic current density. Moreover, Figure 1.14 demonstrates that S_{ads} atoms are very stable, inasmuch as they remain attached to the metal during dissolution. In fact, this means that a small amount of S_{ads} can stimulate the dissolution of a significant amount of material. This accelerating effect has been attributed to a weakening of the metal-metal bonds induced by S_{ads}, which leads to a lowering of the activation energy barrier for the passage of a metal atom from the surface to the solution, referring to the illustration in Figure 1.15.

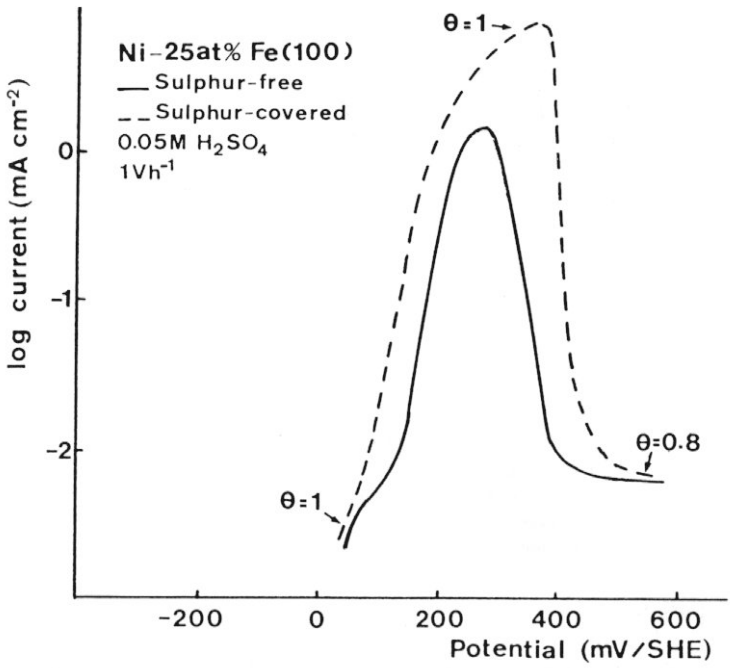

Figure 1.14. The influence of S_{ads} on the *i-E* diagram for Ni-25Fe (at%) single crystal [(100) face)] in 0.05M H_2SO_4. θ is the coverage of S_{ads} [27].

An acceleration factor *R* is defined as the ratio of the currents at the maximum of the active peaks with and without S_{ads}. Values in the range of 5 to 12 have been observed[23].

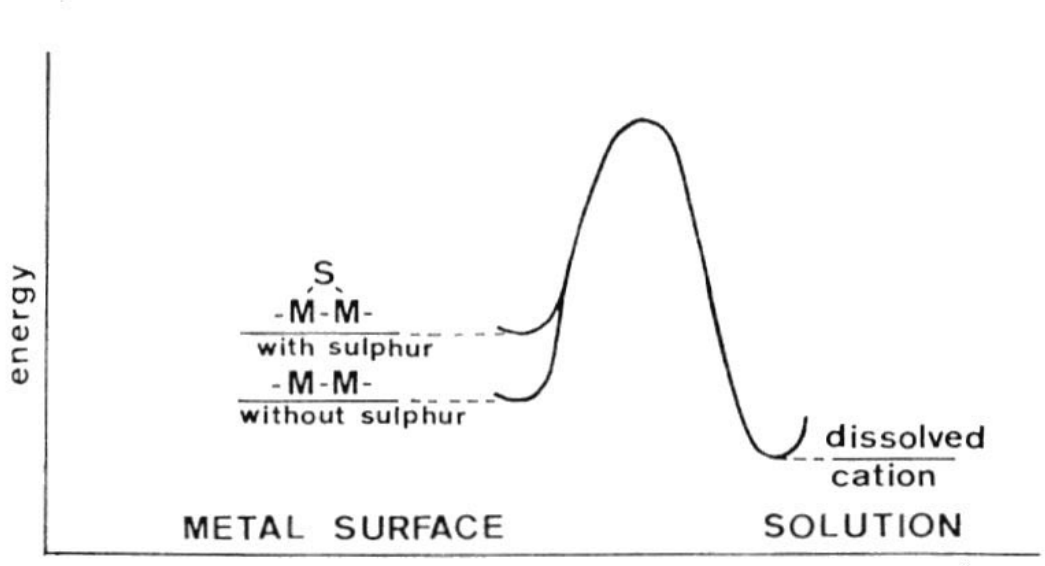

Figure 1.15. Weakening of the metal-metal bond by S_{ads} and acceleration of the dissolution of the metal[23].

1.3.3.3 Impact of adsorbed sulphur on passivation

Marcus claims that specifically adsorbed sulphur "poisons" the passivation at a sufficiently high coverage[23]. The adsorbed sulphur is thermodynamically very stable, and the sulphur-metal bond is strong and it may block the sites of the precursors in the formation of the oxide layer (i.e. hydroxyl ions[23]). The sulphur-contaminated surface also affects the properties of the growing film. Firstly, S_{ads} slows down the repassivation kinetics. Measurements of the passivation kinetics by means of potential steps of surfaces with and without S_{ads} have demonstrated that the time to complete passivation increases when the surface is covered by S_{ads} [23]. This effect is ascribed to a reduction in passivation sites, and to a hindering of the lateral growth of the passive film. Secondly, the sulphur-contaminated surface modifies the growing oxide. In a test with Ni, it was discovered that a more defective polycrystalline film was obtained in the presence of sulphur than without the presence of sulphur[28]. The current density in the passive state was, accordingly, about four times larger for the film formed with sulphur at the metal-oxide interface.

1.3.3.4 Effect of alloying elements on S-induced dissolution

S_{ads} is found to be highly stable on pure Ni. During active dissolution of a Ni alloy, the pre-adsorbed S_{ads} remained on the alloy surface[23], referring to Figure 1.14.

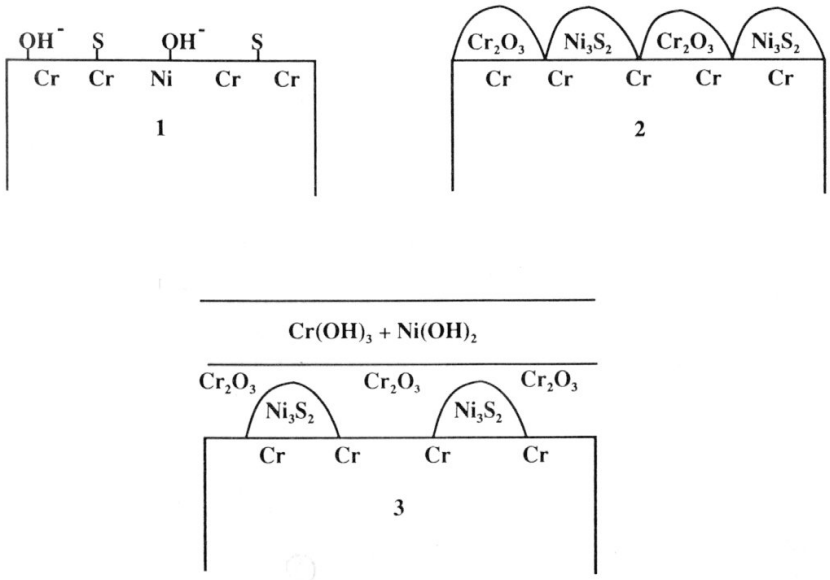

Figure 1.16. Mechanisms of the antagonistic effects of chromium and sulphur on the corrosion resistance of Ni-Cr-Fe alloys[23,30].

Mo is believed to bond to and remove S_{ads} atoms[23]. The number of Mo atoms needed to remove one adsorbed sulphur atom depends on the alloy composition. The results obtained from a survey of a Ni-6%Mo alloy indicated that two Mo atoms bond and removed one sulphur atom. In a survey of CRA's with compositions close to type 304 (Fe-17Cr-12.6Ni) and 316 (Fe-17Cr-14.5Ni-2.3Mo), Elbiache and Marcus[31] observed that only one Mo atom bond and remove one sulphur atom in the 316-type steel, while hardly no desorption was observed for the 304-type steel. This suggests that Cr lower the number of Mo atoms required to promote the dissolution of sulphur.

Cr allows the surface to be passivated under conditions in which the passivation would be precluded by sulphur if there were no Cr[23]. As opposed to Mo, desorption of sulphur is not the key factor with Cr. What Cr does is to react selectively with oxygen (i.e., with OH or H_2O) to give Cr oxide, whereas Ni reacts with sulphur. Cr acts as an oxide former while Ni acts as a sulphide former. This competitive mechanism is represented schematically in Figure 1.16.

1.3.3.5 Composition and structure of the surface film

During anodic dissolution are some elements enriched on the surface due to formation of oxides and sulphides. Ni and Mo are sulphide formers, while Cr basically is an oxide former.

Amaya *et* al. [32] carried out SIMS analysis of the element distribution on the surface film of a martensitic stainless steel with 0.7Mo under various test conditions. Referring to Figure 1.17, SIMS analysis were carried out on: (a) an "as polished" surface, (b) same as (a) after exposure in a 14000ppm Cl^-, 27bar CO_2, 150°C electrolyte for 48 hours, and (c) same as (a) after exposure in a 5%NaCl, 30bar CO_2, 0.1bar H_2S, 25°C electrolyte for 336 hours. The surface film on the "as-polished" specimen consists mainly of Cr oxide in a less than 1nm thin layer. After the test at 150°C in sweet conditions, the surface film is more than 30nm thick and is enriched in Cr, which substantiate a Cr-oxide. Ni and Mo are, on the other hand, slightly depleted compared to the bulk steel composition. Enrichment in Cr is found also in the surface film on the specimen exposed to the H_2S containing solution at 25°C, but it is located to the inner layer, indicating that a Cr-oxide film is formed beneath the sulphide layer. The S-distribution corresponds, on the other hand, to the Mo, Ni and Fe enrichment in the outer layer, indicating the presence of sulphides in the outer layer. This is consistent with the model of a corrosion film on alloyed martensitic stainless steels in Figure 1.18 proposed by Sumitomo[16]. It follows that the inner layer consists of a Cr_2O_3 film, whereas the outer layer consists of different sulphides. This seems consistent with the schematic model in Figure 1.16.

Amaya[32] also tested a martensitic stainless steel without any Mo in 5%NaCl, 30 bar CO_2, 0.1bar H_2S, 25°C, 336 hours. This time, no Cr oxide was observed in the surface film. The same observation was done by Fierro *et* al.[33]. XPS investigations confirmed the lack of Cr oxide in the surface film formed on conventional martensitic stainless steel in a H_2S-Cl^- environment (ambient pressure; 10%H_2S and 90%N_2) with *pH* 2.7 at 80°C. The film was enriched by Fe and S and a very low Cr content. A combination of H_2S and CO_2 gave a better protective film than H_2S alone. Rogne[34] tested a martensitic stainless steel in a CO_2-Cl^- environment at with *pH* 2.7, 3.7 and 4.7 at 80°C. Augèr Spectroscopy measurements showed a Cr and O enrichment in the surface film, indicating the formation of a protective Cr oxide in the absence of H_2S.

These results confirm the beneficial effect of Mo-additions on the corrosion properties of martensitic stainless steels in H_2S containing solutions. They also imply a competitive formation of Cr-oxide and sulphides on the steel surface, which may be important for the final corrosion resistance.

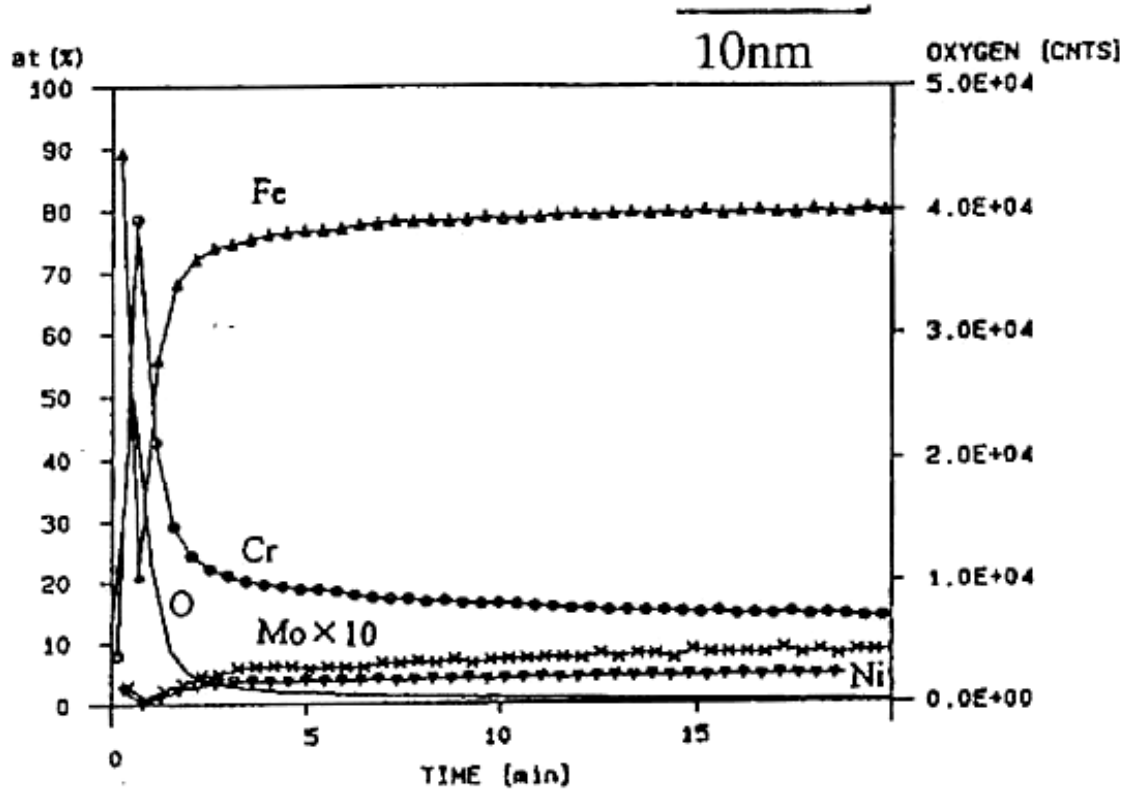

(a)

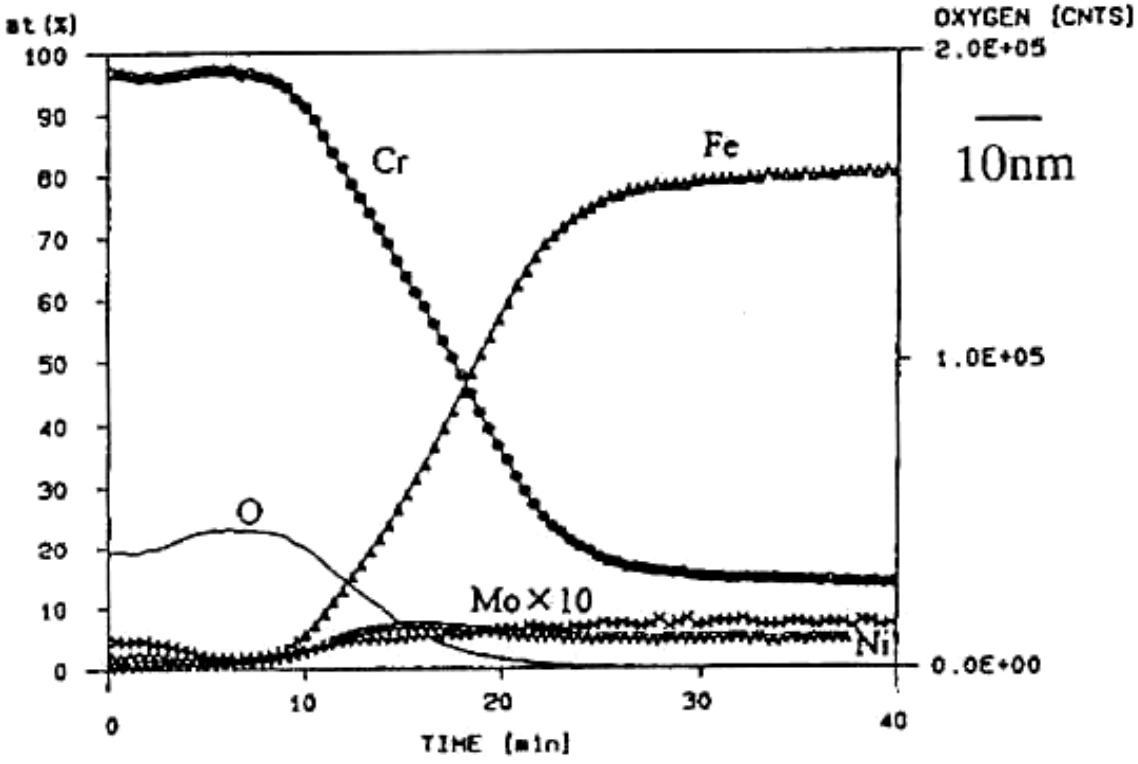

(b)

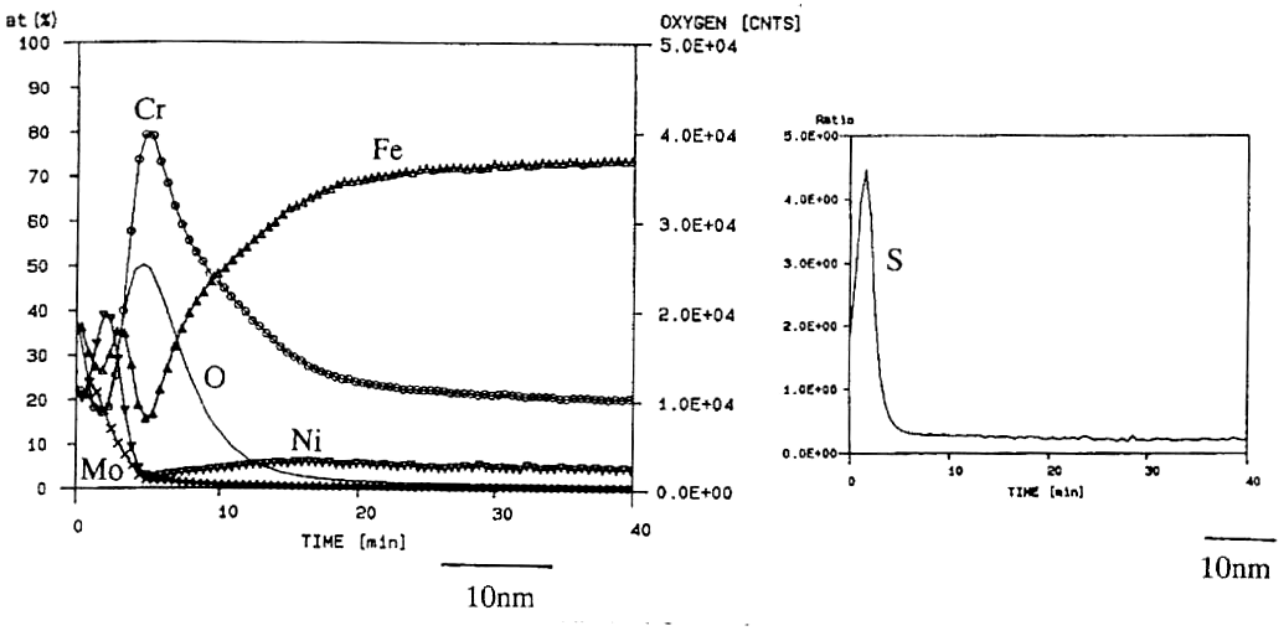

(c)

Figure 1.17. Element distribution on the surface film of a martensitic stainless steel with 0.7%Mo in (a) "as polished" condition (previous page), (b) after immersion in a 14000ppm Cl^-, 2.7Mpa CO_2, 150°C electrolyte for 48 hours, and (c) after immersion in a 5%NaCl, 30 bar CO_2, 0.1bar H_2S, 25°C for 336 hours[32].

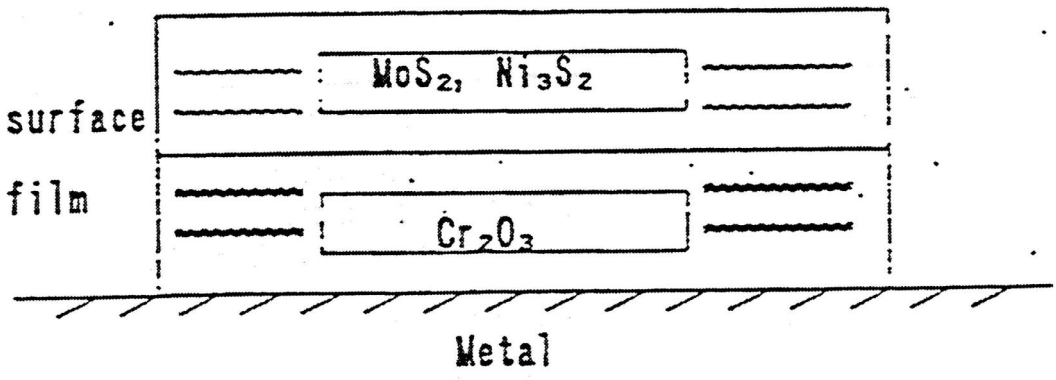

Figure 1.18. A model of corrosion resistant film on a SMSS[16].

1.3.4 Corrosion mechanisms in H_2S solutions

1.3.4.1 Active corrosion

Generally, CRA's are susceptible to general corrosion only in strong acids and alkalies[35] and are therefore assumed passive in CW and FW conditions in the *pH* range of 3.5 to 5.5. However, SMSS weldments were found to be vulnerable to active corrosion in SSC tests[2,36] at $pH \leqslant 3.5$ in a 49m*M* NaAc solution containing 0.8mM H_2S (i.e. 8mbar). Drugli[36] applied ideas proposed by Pourbaix[37] and constructed a tentative *E vs. pH* diagram that demonstrated how SMSS alloys in buffered H_2S solutions may exhibit a potential dependent activation. This chart is shown in Figure 1.19, and illustrates that the active samples repassivated at certain potentials during anodic polarisation, whereas it was impossible to activate samples at *pH* 4.5.

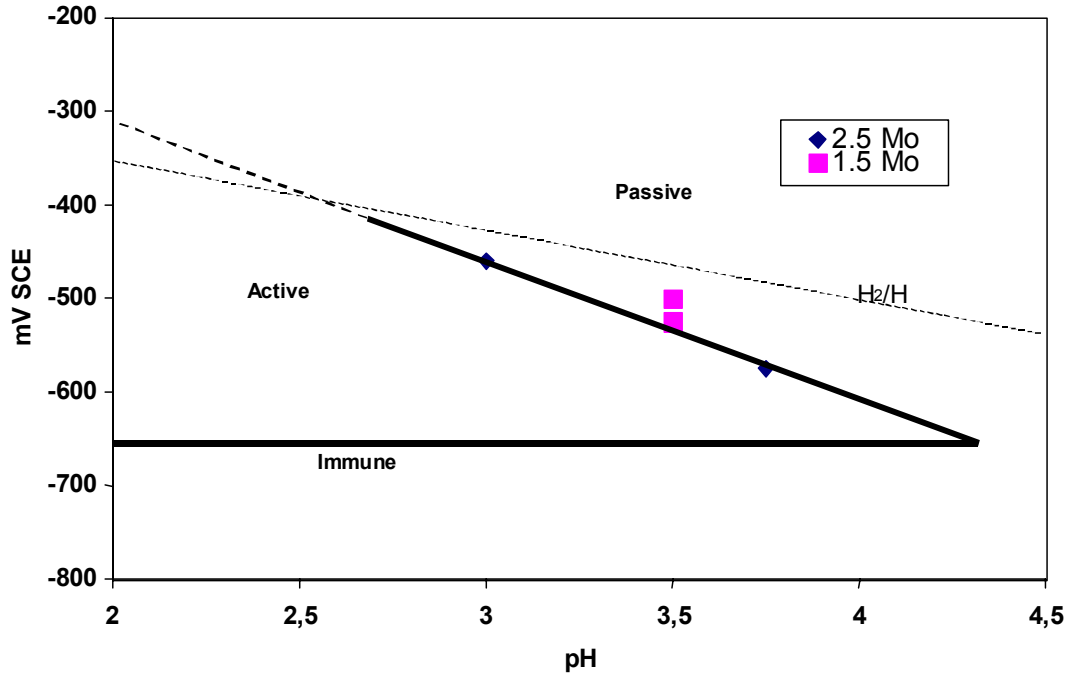

Figure 1.19. A tentative potential-*pH* (Pourbaix) diagram for SMSS in H_2S[36].

Østhus[38] demonstrated that it is impossible to activate SMSS under the prevailing test conditions unless H_2S is present, even at *pH* values of 1.5 to 2.5 in the 49m*M* NaAc solution. However, as the nitrogen gas applied for deaeration was replaced by a gaseous mixture of 20mbar H_2S and CO_2 (balance), then the SMSS specimen activated. To summarize, active corrosion in SMSS seems to be favoured by a low *pH* and a strong buffer in combination with H_2S. Partly passivated surfaces such as root weld surfaces or pipe surfaces containing mill scale are particularly vulnerable to activation.

Neither buffer nor acetate is present in the CW phase in a real flowline. It is still important to gain more knowledge about active corrosion and the buffer effect on SMSS. The commonly applied guideline for SSC testing of stainless steels, EFC 17[39], specifies a buffer of 49m*M* NaAc (4.0g/l) in the standard test solution. Such a study will also improve our general knowledge of corrosion mechanisms such as pitting and SSC in slightly sour conditions.

1.3.4.2 Pitting corrosion

Pitting corrosion is localised corrosive attacks that develop as a result of the coexistence of active and passive regions on the metal surface. The mechanism is thoroughly reviewed by several authors[35,40,41]. For a detailed mechanistic discussion the following stages are usually distinguished: (1) Processes leading to breakdown of passivity, (2) Early stages of pit growth, (3) Late stages of pit growth, and (4) Repassivation phenomena.

Pitting depends on the alloy (i.e. microstructure, inclusions, chemistry and surface condition) as well as on the electrolyte and other environmental factors. The passivity breakdown caused by chloride ions is a very important factor that depends on the temperature. Sulphur compounds (SO_4^{2-}, $S_2O_3^{2-}$, H_2S) are also important. It has been shown that sulphur alone can enhance the dissolution, block or retard the growth of the passive film, and cause passivity breakdown and pitting by enrichment at the metal-film interface[23]. All these effects can evidently also take place in the presence of chloride. According to Marcus, a major difference between the action of chloride and sulphur is that sulphur does not seem to interact directly with the oxide surface as strongly as chloride[23]. Marcus summarises a likely mechanism for the combined action of chlorides and sulphur, where the local breakdown of the film is by Cl^-, which then permits all the effects of S_{ads} shown on metal and alloy surfaces to take place. A major consequence is the stabilisation of otherwise unstable (or metastable) pits, which is consistent with the lower pitting potential and/or shorter incubation time observed experimentally. This was, e.g., experienced by Mat[42] in a test of 316L in 0.6M NaCl at *pH* 3.4 at 25°C. The addition of 0.03*M* H_2S caused E_p to be more negative by nearly 500mV than in the solution without H_2S. Other important environmental variables are[1], oxidizing agents (O_2, H^+ etc.), inhibitor ions, the presence of certain microbiological consortia, velocity and biocides (ozone and chlorine).

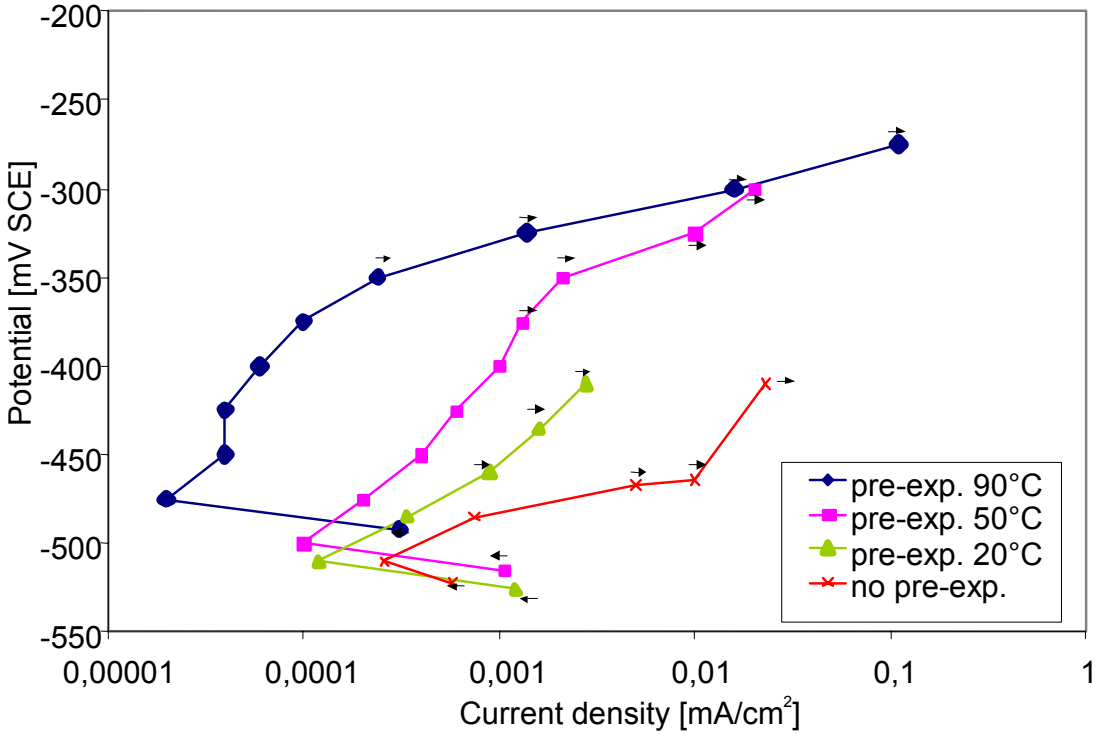

Figure 1.20. Pitting measurements carried out by SINTEF[43]. 20°C, 30000 ppm Cl^-, 100 mbar H_2S, scan rate 12.5mV/12 hour. Pre-exposure for 48 hours in a CO_2 environment at room temperature prior to the pitting measurements.

SMSS weldments are found to be more prone to pitting at low temperatures than at elevated temperatures of 90-140°C[2], which appears contrary to the general behaviour of stainless steels. There are also other test results[43], which indicate that the susceptibility to pitting corrosion in SMSS weldments is reduced during pre-exposures at elevated temperatures. Bjordal *et* al.[43] showed that pre-exposure of a SMSS weldment in a CO_2-saturated environment for 48 hours at ambient, 50 and 90°C, respectively, enhanced the passivity and increased the pitting potential of the specimens during a subsequent test at ambient temperature in 100mbar H_2S, referring to Figure 1.20.

1.4 IMPACT OF WELDING AND SCOPE OF PRESENT WORK

To summarise the present status, efforts should be done to clarify why pitting corrosion occurs at ambient rather than at elevated temperatures in the inner pipe surface close to the fusion boundary in SMSS weldments in the presence of H_2S. The area of interest in this study has therefore been limited to the pipe region near the fusion boundary apart from the weld metal. Some important parameters and definitions are illustrated in Figure 1.21. The heat released during arc

welding imposes temperature fluctuations and hence microstructural changes in the nearby pipe material. This region is commonly known as the heat affected zone (HAZ), and the stippled lines in Figure 1.21 confine its outer limits. The most well-known corrosion problem confined to the HAZ microstructure in stainless steels are associated with sensitisation phenomena, particularly in ferritic and austenitic stainless steels[1,11]. Moreover, the temperature fluctuations induced by welding causes high temperature oxidation reactions in the inner pipe surface close to the fusion boundary[29]. Although inert shielding gas is used, the oxygen infiltration is sufficient to promote the formation of high temperature oxides. The type and thickness of the oxide layer as well as possible Cr-depletion of the outermost steel[29] will, in turn, depend on the imposed temperature-time pattern as well as the oxygen potential in the shielding gas. The original passive film on the root surface close to the fusion boundary is destroyed during welding, and a new, Cr-depleted surface is formed that probably is covered by a metal oxide. The high temperature oxidation process most likely deteriorates the instant corrosion resistance of the root surface. It remains, however, to determine whether this only is a transitory, increased susceptibility to corrosion, or if high temperature oxidation processes creates any persistent corrosion problems in SMSS flowlines.

Parameters such as heat input, pipe thickness and bevel geometry determine the temperature transients throughout the HAZ and hence the microstructural and surface changes and modifications. The peak temperature distribution in HAZ during welding can be illustrated as in Figure 1.22 (a). The points close to the weld fusion boundary experience temperatures reaching the melting point, while the maximum temperature decrease with increasing distance from the fusion boundary. Figure 1.22 (b) shows a phase diagram showing how different points in HAZ has reached the different phase regions during welding (Figure 1.22 (b) from Figure 1.3). Variations in the HAZ may hence be predicted by means of such diagrams. A similar approach could be used to determine the potential for oxidation of alloying elements at the pipe surface.

It follows that the present study seeks to examine the impact of the welding process on the occurrence of pitting corrosion in the presence H_2S in terms of microstructural variations and in changes in the surface condition in the HAZ. Particular attention should be given to the role of H_2S and its ability to stabilize and accelerate anodic dissolution. The influence of S_{ads} on passivation can be a critical factor. Moreover, possible beneficial effects of surface modifications of the root surface on the pitting properties should be explored. Further, the dissolution and repassivation kinetics of the SMSS alloys should be determined and compared with other stainless steel to determine whether there are any fundamental differences between the various CRA's.

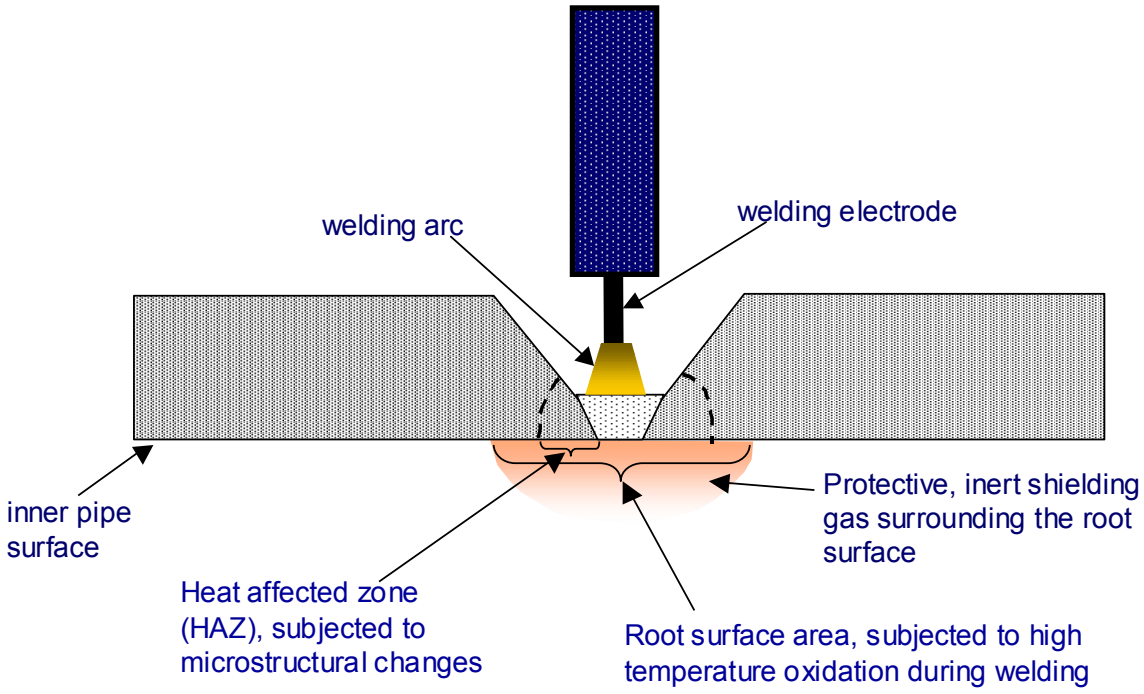

Figure 1.21. Illustration of the impact of welding on the pipe close to the weld metal.

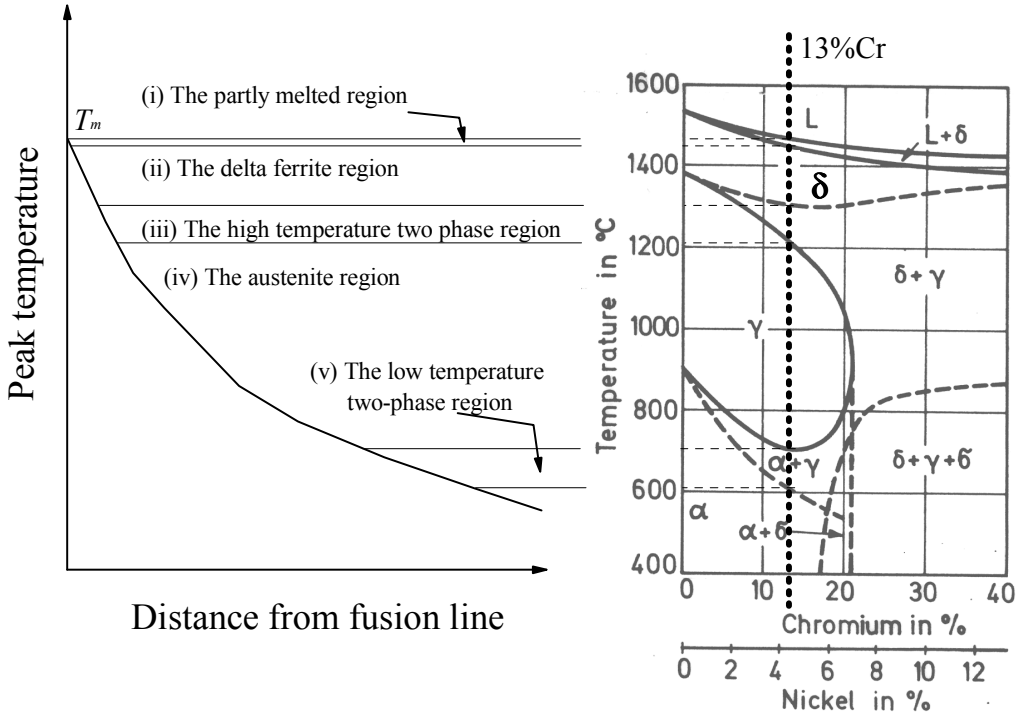

(a) (b)

Figure 1.22. Schematic diagram illustrating the structural changes that occur in the HAZ during welding of a martensitic stainless steel; (a) Peak temperature vs. position in HAZ, and (b) a phase diagram for Fe-Ni-Cr alloys[11].

1.5 REFERENCE

1. J. Enerhaug, S. L. Eliassen, P. E. Kvaale: *Corrosion/97*, paper no. 60, (Houston, TX: NACE International, 1997).
2. J. Enerhaug, P. E. Kvaale, M. Bjordal, J. M. Drugli, T. Rogne: *Corrosion/99*, paper no. 587, (Houston, TX: NACE International, 1999).
3. S. Olsen, P. E. Kvaale, J. Enerhaug: *SUPERMARTENSITIC STAINLESS STEELS '99*, Brussels, Belgium, 1999, Belgian Welding Institute, Belgium, pp. 84-87.
4. T. Okazawa, T. Kobayashi, M. Ueda, T. Kushida: *Development of Super 13Cr Stainless Steel for CO_2 Environment Containing a Small Amount of H_2S*. Sumitomo Metal Industries Ltd.
5. E. Bardal: *Korrosjon og korrosjonsvern*. Tapir Forlag, 1985.
6. M. Bonis, J.-L. Crolet: *Corrosion/94*, paper no. 7, (Houston, TX: NACE International, 1994).
7. K. Tamaki: *Corrosion/89*, paper no. 469, (Houston, TX: NACE International, 1989).
8. A. Miyasaka. H. Ogawa: *Corrosion/90*, paper no. 67, (Houston, TX: NACE International, 1990).
9. S. Hashizume, T. Takaoka, Y. Minami, Y. Ishizawa, T. Yamada: *Corrosion/91*, paper no. 28, (Houston, TX: NACE International, 1991).
10. M. Ueda, T. Kushida, T. Mori: *Corrosion/95*, paper no. 80, (Houston, TX: NACE International, 1995).
11. E. Folkard: *Welding Metallurgy of Stainless Steels*. Springer-Verlag, 1988.
12. R. Honeycomb, H. K. D. H. Bhadeshia: *Steels – microstructure and properties*. Eward Arnold, 1995.
13. J. M. Drugli, E. Bardal: *Rustfrie stål i prosess- og sjøvannssystem. Kompendium for endagsseminar.* SINTEF report STF16 A89045. Trondheim, 1989.
14. A. Kulmburg, F. Kortenheuer, M. Koren, O. Gründler, K. Hutterer, *Berg- u. hüttenm*., 1981, vol. 126, pp. 104-108.
15. H.J. Niederhau, *Stahl u. Eisen*, 1978, vol. 98, pp. 385-392.
16. Communication with dr. Ueda, Sumitomo, 1998.
17. A. Kulmburg, W. Sölkner, F. Kortenheuer, H. E. Schmied, *Berg- u. hüttenm.*, 1979, vol. 124, pp. 400-406.
18. O. M. Akselsen, M. Bjordal, T. Rogne, G. Rørvik: *A study of the properties of 13% Cr martensitic stainless steels*. SINTEF report STF24 F95605. Trondheim, 1995.
19. J. M. Drugli, T. Rogne: *A literature Study of SCC- and Corrosion testing of alloyed 13 Chromium Steels*. SINTEF report STF24 F02226. Trondheim, 2002.

20. U. Steinsmo, T. Rogne, J. M. Drugli: *Corrosion/94*, paper no. 492, (Houston, TX: NACE International, 1994).
21. MultiScale® is a computer programme developed at NTNU, Trondheim, by Baard Kaasa and Terje Østvold for Statoil, Norsk Hydro and Saga Petroleum.
22. F. M. M. Morel: *Principles of Aquatic Chemistry*. John Wiley&Sons, 1983.
23. P. Marcus: *Sulfur-Assisted Corrosion Mechanisms and the Role of Alloyed Elements*. ("Corrosion Mechanisms in Theory and Practice", P. Marcus and J. Oudar eds.). Marcus Dekker, 1995, pp. 239-263.
24. P. Marcus, E. Protopopoff, *J. Electrochem. Soc.*, 1993, vol. 140, pp. 1571-1575.
25. P. Marcus, E. Protopopoff, *J. Electrochem. Soc.,* 1990, vol. 137, pp. 2709-2712.
26. P. Marcus and E. Protopopoff, *J. Electrochem. Soc.*, 1997, vol. 144, pp. 1586-1590.
27. P. Marcus, A. Teissier, J. Oudar, *Corros. Sci.*, 1984, vol. 24, pp. 259-268.
28. J. Oudar, P. Marcus, *Appl. Surf. Sci.*, 1979, vol. 3, pp. 48-67.
29. J. Vagn Hansen, E. Maahn, P. Aastrup, P. F. Larsen, *Beskyttelsesgasdækning og korrosionsbestandighed efter svejsning af rustfrie stålrør*. Report 87.66, Korrosjonssentralen ATV, Denmark, 1987.
30. P. Marcus, J.M. Grimal, *Corros. Sci.*, 1990, vol. 31, pp. 377-382.
31. Elbiache, P. Marcus, *Corros. Sci.*, 1992, vol. 33, pp. 261-269.
32. H. Amaya, K. Kondo, H. Hirata, M. Ueda, T. Mori: *Corrosion/98*, paper no. 113, (Houston, TX: NACE International, 1998).
33. G. Fierro, G. M. Ingo, F. Mancia, *Corrosion/88*, paper no. 215, (Houston, TX: NACE International, 1988).
34. T. Rogne: *Corrosion behaviour of 13%Cr steel in CO_2 solutions at different pH*. SINTEF report STF16 F87108, Trondheim, 1987.
35. J. Sedriks: *Corrosion of Stainless Steels.* John Wiley&Sons, 2nd ed., 1996.
36. J. M. Drugli, T. Rogne, M. Svenning, S. Axelsen, J. Enerhaug: *SUPERMARTENSITIC STAINLESS STEELS '99*, Brussels, Belgium, 1999, Belgian Welding Institute, Belgium, pp. 315-322.
37. M. Pourbaix, *Corrosion*, 1970, vol. 26, pp. 431-438.
38. R. Østhus: *Karakterisering og Korrosjonstesting av 13%Cr-stål*. Project work at NTNU, Trondheim, 1999.
39. EFC publication no. 17: *Corrosion Resistant Alloys for Oil and Gas Production: Guidance on General Requirements and Test Methods for H_2S Service*. The Institute of Materials, London, 1996.
40. H. H. Strehblow: *Mechanisms of Pitting Corrosion*. ("Corrosion Mechanisms in Theory and Practice", P. Marcus and J. Oudar eds.). Marcus Dekker, 1995, pp. 201-237.

41. B. Baroux: *Further Insights on the Pitting Corrosion of Stainless Steels.* ("Corrosion Mechanisms in Theory and Practice", P. Marcus and J. Oudar eds.). Marcus Dekker, 1995, pp. 265-309.
42. S. Mat: *Pitting and Stress Corrosion Cracking of Stainless Steels in Sour Environments*. Doctor Thesis at University of Manchester (UMIST), Manchester, 1996.
43. M. Bjordal, J. M. Drugli, N.I. Nilsen: *Study of corrosion properties of alloyed 13%Cr stainless steel*. SINTEF report STF24 F00234. Trondheim, 2000.

PART II: FACTORS AFFECTING THE INITIATION OF PITTING CORROSION IN SUPER MARTENSITIC STAINLESS STEEL WELDMENTS

2.1 INTRODUCTION

The super martensitic stainless steels (SMSS) low in carbon have proved to be weldable with no or only limited use of post weld heat treatment (PWHT) and are therefore particularly useful as pipeline materials in the oil- and gas industry. During the last three years Statoil has installed more than 200km offshore flowlines of SMSS with Cr, Ni and Mo being the main alloying elements[1]. Duplex and super duplex steels have been used as welding consumables, but the need of higher yield and tensile strengths has enforced the development of matching consumables[2].

SMSS are delivered in the as-quenched and tempered condition and the microstructure is tempered martensite with considerable amount of finely dispersed stable austenite in addition to carbides[3,4,5,6]. The heat released by the welding process does, however, alter the microstructure and it will therefore vary across the HAZ because of the inherent temperature fluctuations[7]. The welding operation also modifies the internal weld surface due to high temperature oxidation reactions[8]. Although inert shielding gas is commonly used, the oxygen infiltration is sufficient to promote the formation of high temperature oxides. The type and thickness of the oxide layer will, in turn, depend on the imposed temperature-time pattern as well as the oxygen potential in the shielding gas. In a real welding situation chromium is believed to be oxidised to Cr_2O_3[8], while iron probably forms less stable oxides such as FeO and Fe_3O_4. Only in cases where the oxygen content in the shielding gas is sufficiently low, the oxide is assumed to be as protective as the parent surface oxide outside the HAZ[8]. In more oxidising atmospheres, however, coloured oxides are formed and the protectiveness of the oxides may be lower.

The martensitic and super martensitic stainless steels have been applied as tubing material for several decades and are known to exhibit acceptable corrosion properties[9]. During the last years the area of application of the SMSS have been extended to include pipelines and welded joints as well[10]. Corrosion tests performed on welds exposed to well streams containing small amounts of H_2S have shown that the resistance to sulphide stress corrosion cracking (SSC) is adequate. In practice, the phenomenon has only been observed in conjunction with preceding corrosion attacks, either pitting or active corrosion comprising the whole specimen[11]. This suggests that a certain amount of active corrosion is necessary to initiate SSC in such welds. Moreover, in the Åsgard Field Development Project the gas metal arc (GMA) welds made with 22%Cr duplex filler in the root pass were found to be most sensitive to pitting corrosion and hence to SSC in the high peak temperature region of the weld HAZ adjacent to

the fusion boundary[11]. Occasionally, attacks were also detected in more remote positions. Finally, in a series of SSC tests carried out on friction stir welds the pitting usually occurred in the transition region between the fully and the partially transformed HAZ[12].

Although SMSS weldments suffer from pitting corrosion in the HAZ, it is still unclear why this region is more susceptible to such corrosion than the adjacent parent material or weld metal. One possible explanation is that certain unfavourable microstructures or phases may form in parts of the HAZ during welding. Another possibility is that the oxide scale formation accompanying the welding operation is the main cause of the problem, e.g. in combination with some underlying microstructural effect. Thus, the main objective of the present investigation is to examine the HAZ microstructure evolution and the associated surface oxidation reactions more in detail and then clarify to what extent these factors contribute to the initiation of pitting corrosion in SMSS weldments during service.

2.2 EXPERIMENTAL

2.2.1 Materials

The base material was received in the form of 10'' diameter pipe from a Japanese steel manufacturer (Sumitomo) through the Åsgard Project. The wall thickness was 20mm and the pipe was delivered with pickled surfaces, using HNO_3 + HF and H_2SO_4. The steel chemical composition is shown in Table 2.1. The base composition of approximately 12%Cr, 2.5%Mo and 6.5%Ni places this pipe material in the "high alloyed" category of the SMSS, with a martensite start transformation temperature (M_s) of about 220°C. The desired martensitic microstructure is achieved by applying a standard heat treatment schedule, involving quenching from 900°C followed by tempering at 620°C.

Table 2.1. Chemical compositions of pipe material, filler wire and single root pass weld (in wt%).

	C	Cr	Mo	Ni	P	S	Si	Mn	V	Cu	W	Co	Al	Ti
Pipe	0.01	12.2	2.5	6.4	0.018	0.002	0.12	0.48	0.04	0.08	0.03	0.11	0.03	0.12
Wire	0.012	12.37	2.65	6.37	0.01	0.001	0.50	0.67						
Weld	0.011	12.2	2.7	6.5				0.49		0.06				

2.2.2 Welding conditions

Girth welds were made in a remotely controlled welding chamber, using the gas tungsten arc (GTA) welding process. A Ø1mm Thermanite 13/06 filler wire (produced by Böhler/Thyssen) was selected as welding consumable. This is a "high alloyed" wire developed for matching the SMSS base material, with chemical composition as given in Table 2.1.

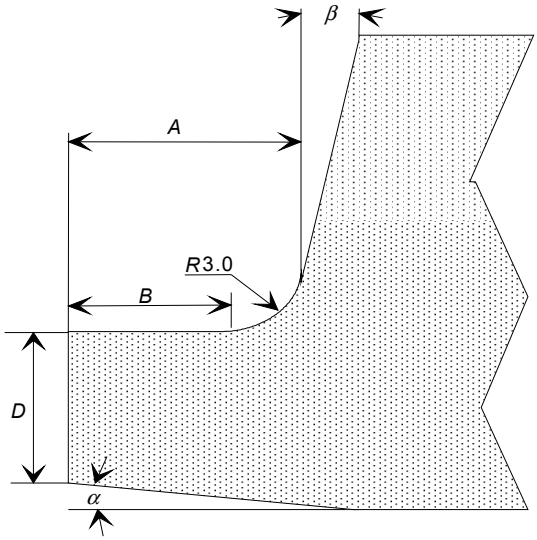

D= 2.75 ± 0.25 mm, B= 2.25 ± 0.2 mm,
A= 5.25 ± 0.3 mm, α= 6° and β= 7°

Figure 2.1. Schematic diagram showing the pipe bevel preparation.

The two pipe ends to be joined were bevelled in a lathe machine, and the final groove joint geometry is shown in Figure 2.1. The root face (land thickness) was machined to 2.75 mm, and no misalignment between the pipes was allowed. The welding was performed with zero root gap. The pipe was rotated with the torch in a fixed position. The torch was located in the 11 o'clock position during root pass welding and 12 o'clock position for filler and cap layers, i.e. the 1G position. All welding was performed with pulsed current. The shielding gas composition was 70%He and 30%Ar (vol.-%). No extra shielding gas was supplied from the bottom side of the weld, but the chamber was flushed with inert gas mixture before welding. Both single pass and full pass welds were produced, using the welding parameters listed in Table 2.2. The chemical composition of the former weld is given in Table 2.1.

Table 2.2. Summary of welding parameters.

Pass type	Welding current (I_p/I_b), [A]	Arc voltage [V]	Weaving amplitude [mm]	Weaving rate [mm/s]	Welding speed [mm/s]	Wire feed rate [m/min]	Dwell time on high pulse [ms]
Root weld	170/90	13	1.0	2.5	1.0	0.50	400
Bottom layer	200/100	13	3.0-3.25	6.0-6.5	1.0	0.90	500
Layers 1 and 2	210/110	13	3.0-3.25	6.0-6.5	1.0	1.3	500
Layers 3, 4, 5	220/120	13	2.75-3.5	5.5-7.0	1.0	1.3	500
Layers 6 and 7	220/120	13.5	1.0-4.5	2.0-9.0	1.0	1.3	500
Cap layer	220/120	14	6.0	6.0	1.0	1.55/0.75	400

The oxygen content in the chamber was measured to be 150ppm (by volume) before welding and less than 1ppm after deposition of the single pass weld. Similarly, the chamber contained initially 250ppm of oxygen before the root layer of the full pass weld was deposited.

2.2.3 Metallographic examination

The specimens used in the metallographic examination were taken from the root surface of the single root pass weld, as this is the most critical region with respect to initiation of pitting corrosion. After machining the specimens were embedded in epoxy and ground with 1000grit paper before polishing and etching with Marble to unravel the microstructure. Occasionally, a special in-house variant was used in order to achieve the required contrast. The microstructure was subsequently examined in a light microscope.

The variation in the hardness across the root region was measured by placing a number of Vickers pyramid impressions at fixed positions on both sides of the fusion boundary, sampling the weld metal, the HAZ and the base metal. To ensure a high degree of confidence in these measurements 4 independent impressions were made at each location. The mean values were subsequently calculated and reported. The Vickers hardness measurements were carried out using a PC-controlled Wolpert V-Testot DA6552 sclerometer and a load of 1kg.

2.2.4 Characterisation of weld surface oxides

The root surface of both types of welds was covered with a colourful and visible oxide. This pattern bears a close resemblance to the one observed on actual flowline welds, indicating that the oxygen partial pressure in the artificial He-Ar chamber atmosphere is comparable with that experienced in a real welding situation.

The oxide on the single root pass weld surface was analysed by MATS-UK in Warrington, England, using the sputtered neutral mass spectrometry (SNMS)

analysis technique[13,14]. SNMS is a development of the secondary ion mass spectroscopy (SIMS) technique, where the sputtered neutral atoms that are ejected from the sample due to the ion bombardment are ionised and analysed in a mass spectrometer. Because of the roughness of the actual machined and oxidised surface, it was not possible to detect any sharp transition between the oxide and the metal. The surface concentration of the main alloying elements Fe, Ni, Cr and Mo along with O is therefore recorded as a function of the etching depth in the SNMS analysis. The composition data were subsequently normalised to 100% to allow for variations in the sputtering yield. In the present investigation the oxide/metal boundary is defined as the depth where the oxygen concentration has dropped to 1/3 of its maximum value. The estimated uncertainty in the measured oxide layer depth is, according to the laboratory, about ±40% under the prevailing circumstances.

2.2.5 Corrosion testing

The purpose of the corrosion tests was to establish the location of the pitting initiation by generating a limiting number of pits. These tests were carried out at ambient temperature and pressure, using a combination of potentiodynamic and potentiostatic measurements in an H_2S-containing electrolyte and galvanostatic measurements in an H_2S-free electrolyte. A platinum wire was used as counter electrode, while a saturated calomel electrode (SCE) was used as reference electrode.

In the corrosion tests with H_2S a Solatron SI 1280 unit, controlled by the PC programme ElektroChem, was used for sweeping the potential of the specimens from the open circuit potential E_{CORR} to a hold potential E_{HOLD} above the pitting potential E_P with a sweep rate of 1mV/min. As E_{HOLD} was reached the Solatron unit was replaced by a Wenking MP 87 potensiostat maintaining the potential at E_{HOLD}. The current was continuously recorded during the polarisation. Prior to testing the side edges apart from the intact root surface were first cut and ground with a 500grit paper and then covered with a layer of bees wax to prevent corrosion. Further details are given in Table 2.3. Note that in tests 1 to 4 and 6 to 8 the intact root surfaces were exposed, while in test 5 only the polished side edge was exposed. Moreover, in tests 9 to 11 pickled root surfaces were exposed. The pickling was carried out in a 20% HNO_3, 5% HF solution at 60°C for 30 seconds.

Table 2.3. Summary of experimental conditions in the combined potentiodynamic and potentiostatic corrosion tests with H_2S-containing electrolyte.

Test series	E_{CORR} [mV SCE]	E_{HOLD} [mV SCE]	E_{HOLD}-E_{CORR} [mV]	Sweep rate [mV/min]
1	-526	-295	231	1
2	-535	- 355	180	0.16
3	-541	-360	181	1
4	-547	-425	122	1
5	-545	-360	185	1
6	-528	-403	125	1
7	-522	-402	120	1
8	-537	-409	128	1
9	-548	-280	268	1
10	-540	-394	146	1
11	-545	-260	285	1

The electrolyte used was artificial formation water with 3.93*M* NaCl and a *pH* of approximately 4.5, which was adjusted by the addition of NaAc (0.049*M*) and HCl. The electrolyte was stored in a separate tank where the oxygen was removed by nitrogen purging for 24hours. Before transfusing the electrolyte to the actual test chamber (glass cell) nitrogen was purged through the empty glass cell for 2 hours. The gaseous mixture of H_2S (4%) and CO_2 was then bubbled through the electrolyte (in the glass cell) for 24hours prior to the polarisation of the specimens. The supply of the corrosive gaseous mixture was maintained throughout the test.

In the corrosion tests without H_2S, a Solatron SI 1286 unit, controlled by the PC programme Galvanostat, was used to carry out the galvanostatic measurements. When E_{CORR} stabilised the galvanostat was switched on, generating a constant current density of approximately 0.8μA/cm^2, which was sufficient to passivate the steel surface. The first signs of fluctuations in the potential indicate that the pitting corrosion potential E_P is reached and pits start to form. Prior to the galvanostatic measurements the side edges apart from the intact root surface were cut and ground with a 1000 grit paper, and a hole was drilled for the connection of the platinum wire. The electrolyte was a 1*M* NaCl solution that had had been purged with nitrogen gas for more than 6 hours before the specimens were immersed.

2.3 RESULTS AND DISCUSSION

In the following, the results will be presented and discussed consecutively throughout the text, starting with the HAZ microstructure evolution in the single pass root weld.

2.3.1 Structural zones within the weld HAZ

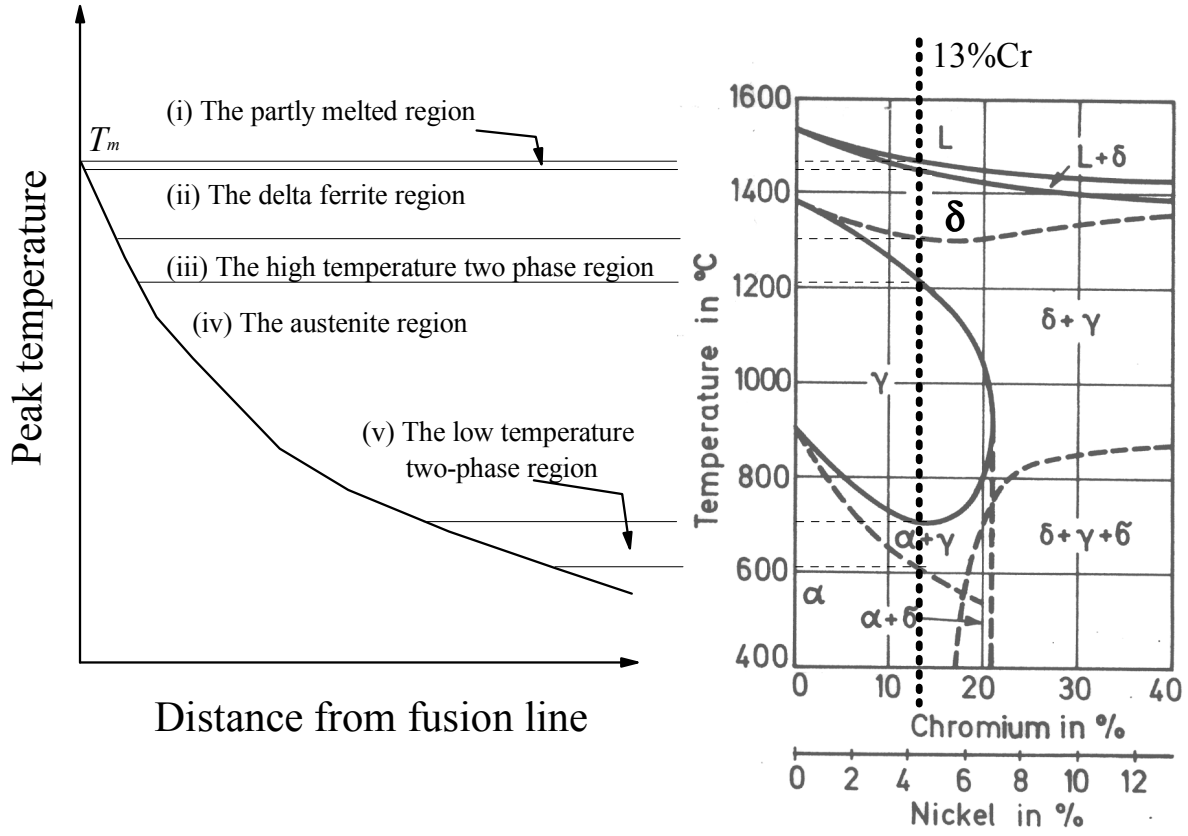

Figure 2.2. Schematic diagram illustrating the structural changes that occur within the HAZ of a single pass SMSS weld according to the Fe-Cr-Ni phase diagram.

The ternary Fe-Ni-Cr phase diagram[15] provides a good starting point for a presentation and subsequent interpretation of the results obtained in the optical metallographic examination. Figure 2.2 shows, in principle, the structural changes that occur in the HAZ during welding. This is a schematic diagram, where the variation in the peak temperature with position in HAZ has been coupled with a typical phase diagram for SMSS.

Figure 2.2 suggests that the HAZ of a single pass root weld can be subdivided into the following five structural regions:
(i) The partly melted region, where incipient melting of the newly formed delta ferrite occurs on heating. This region is located adjacent to the fusion boundary.

(ii) The delta ferrite region, where all transforms to delta ferrite during heating. Due to the high peak temperatures involved, significant growth of the delta ferrite grains may occur at elevated temperatures.
(iii) The high temperature two-phase region, characterised by partial transformation of the austenite to delta ferrite during heating.
(iv) The austenite region, where full transformation to austenite occurs on heating.
(v) The low temperature two-phase region, characterised by partial transformation of the tempered martensite to austenite during heating.

In general, the results from the metallographic examination were found to be in good agreement with the reaction scheme outlined in Figure 2.2. As shown in Figure 2.3 (a), the width of the partially melted region is approximately 1mm and the average grain size about 250μm. The structure within the grain interiors is martensite, which forms on subsequent cooling. Moreover, about 1mm from the fusion boundary, a fine-grained martensite surrounded by ferrite is observed, as indicated in Figure 2.3 (b). Under the prevailing circumstances it is reasonable to assume that the delta ferrite forms along the prior austenite grain boundaries during heating. On subsequent cooling, the natural retransformation to austenite (and thus martensite) is suppressed because of the high cooling rates involved, which means that most of the delta ferrite is retained down to room temperature. Hence, this zone conforms to the high temperature two-phase region in Figure 2.2. At a distance 1 to 5mm from the fusion boundary a fine-grained martensitic microstructure is visible, as shown in Figure 2.3 (c). This zone has fully transformed to austenite on heating at the same time as some of the carbides initially present in the parent material have dissolved, giving rise to a weaker etching response compared with the base metal. The low temperature two phase region is observed about 5 to 6.5mm from the fusion boundary. Referring to Figure 2.3 (d), the microstructure consists of a mixture of tempered and untempered (virgin) martensite, where the brightest grains represent the virgin martensite that form as a result of the austenite decomposition on cooling. In general, the etching response of this zone to Marble is very strong, indicating that a high density of carbides is present within the grain interiors. Finally, a martensitic microstructure with weak etching response can be detected about 6.5 to 8mm from the fusion boundary (not shown here). Here no evidence of re-austenitising could be found, indicating that the microstructure is tempered martensite.

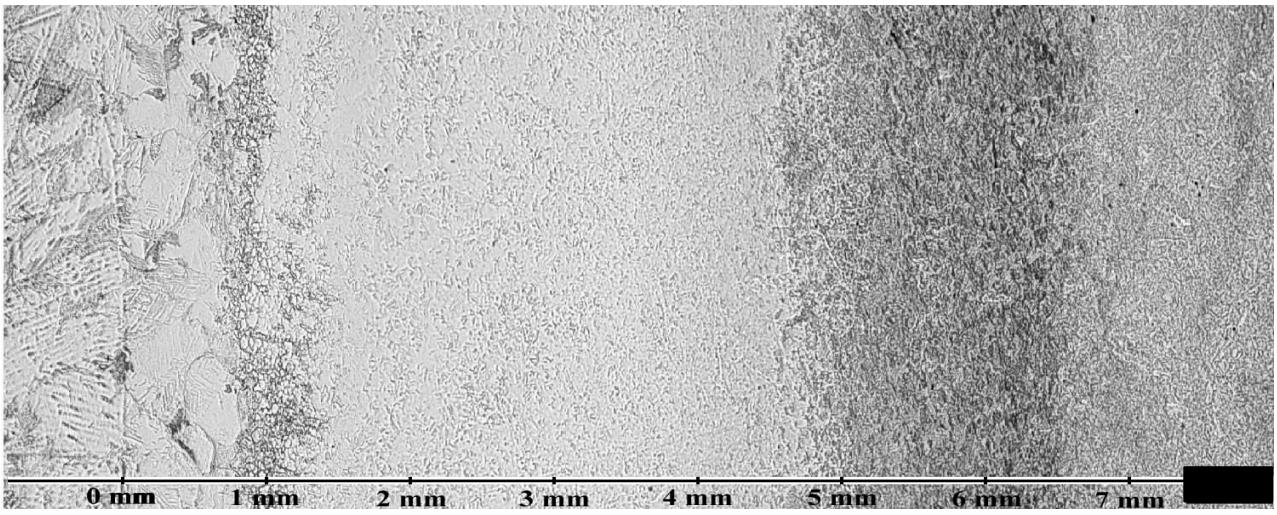

(a)

(b)

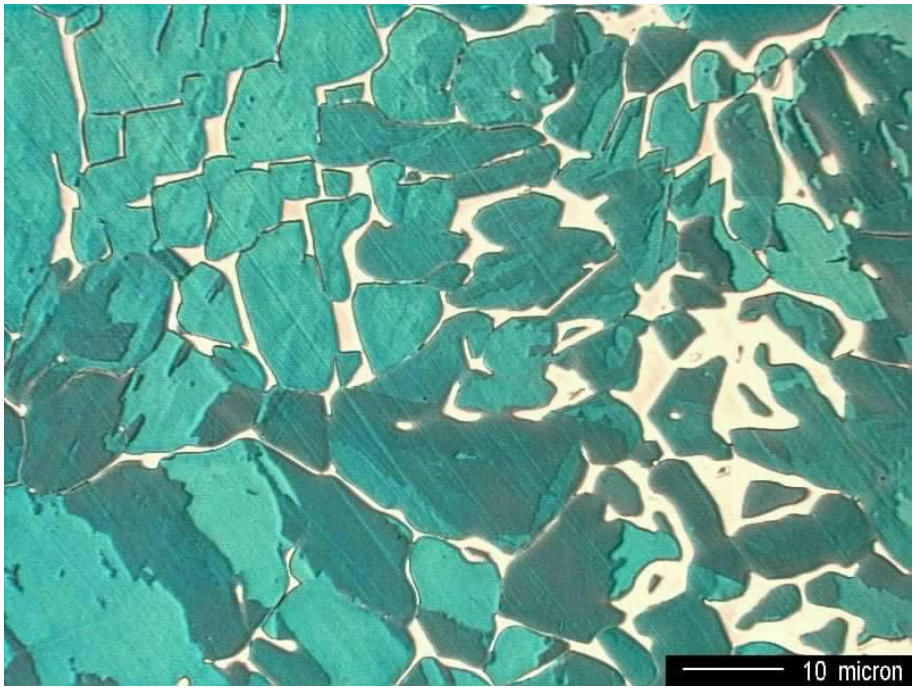

(c)

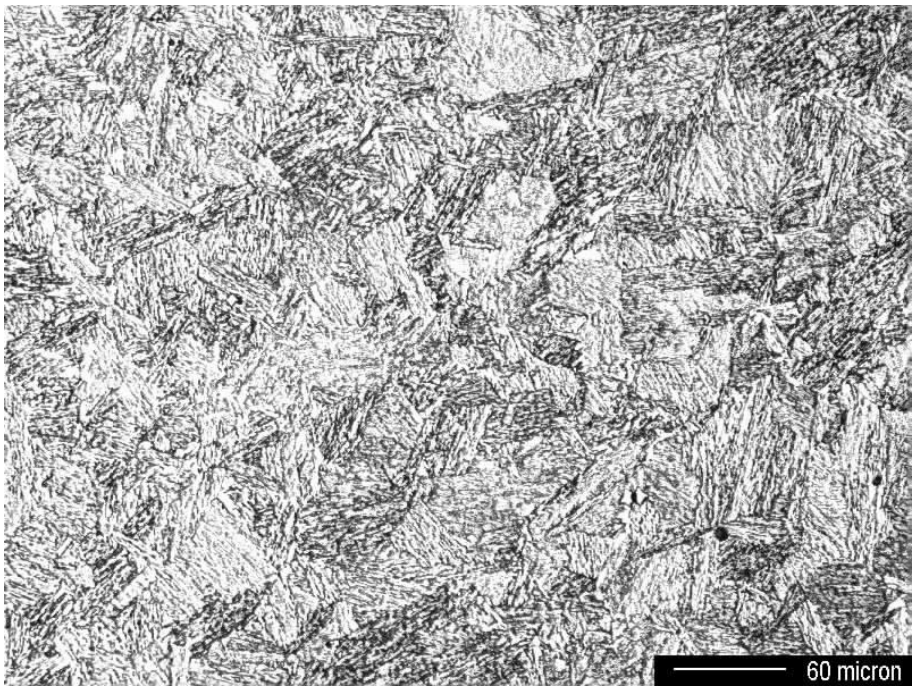

(d)

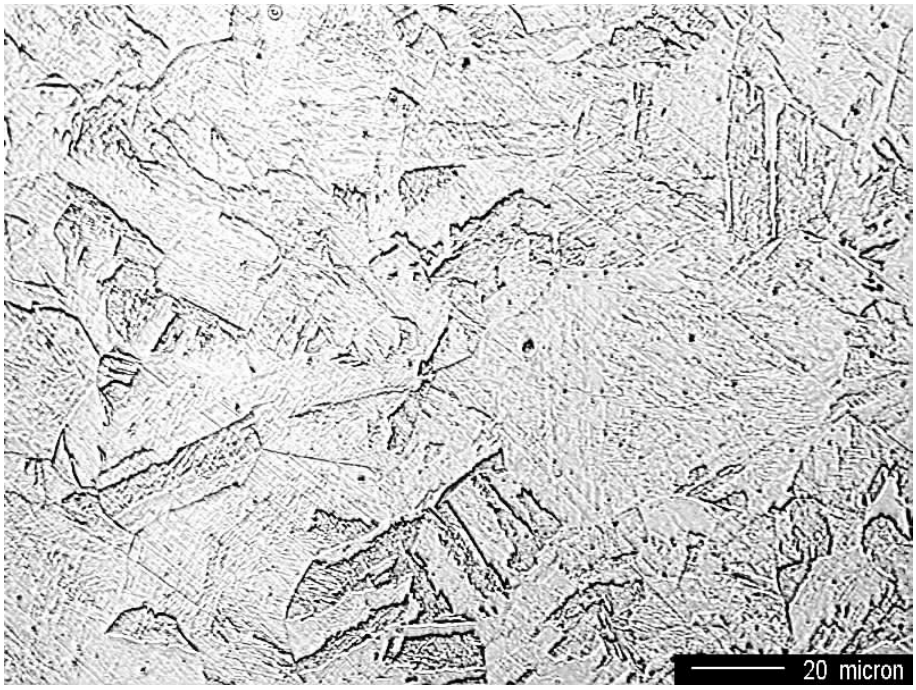

Figure 2.3. Optical micrographs of typical HAZ microstructures in the single pass weld; (a) Overview of the partly melted region and the adjacent weld HAZ (position zero refers to fusion boundary), (b) Close-up of the high temperature two phase region showing a fine grained martensite surrounded by ferrite, (c) Close-up of the fully transformed (austenite) region showing details of the fine grained martensite structure, and (d) Close-up of the low temperature two phase region showing a mixture of tempered and untempered martensite.

2.3.2 HAZ hardness profile

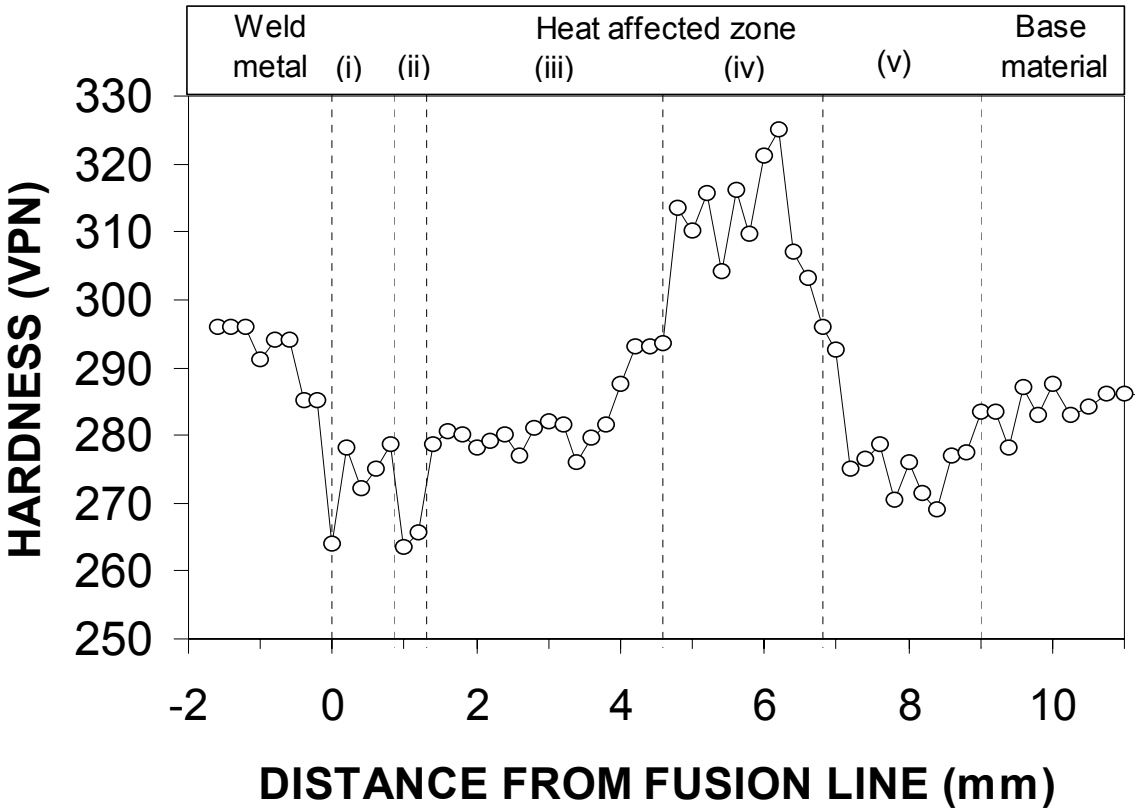

Figure 2.4. Measured hardness profile across the weld zone. The roman numbers in the graph refer to the structural zones defined in Figure 2.2.

The hardness profile shown in Figure 2.4 provides a further visualisation of the HAZ microstructure evolution. Here the structural zones, as observed in Figures 2.2 and 2.3, are indicated in the upper part of the diagram. It follows that a reduced hardness is observed within the delta ferrite region, the high temperature two-phase region as well as within a narrow tempered region adjacent to the base metal. This softening is the result of the delta ferrite formation and the martensite tempering occurring during welding. Conversely, the low temperature two-phase region is characterised by a significant hardness increase, whereas the hardness within the austenite region is more comparable with that of the base material.

The high hardness of the former region is probably due to the presence of untempered (virgin) martensite that form during the partial transformation, as shown previously in Figure 2.3 (d). The low hardness of the fully austenitised

region is more surprising, considering the fact that the transformation product also is untempered martensite, see Figure 2.3 (c). This suggests that considerable amounts of retained austenite are present between the martensite laths at room temperature, which completely overrides the hardness increase provided by the virgin martensite under the prevailing circumstances.

2.3.3 Oxide layer thickness

As shown in Figure 2.5, the single pass root weld surface was covered with a colourful oxide visible for the naked eye. At first glance the colour bands seem to be associated with a specific structural zone within the HAZ and in terms of position the dark band coincides with the tempered region adjacent to the base material.

However, this incident is probably fortuitous in the sense that outermost part of the coloured zone, in practice, reflects the lower temperature needed for iron oxidation during welding. The primary cause for the colour bands is thought to be constructive interference. Under such conditions the relationship between the wavelength of visible light λ (in nm) and the transparent oxide layer thickness d (also in nm) can be expressed as[16]:

$$d = \frac{\lambda}{2 \cdot n} \tag{2.1}$$

where n is the index of refraction, and is assumed to be 2.55 for Cr_2O_3 and between 2.4 and 3.0 for iron oxides[17].

Some values of the colour-wavelengths correlation and the corresponding oxide thickness are given in Table 2.4, taking n = 2.55 as a lower limit. According to these data, the thickness of the colourful part of the oxide layer should be in the range of 80 to 150nm.

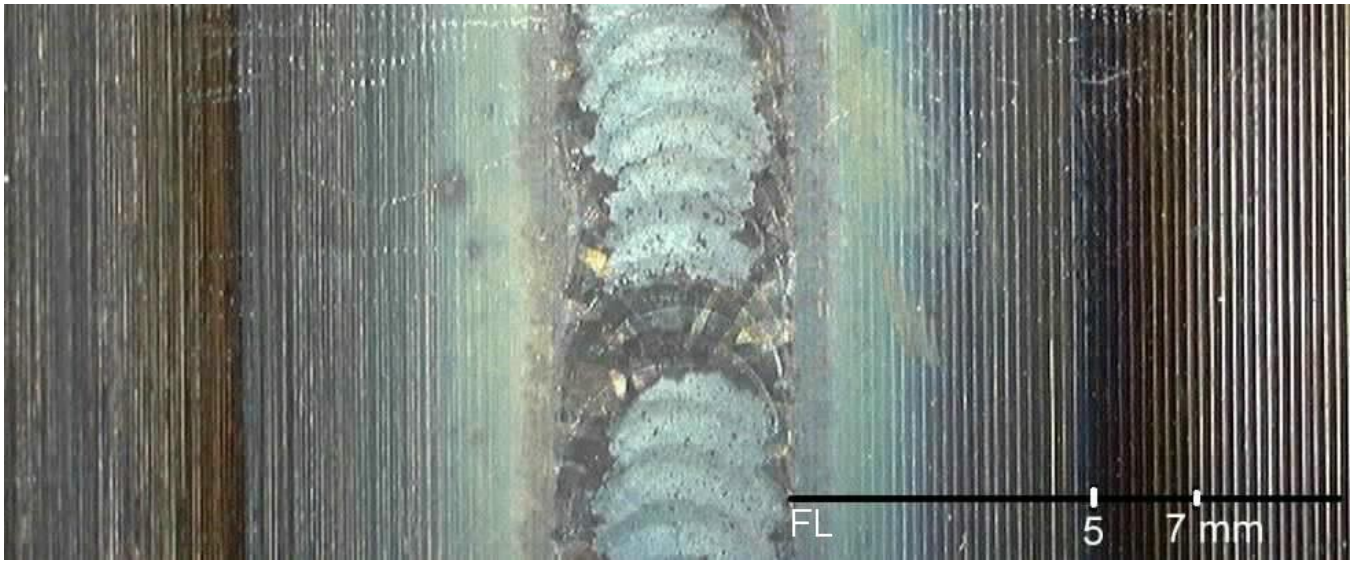

Figure 2.5. Macrograph of the single pass root weld surface showing the coloured regions of the HAZ.

The SNMS analysis combined with ion gas sputtering made it possible to make depth profiles at selected positions within the HAZ. Figure 2.6 shows a compilation of measured oxide layer thickness and corresponding wavelengths, as calculated from Equation (2.1) and input data from Table 2.4. In general, the agreement is good, which means that the SNMS data provide a fair estimate of the variation in the oxide layer thickness across the HAZ. It follows that the thickness is about 250nm close to the fusion boundary and approximately 50nm within the more remote regions of the weld HAZ.

Table 2.4. The relationship between the wavelength λ of visible light and the corresponding thickness d of a transparent oxide.

Colour	Wavelength λ (nm)	Thickness d (nm)
Violet (limit)	400	78
Blue	450	88
Cyan	500	98
Green	550	108
Yellow	580	114
Orange	600	118
Red	650	127
Red (limit)	750	147

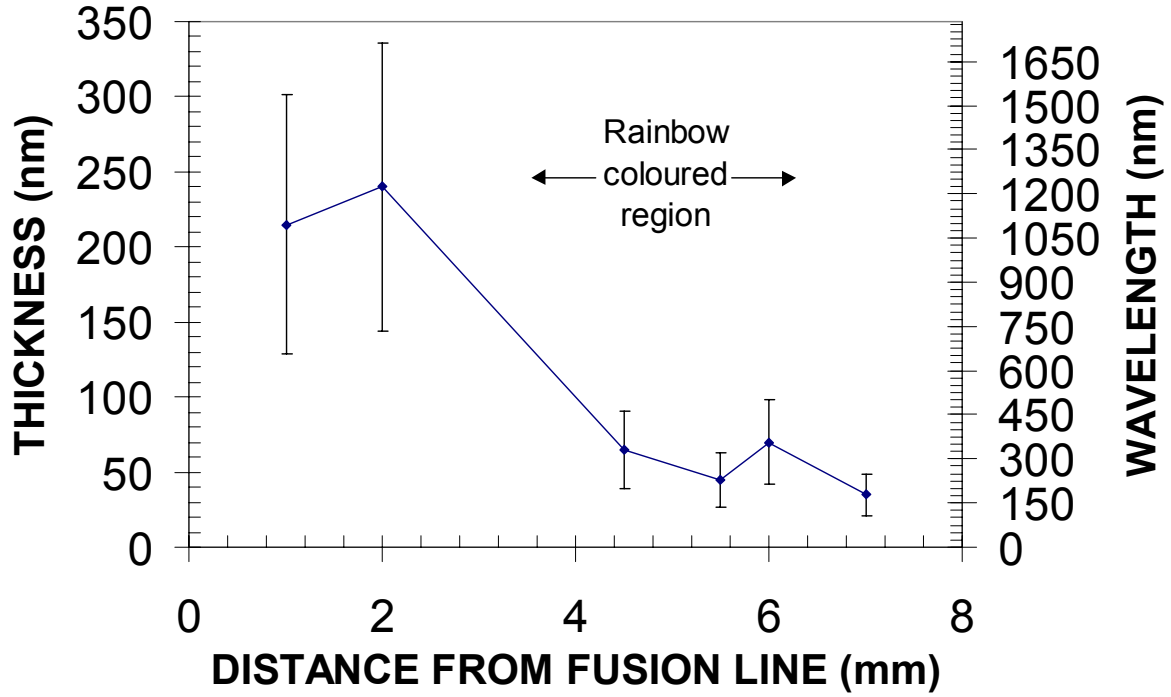

Figure 2.6. Measured oxide layer thickness based on outputs from SNMS analysis and corresponding wavelengths, as calculated from Equation (2.1) and taking $n = 2.55$.

2.3.4 Spatial variations in the oxide layer composition

The SNMS element analyses also revealed evidence of spatial variations in the oxide layer composition, both in-depth and with position across the HAZ. Considering the heavily coloured region of the HAZ (i.e. 1, 4.5 and 6mm from the fusion boundary) Fe is enriched in the outermost oxide, while Cr is enriched in the layers beneath. This can be seen from the plots in Figure 2.7 (a), (b), and (c), respectively. However, just outside the coloured region (i.e. 7mm from the fusion boundary), the oxide appears to be pure Cr_2O_3 with no indication of iron enrichment, as shown in Figure 2.7 (d). The sharp transition in the oxide layer composition at this position is better illustrated in Figure 2.8, which shows a SNMS image of the surface oxide layer about 7mm from the fusion boundary. It follows that the iron-rich oxide suddenly disappears at a given position in the HAZ, from whence pure chromium oxide is observed. The latter oxide is probably the same type as the one being present in the parent material, indicating that no significant surface oxidation occurs outside the coloured region during welding. Consequently, the colour bands observed across the HAZ probably arise from constructive interference due to variations in the iron-chromium oxide layer thickness, whereas the sharp demarcation line towards the

base material mainly reflects an abrupt change in the oxide composition from a mixed (spinel) type to pure Cr_2O_3.

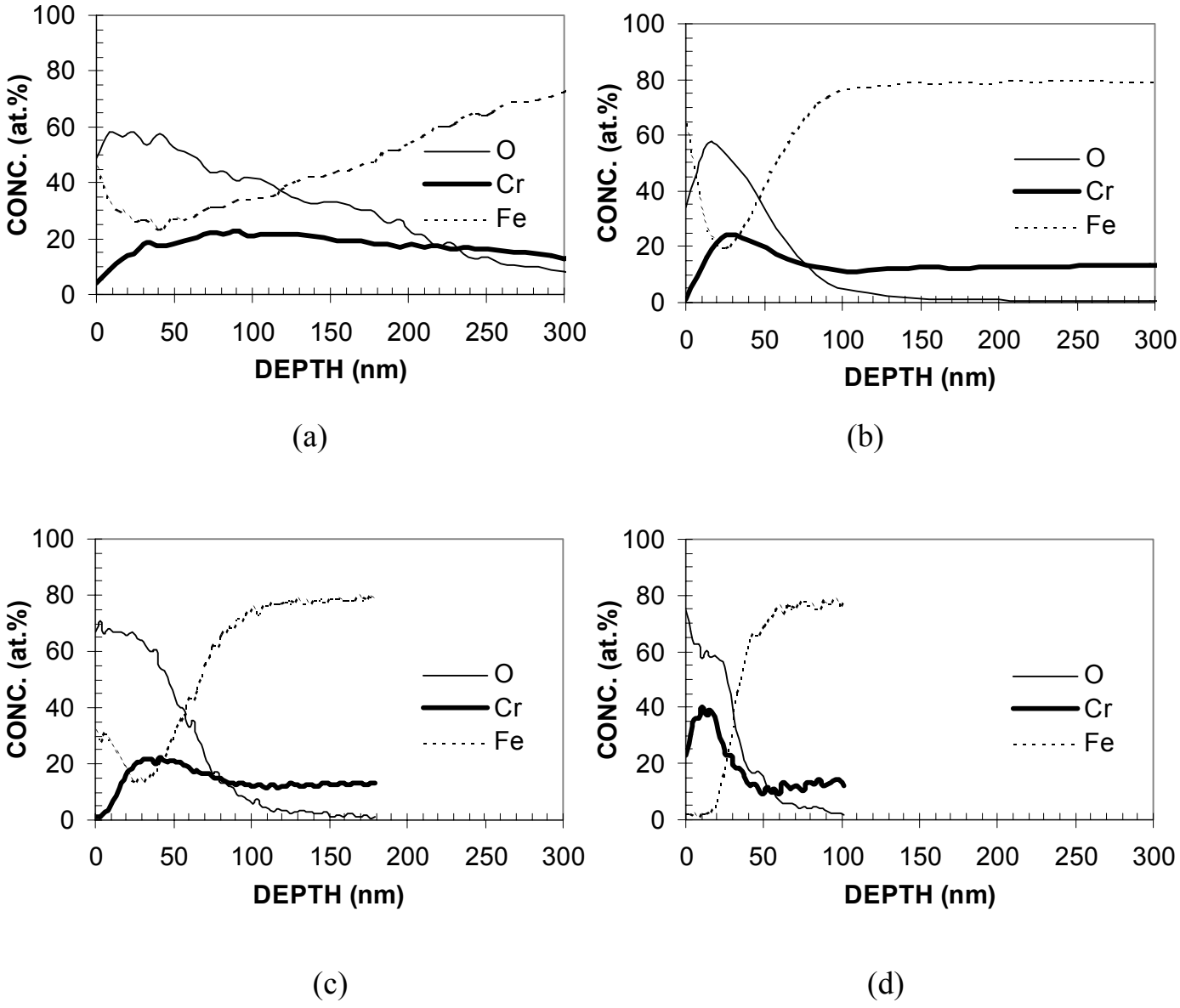

Figure 2.7. Measured oxide layer compositions at varying depths and positions across the weld HAZ; (a) 1mm from the fusion boundary, (b) 4.5mm from the fusion boundary, (c) 6mm from the fusion boundary, and (d) 7mm from the fusion boundary. For clarity, the alloying elements Ni and Mo are not shown the graphs.

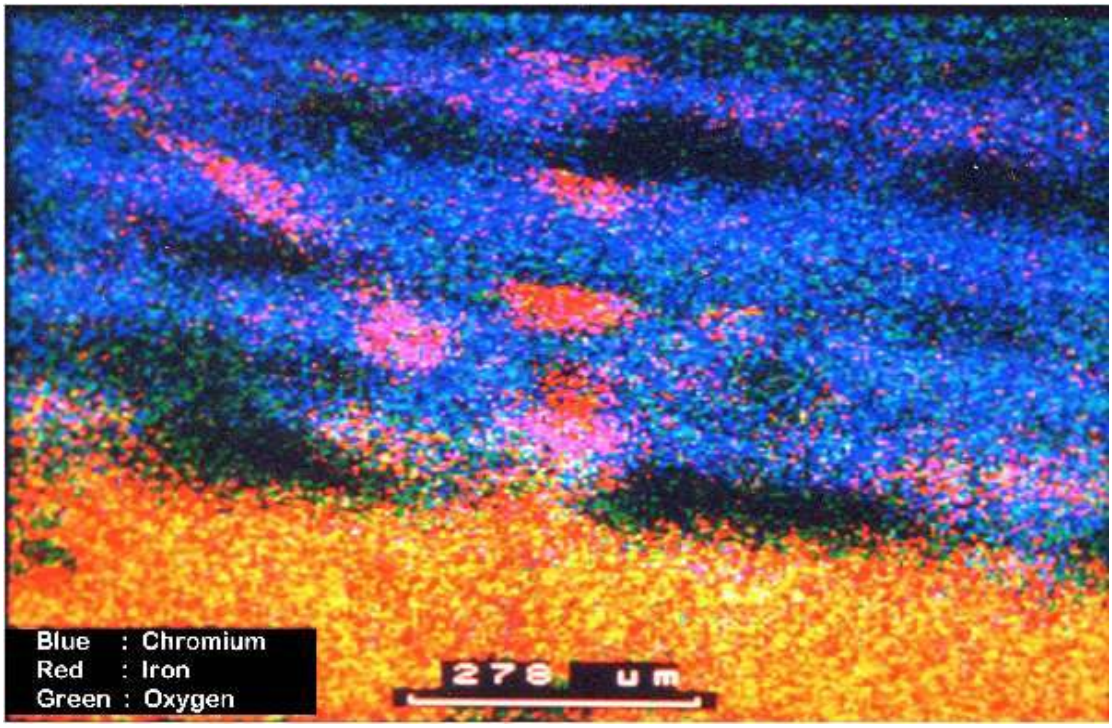

Figure 2.8. SNMS image of the outermost surface oxide layer about 7mm from the fusion boundary.

2.3.5 Initiation of pitting corrosion in the presence of H_2S

The corrosion attacks observed after the combined potentiodynamic and potentiostatic tests in the H_2S-containing electrolyte were confined to two distinct regions of the HAZ, i.e. the region adjacent to the fusion boundary, and a narrow zone located approximately 6mm from the fusion boundary. The appearances of the pits were different in the two regions. Only a limited number of pits could be observed in the region close to the fusion boundary, but they were generally deeper than the numerous and more shallow pits appearing in the narrow zone 6mm from the fusion boundary. Pits could also be detected within other HAZ regions, but these were more randomly distributed and appeared less frequent. The test conditions employed are summarised in Table 2.3. Figure 2.9 shows the corroded surface of the specimen from test 1, where the black spots represent the pits generated during testing.

In test 1 E_{HOLD} was –295mV SCE, but was lowered in the subsequent tests to reduce the total number of pits generated. The high number of pits can be explained by the stabilisation of otherwise unstable pits in the presence of adsorbed sulphur on the metal surface, which stems from dissolved H_2S[18]. In test 5, where the polished side edge of the specimen was exposed to the

electrolyte, pitting occurred in the base metal rather than in the weld HAZ. Similarly, by removing the surface oxide from the root side of the weld the initiation point for pitting corrosion was shifted to the base material, leading to incipient crevice corrosion between the specimen and the protecting bees wax.

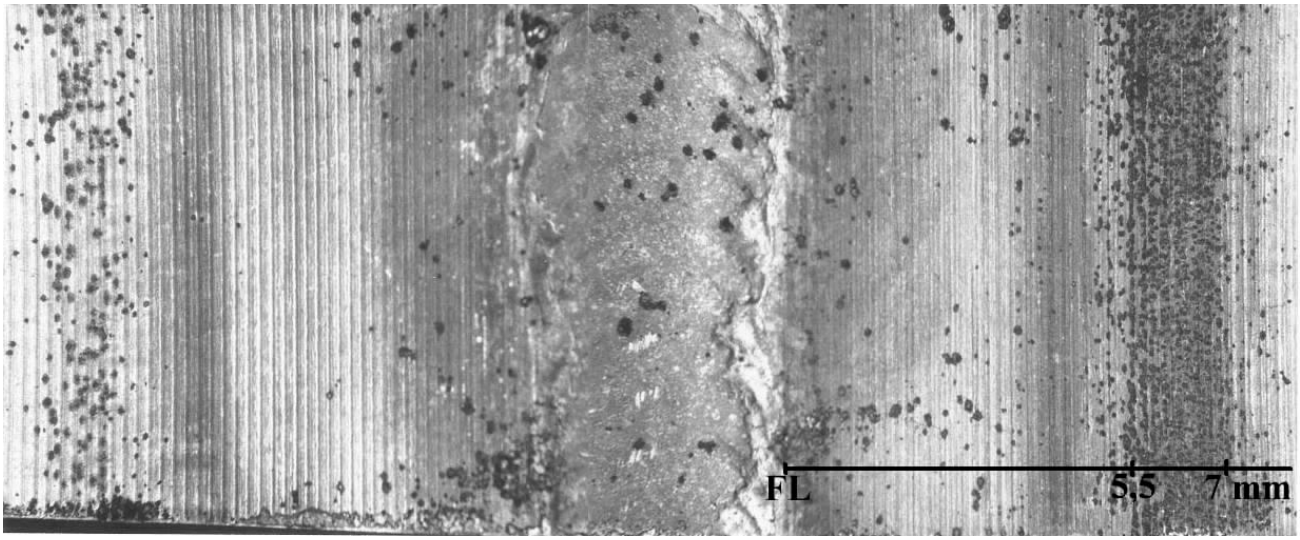

Figure 2.9. Optical macrograph showing the corroded surface of the specimen from test 1 (H_2S-containing electrolyte). The black spots indicate pits that are generated during the corrosion test.

2.3.6 Initiation of pitting corrosion in the absence of H_2S

The use of galvanostatic measurements in an H_2S-free environment offers a special advantage in that the pit formation can be controlled to an extent that allows a more exact identification of the initiation site.

Table 2.5. Summary of experimental conditions in the galvanostatic corrosion tests with an H_2S-free electrolyte.

Specimen	Type of weld	Root surface condition	E_{CORR} [mV SCE]	E_P [mV SCE]
A	Single root pass weld	As-welded	-667	-185
B	Single root pass weld	As-welded	-701	-190
C	Single root pass weld	As-welded	-640	-75
D	Single root pass weld	As-welded	-674	-220
E	Single root pass weld	Ground	-705	-90
F	Full pass weld	As-welded	-728	-211
G	Base material	Ground	-700	-206

The different samples and test conditions employed are summarised in Table 2.5. Note that in the corrosion tests referring to samples (A) and (B) the current

was switched off immediately after the pitting potential was reached in order to confine the pit formation to the weakest part of the weld HAZ. In sample (E) the surface oxide was removed by grinding prior to testing, whereas sample (G) representing the base metal was included as a reference.

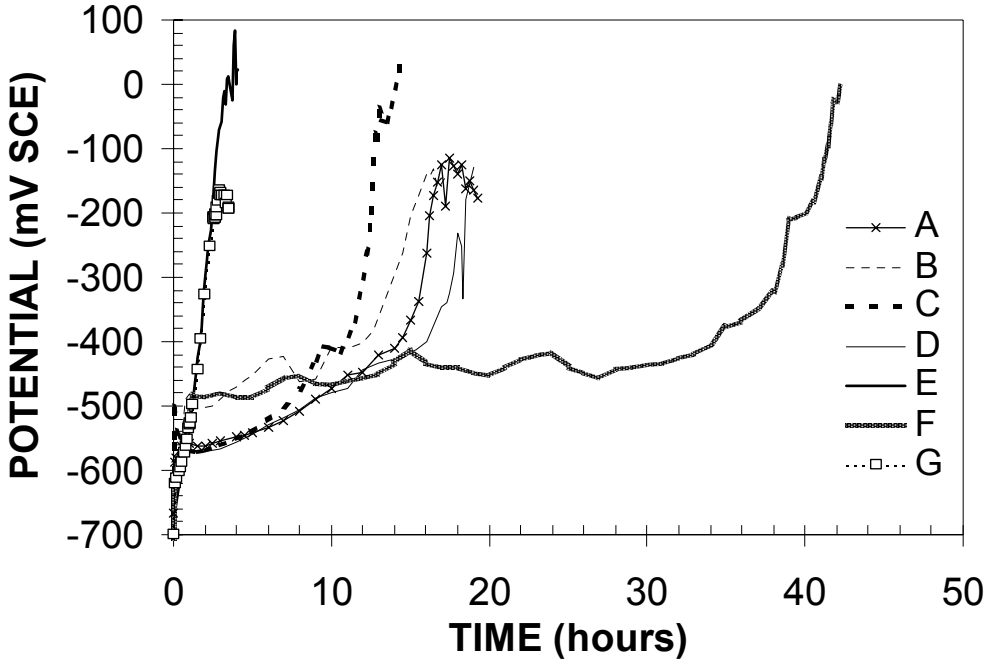

Figure 2.10. Summary of the results obtained in the galvanostatic corrosion tests (H_2S-free electrolyte). The experimental conditions are defined in Table 2.5.

Figure 2.10 shows the characteristic evolution of the potential with time during the galvanostatic measurements. Initially, E_{CORR} decreased to values below −650mV SCE within a few hours of the free exposure period. Subsequently, a peculiar passivation process took place, where the potential first increased rapidly as the galvanostat was switched on and then started to level-off until some sort of plateau was reached after a few minutes. Eventually, the potential began to increase again until the value exceeded the pitting potential.

A closer inspection of Figure 2.10 reveals that the passivation process occurs slower on the oxidised root weld surfaces compared with the ground surfaces. This follows from a comparison between the curves representing the base material specimen (G) and the ground single root pass weld specimen (E), on the one hand, and the single root pass weld specimens (A) through (D) on the other. In fact, the time to reach the −200mV SCE potential is less than 3 hours during testing of the former specimens and approximately 15 hours for the iron oxide contaminated specimens. The passivation process occurred even slower in the

full weld sample (F), reaching the −200mV SCE potential after about 40 hours. In both cases E_P was in the range of −240 to −100mV SCE.

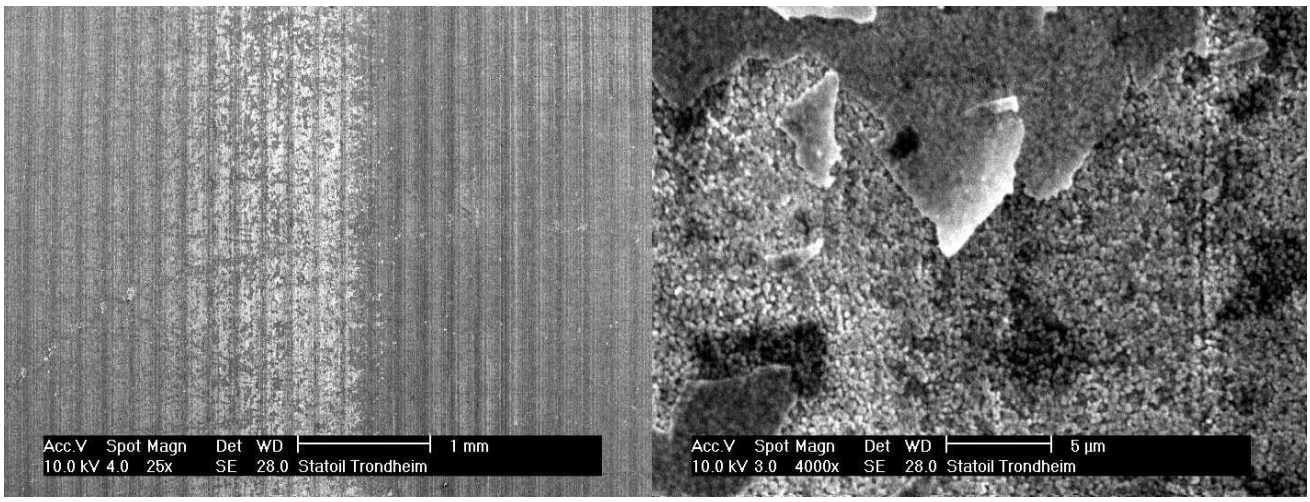

(a) (b)

Figure 2.11. SEM micrographs of the corroded region approximately 6mm from the fusion boundary following galvanostatic testing in an H_2S-free environment, (a) Overview, (b) Close-up showing details of the pitting corrosion initiation.

Also in the galvanostatic corrosion tests the initiation of pitting corrosion took place in the outermost part of the coloured region in Figure 2.5, i.e. about 6 mm from the fusion boundary. The first attacks were hardly visible for the naked eye, but could be observed in the scanning electron microscope (SEM). Figures 2.11 (a) and 2.11 (b) show an overview and a close-up, respectively of the corroded area in specimen (A). It follows that the early stage of pitting corrosion appears to occur by spalling of the surface oxide in this particular region. As the pitting process proceeds, the pitting attacks become scattered to other parts of the specimens, but not to the narrow zone adjacent to the fusion boundary, where pitting was observed in the presence of H_2S. The other specimens tested in the as-welded condition revealed a similar pattern, although polarisation in some cases were carried out beyond the point of initiation, leading to pit formation at various sites across the weld HAZ.

2.3.7 Summary of experimental findings

Both the combined potentiodynamic and potentiostatic 2corrosion tests and the galvanostatic corrosion tests indicate the existence of a weak iron oxide contaminated zone in the weld HAZ approximately 6mm from the fusion boundary, where the pitting initiation occurs. A similar zone also exists in the full pass weld, which has undergone several heating cycles. The corrosion is presumably initiated in the bottom of cracks that are present in the oxide. At the

same time the observation of flakes of iron-rich chromium oxide in the corroded region suggests that a spalling mechanism is operative and responsible for the pitting initiation, allowing crevice corrosion to occur beneath the oxide. The spalling process starts within a narrow region approximately 6 mm from the fusion boundary, where the contaminated chromium oxide is thinnest. If the corrosion process is allowed to proceed, the pits become eventually scattered to other parts of the specimen, leading to pitting attacks across the entire weld zone as well as in the base metal. As H_2S is introduced, the region close to the fusion boundary becomes susceptible to localised corrosion, covering both the delta ferrite region *(ii)*, the high temperature two-phase region *(iii)* and part of the austenite region *(iv)* in Figure 2.2. This last region is the most oxidised part of the HAZ. Thus, the corrosion resistance is mainly determined by the nature of the oxidised metal surface and less by the underlying HAZ microstructure.

2.3.8 Practical implications

In general, high temperature oxidation of metals and alloys is an intricate process that is difficult to map out in detail. However, it seems to be well established that the protectiveness of an oxide can be destroyed by exposure to oxygen at elevated temperatures, leading to undesirable stress build and subsequent crack formation on cooling[19,20]. This is clearly the case during welding of SMSS, where infiltration of oxygen in the surrounding gas atmosphere tends to deteriorate the corrosion resistance of the parent chromium oxide. Thus, the nature of the surface oxide appears to be a key issue under the prevailing circumstances, and in search of practical solutions to the problem the tolerance of the steel to high temperature oxidation should be duly considered.

2.4 CONCLUSIONS

The basic conclusions that can be drawn from this investigation can be summarised as follows:

The HAZ of a single pass SMSS weld can be divided into five different regions, each zone being characterised by a specific peak temperature interval according to the Fe-Cr-Ni phase diagram. In general, a reduced hardness is observed within the delta ferrite region, the high temperature two-phase region as well as within a narrow region adjacent to the base material. Conversely, the low temperature two-phase region is characterised by a significant hardness increase, whereas the hardness within the austenite region is more comparable with that of the base material.

When welding is performed in the presence of oxygen, a colourful and visible oxide covers the root surface. A closer examination of the oxide, involving the use of sputtered neutral mass spectrometry (SNMS), shows that the HAZ colour bands can be ascribed to constructive interference due to variations in the iron-chromium oxide layer thickness. Conversely, the sharp demarcation line observed towards the base metal is mainly caused by an abrupt change in the oxide composition from a mixed (spinel) type to pure Cr_2O_3.

Both the combined potentiodynamic and potentiostatic corrosion tests and the galvanostatic corrosion tests reveal the existence of a weak iron oxide contaminated zone in the weld HAZ approximately 6mm from the fusion boundary, where the oxide layer is thinnest. The indications are that a spalling mechanism is operative and responsible for the pitting initiation, allowing crevice corrosion to occur beneath the oxide. On the other hand, the observed gradients in the microstructure across the weld HAZ seems to have no significant effect on the pitting corrosion initiation under the prevailing experimental conditions.

In the presence of H_2S, pitting corrosion will also occur in the most oxidised part of the HAZ close to the fusion boundary. These pits are generally deeper and more pronounced than those observed 6mm from the fusion boundary.

2.5 REFERENCES

1. J. Enerhaug, P. E. Kvaale, M. Bjordal, J. M. Drugli, T. Rogne: *Corrosion/99*, paper no. 587, (Houston, TX: NACE International, 1999).
2. S. Olsen, L. Børvik, G. Rørvik, *Corrosion/00*, paper no. 129, (Houston, TX: NACE International, 2000).
3. K. Kondo, K. Ogawa, H. Amaya, H. Hirata, M. Ueda, H. Takabe, Y. Miyzaki: *SUPERMARTENSITIC STAINLESS STEELS '99*, Brussels, Belgium, 1999, Belgian Welding Institute, Belgium, pp. 11-18.
4. H.-J. Niederau: *Stahl u. Eisen*, 1978, vol. 98, pp. 385-392.
5. N. N. Dias, F. G. Wilson, *SOLIFIDICATION TECHNOLOGY IN THE FOUNDRY AND CAST HOUSE*, Book 273, (Metals Society, Coventry, England), pp. 602-606.
6. M. Kimura, Y. Miyata, T. Toyooka, Y. Kitahaba: *Corrosion/00*, paper no. 137, (Houston, TX: NACE International, 2000).
7. T. G. Gooch, P. Woollin, A. G. Haynes: *SUPERMARTENSITIC STAINLESS STEELS '99*, Brussels, Belgium, 1999, Belgian Welding Institute, Belgium, pp. 188-195.
8. J. Vagn Hansen, E. Maahn, P. Aastrup, P. F. Larsen, *Beskyttelsesgasdækning og korrosionsbestandighed efter svejsning af rustfrie stålrør*. Report 87.66, Korrosjonssentralen ATV, Denmark, 1987.
9. M. Bonis, J.-L. Crolet: *Corrosion/94*, paper no. 7, (Houston, TX: NACE International, 1994).
10. J. Enerhaug, S. L. Eliassen, P. E. Kvaale: *Corrosion/97*, paper no. 60, (Houston, TX: NACE International, 1997).
11. S. Olsen, P. E. Kvaale, J. Enerhaug: *SUPERMARTENSITIC STAINLESS STEELS '99*, Brussels, Belgium, 1999, Belgian Welding Institute, Belgium, pp. 84-87.
12. G. Rørvik, L. Børvik, B. Bøgner, E. Aune: *SSC-Testing of Supermartensitic 13% Cr MIG, TIG and Radial Friction Weldments at Åsgard Conditions*. Report Statoil MAT 2000060, Trondheim, 2000.
13. J. S. Colligon, H. Kheyrandish, J. M. Wallis, J. Wolstenholme, *Thin Solid Films*, 1991, vol. 200, pp. 293-300.
14. H. E. Bishop, S. J. Greenwood, *Surface and Interface Analysis*, 1991, vol. 17, pp. 325-329.
15. E. Folkard: *Welding Metallurgy of Stainless Steels*. Springer-Verlag, 1988.
16. F. W. Sears, M. W. Zemansky, H. D. Young: *University Physics*, 7th edn., Addison-Wesley Publishing Company, 1987, pp. 922-925.
17. *CRC Handbook of Chemistry and Physics*, (ed. D. R. Lide *et. al.*), CRC Press 1994, pp. 4.53-4.66.

18. P. Marcus: *Sulfur-Assisted Corrosion Mechanisms and the Role of Alloyed Elements*. ("Corrosion Mechanisms in Theory and Practice", P. Marcus and J. Oudar eds.). Marcus Dekker, 1995, pp. 239-261.
19. P. Hancock, R. C. Hurst: *The mechanical properties and breakdown of surface oxide films at elevated temperatures*. ("Advances in Corrosion Science and Technology", R. W. Staehle and M.G. Fontana eds.), 1974, vol. 4, Plenum Press, pp. 1-84.
20. S. A. Bradford: *Fundamentals of corrosion in gases*. ("Metals Handbook", 9th edn., J. R. Davis *et. al.* eds.), 1987, vol. 13, ASM International, pp. 61-76.

PART III: A COMPARATIVE STUDY OF THE DISSOLUTION AND REPASSIVATION KINETICS OF A 12.3Cr-2.6Mo-6.5Ni SUPER MARTENSITIC STAINLESS STEEL

3.1 INTRODUCTION

Martensitic stainless steel pipes of the 13Cr-4Ni type have successfully been used in the oil industry as OCTG (Oil Country Tubular Goods) material since the nineteen seventies[1]. Later, modified or so-called super martensitic stainless steels (SMSS) with improved weldability and corrosion resistance have been developed. These grades are now in commercial use, also as pipelines[2,3,4,5,6]. Although localised pitting corrosion is observed in most stainless steels, the problem is particularly prominent in SMSS pipes that are employed as flowlines transporting corrosive well stream with H_2S. Since the main emphasis in the past has been on "fit for purpose" testing and qualification of the material for use offshore[6], a more fundamental understanding of the underlying corrosion mechanisms is lacking, as discussed in Part I. Specifically, there is a need to clarify the dissolution and repassivation kinetics of SMSS and compare the results with those reported for other classes of stainless steel under similar experimental conditions[7,8,9,10].

When a stainless steel is exposed to an electrolyte containing aggressive chloride anions, the passive oxide layer is undermined. Chloride ions penetrate the oxide layer at specific points on the surface and increase the rate at which metal dissolves by the reaction $Me \rightarrow Me^{n+} + ne$ [7]. Generally, it is distinguished between the initiation stage, involving the breakdown of the passive film and the development of an aggressive solution, and the growth stage, where stable pit growth occurs when the pitting potential E_P is reached[11,12].

During pitting corrosion the anodic dissolution creates a flow of electrons (current) from the pit surface (anode) to the surrounding passive metal surface (cathode). As metal cations are dissolved in the adjacent electrolyte, chloride anions migrate from the bulk solution towards the pit to maintain electric neutrality in the solution. A hydrolysis reaction of the metal ions lowers the pH, which, together with an increased chloride concentration, prevents repassivation of the pit surface. This behaviour is generally favoured by a low pit surface concentration and a low potential[7]. At a certain threshold in the potential, the rate of dissolution becomes faster than the diffusive transport, which means that the accumulated dissolution products will precipitate, forming a salt layer at the metal-solution interface[7]. The salt layer, in turn, hinders repassivation, and remains intact until the surface concentration of the dissolved species decreases below saturation. Finally, if the concentration exceeds, say, 60% of the saturation level, the active dissolution in salt free surfaces may reach a steady state, provided that the potential is above a certain critical value[7].

It is generally accepted that the growth of a metastable pit is essentially the same as the early growth of a stable pit[11]. Under normal conditions it is believed that only metastable pits, which can maintain a salt film in the absence of a cover, are stable[11]. Accordingly, Laycock and Newman[11] introduced a transition potential E_T to define the intermediate stage between diffusion controlled and activation ohmic growth for a particular limiting current. By this they were able to show that the E_T value approaches the pitting potential E_P at the moment the pits lose their cover.

In the past, the so-called "artificial" pit technique, using lead in pencil electrodes, has been successfully employed to capture the dissolution and repassivation kinetics of certain grades of high alloyed steels[7-11,13-18]. In the present investigation, the potentials of this technique are further explored and documented. In particular, its applicability to SMSS will be demonstrated in which potential step experiments are combined with calculations of the pit surface concentration, using an appropriate diffusion model[7]. By comparing the results with relevant literature data for other classes of stainless steels, the underlying corrosion mechanisms can be disclosed and correlated to the content of Cr, No and Mo in the parent material.

3.2 THEORETICAL BACKGROUND

3.2.1 Numerical pit diffusion model

In the following, a brief outline of the diffusion model will be given.

3.2.1.1 Underlying assumptions and boundary conditions

Since the artificial pit is cylindrical with inert sidewall, its geometry is uniquely defined by the radius r (in mm) and the pit depth δ (in mm), as shown in Figure 3.1. Under such conditions the diffusion problem can be treated as one-dimensional, where the dissolution of the metal surface occurs from the bottom. The pit depth δ is controlled via coulometric readings by calculating the electricity needed to dissolve a specific length of the embedded wire, and can be measured using a light microscope.

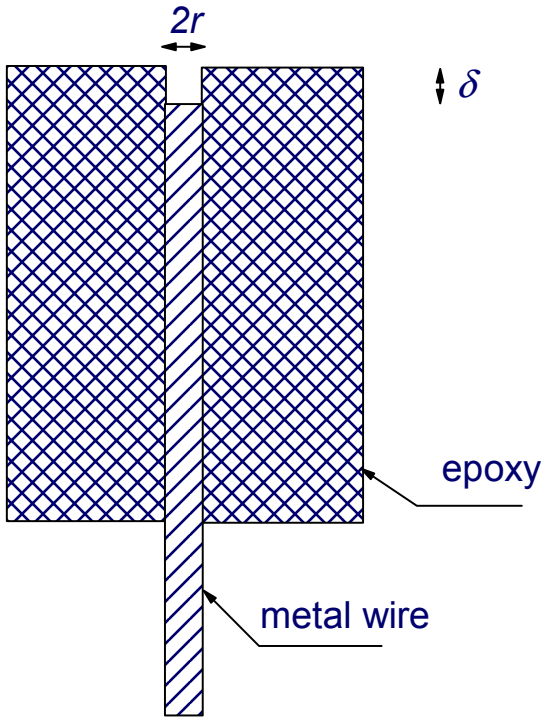

Figure 3.1. Sketch of the artificial pit model (r is the pit radius and δ is the pit depth).

In order to compute the concentration of dissolved species at the pit surface as a function of time, a special PC programme has been developed using the diffusion model of Gaudet *et* al.[7]. However, due to the complexity of the problem a number of simplifications have been made to obtain a tractable model[7,10]. These can be listed as follows:
As a starting point the main alloying elements (Cr, Ni, Mo, Fe) are combined in one hypothetical species Me^{n+}. For the actual SMSS (Fe-12.3Cr-6.5Ni-2.6Mo) the average molecular weight M_w = 56.16g/mol, the average valence n = 2.163 and the average density ρ = 7.90g/cm^3. The relationship between coloumetric reading (q, in C) and pit depth (δ) is then given by Equation (3.1) which applies to a 1 mm dia. SMSS wire:

$$q = \frac{A \cdot \rho \cdot n \cdot F}{M_w} \cdot \delta = 23.07 \cdot \delta \qquad (3.1)$$

where A is the wire cross-sectional area (in cm^2) and F is the Faraday constant (in C/mol).
As a second approximation the solubility of the species Me^{n+} is assumed to be equivalent to that of pure $FeCl_2$. This is because the solubility of the $CrCl_3$

compound is much higher under the prevailing circumstances[10]. The saturation concentration is fixed to $C_{sat} = 4.2M$ throughout the calculations.
Next, the diffusion length is assumed to be equal to the actual pit depth (δ). This assumption is valid as long as the current-pit depth product is constant[7], implying that the flux-dependent hemispherical boundary layer outside the pit is negligible.
Finally, it is assumed that ion migration can be neglected and that the system is adequately described by a variable diffusion coefficient D (in cm^2/s), which allows for the variation in the electrolyte concentration along the pit depth. The appropriate relationship for D is:

$$D = \frac{D_0}{1 + b \cdot C_{Me}} \tag{3.2}$$

where b is the viscosity coefficient (in litre/mol), C_{Me} is the concentration of dissolved species (in mol/litre), and D_0 is the infinite dilution diffusivity (in cm^2/s).

In Gaudets[7] model the changes in the solution concentration during a potential step experiment is described by Fick's 2nd law, which is the continuity equation for diffusion:

$$\frac{\partial C_{Me}}{\partial t} = D \frac{\partial^2 C_{Me}}{\partial x^2} \tag{3.3}$$

where t is time (in seconds) and x is the position (in mm) defined as zero at the pit surface. The calculations are initiated when the current for diffusion-controlled dissolution of the Me^{n+} species is reached, assuming an initial linear concentration profile in the pit, given as:

$$C_{Me}\big|_{t=0} = C_{sat} \cdot \frac{(\delta - x)}{\delta} \tag{3.4}$$

The boundary conditions of the system can be summarised as follows:

$$C_{Me}\big|_{x=\delta} = 0 \text{ and } D_{Me} \left.\frac{\partial C_{Me}}{\partial x}\right|_{x=0} = \frac{I}{nFA} \tag{3.5}$$

where I is the current (in mA).

3.2.1.2 Validation of solution algorithm

Because the current has a transient response, the boundary condition at the pit surface is time dependent. This implies that no simple analytical solution can be found, and the diffusion problem must therefore be solved numerically using the finite volume method in combination with explicit time integration[19]. Based on the assumption that the initial concentration profile in the pit is linear, the surface concentration has been calculated for the imposed current as a function of time. In this way the experimental current-time data can be transformed and replotted as current density versus surface concentration.

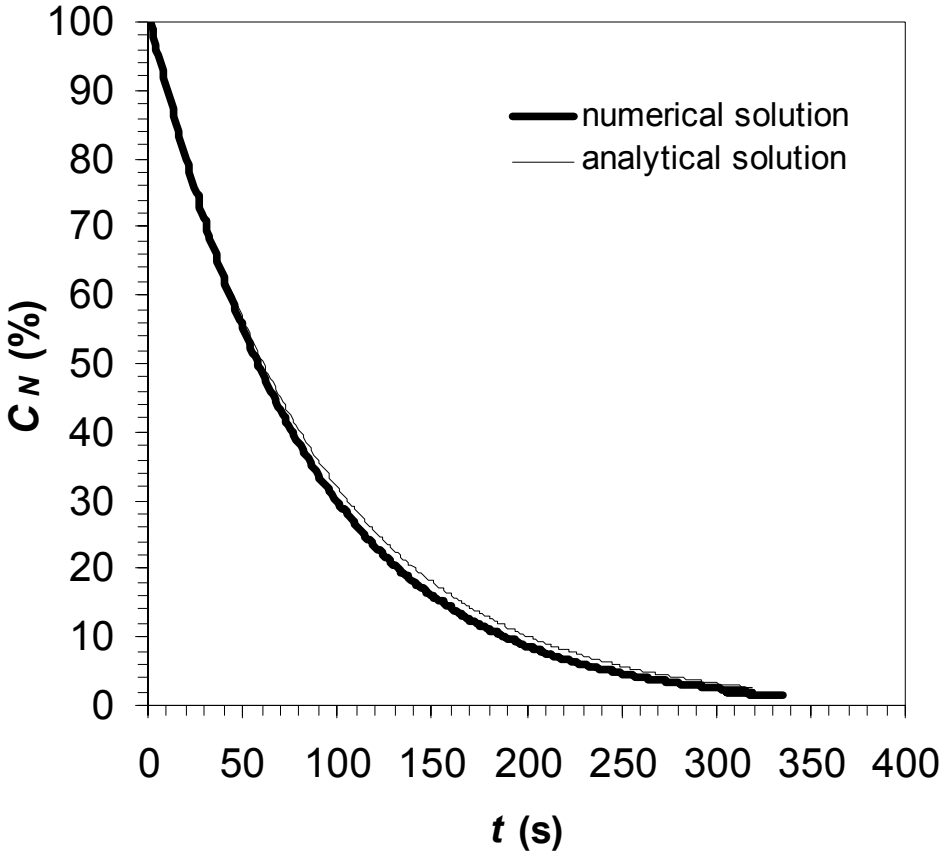

Figure 3.2. Comparison between the outputs from the numerical algorithm and the analytical solution, respectively, showing normalised concentration C_N *vs.* time t for a 0.5mm deep pit.

The numerical algorithm is validated by comparison with an analytical solution, assuming zero flux of dissolving metal ions from the pit surface and a constant diffusivity in the pit. Under such conditions Equation (3.3) has the following analytical solution[20]:

$$C_{Me} = \frac{C_{sat}}{2} \cdot e^{-\frac{\pi^2 Dt}{4\delta^2}} \cos\left(\frac{\pi}{2\delta} x\right) \tag{3.6}$$

The analytical solution assumes a cosine-like starting concentration profile of dissolved species in the pit. Provided that a similar starting concentration profile is implemented in the numerical solution, the resulting concentration transients coincide, as shown in Figure 3.2. The graph shows the normalised concentration transients C_N at the pit surface, as predicted by the numerical solution and the analytical solution for a 0.5mm deep pit, assuming zero flux and $b = 0$ in the numerical solution. As the two solutions coincide, the numerical algorithm is correctly implemented and validated.

3.2.1.3 Assumed starting concentration profile

In the final calculations, however, a linear starting concentration profile is assumed, as done by Gaudet *et* al.[7] and Steinsmo and Isaacs[10]. This, in turn, makes it possible to compare results from different tests to decide whether the dissolution and repassivation behaviour of SMSS is similar to that reported for other grades of high-alloyed steels.

3.2.2 Solution resistance

In general, a comparison of current decay curves or single data points measured at unequal pit depths requires an adequate IR-correction and consequently an expression for the solution resistance as a function of pit depth. The solution resistance R_s (in ohm) in an artificial pit is given as[7]:

$$R_s = R_p + R_b = \alpha_1 \left(\frac{\delta}{\pi r^2}\right) + \alpha_2 \frac{1}{4r} \tag{3.7}$$

where α_1 and α_2 are the average solution resistivities within and outside the pit, respectively. The first term R_p expresses the solution resistance in the pit, increasing linearly with the pit depth. The second term represents the approach resistance in the mouth of the pit, and is therefore only a function of the pit radius r.

The R_s-values can be determined using potential step experiments. The applied potential E (in mV) consists of the sum of the potential at the pit surface and the *IR*-drop in the pit solution, and can be expressed as:

$$E = b_a \log\left(\frac{I}{A}\right) + k + I \cdot R_S \tag{3.8}$$

where b_a is the Tafel slope (in mV/decade) and k is a constant. A differentiation and subsequent reformulation of Equation (3.8) gives:

$$R_S = \frac{dE}{dI} - \frac{b_a}{\ln 10 \cdot I} \tag{3.9}$$

In practice, it is a reasonable approximation to assume that $\frac{dE}{dI} >> \frac{b_a}{\ln 10 \cdot I}$, which leads to:

$$R_s \approx \frac{\Delta E}{\Delta I} \tag{3.10}$$

Hence, the R_s values can be determined from the slope of the *E-I* curves, as obtained from the potential step experiments, using linear regression. Alternatively, a.c. impedance measurements can be used to determine the R_s-values[9], as done in the present investigation to validate Equation (3.7).

3.3 EXPERIMENTAL PROCEDURES

3.3.1 Materials and specimen preparation

The material to be tested was received in the form of a cold-drawn SMSS Ø1mm Thermanite 13/06 welding wire (produced by Böhler Thyssen) with a martensitic microstructure and a chemical composition as shown in Table 3.1 (Fe-12.3Cr-6.5Ni-2.6Mo). The wire was slightly ground with a 1000-grit paper before it was cleaned with acetone and embedded in a rod of epoxy, as shown in Figure 3.3. Prior to the corrosion tests the end face of the rod was ground with a 1000-grit paper and washed in acetone.

Table 3.1. Chemical composition of the base material (in wt%).

C	Cr	Mo	Ni	S	Si	Mn	V	Cu
0.02	12.3	2.6	6.5	0.003	0.50	0.69	0.03	0.04

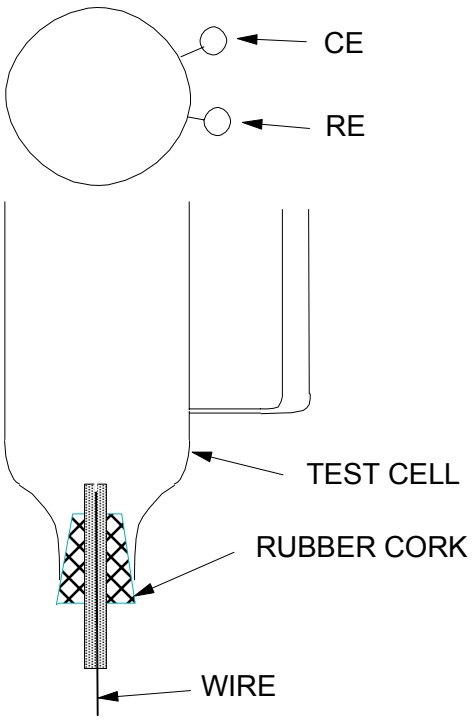

Figure 3.3. Schematic illustration of the artificial pit test set up.

3.3.2 Test setup

The rod was mounted in a 200ml-glass cell, with the ground end facing upwards, see Figure 3.3. A saturated calomel electrode (SCE) was used as a reference electrode, while a platinum wire served as counter electrode. The electrolyte was 1*M* NaCl (air-saturated) at 22 ± 2°C. A Solatron SI 1286 unit, controlled by the PC programme Galvanostat, was used to carry out the potentiostatic measurements, while a Solatron SI 1280 unit was used in the case of the a.c. impedance measurements.

3.3.3 Potential step measurements

The wire surface of the stainless steel was first polarised to a potential E of 400mV SCE to activate the corrosion process and grow pits with certain depths. During the growth process the dissolved products will diffuse towards the pit opening and create a concentration gradient in the pit. If the current density i (in mA/cm^2) is sufficiently high the solution concentration exceeds the super saturation level and a thin salt film will start to precipitate on the metal

surface[7]. Under such conditions, the current density will reach its limiting value i_{lim} (in mA/cm^2), which is determined by the extent of diffusion occurring within the pit itself [10]. Hence, a further increase in the potential (i.e. beyond 400mV SCE) will not lead to a corresponding increase in the current density.

3.3.3.1 Solution resistance (IR-drop)

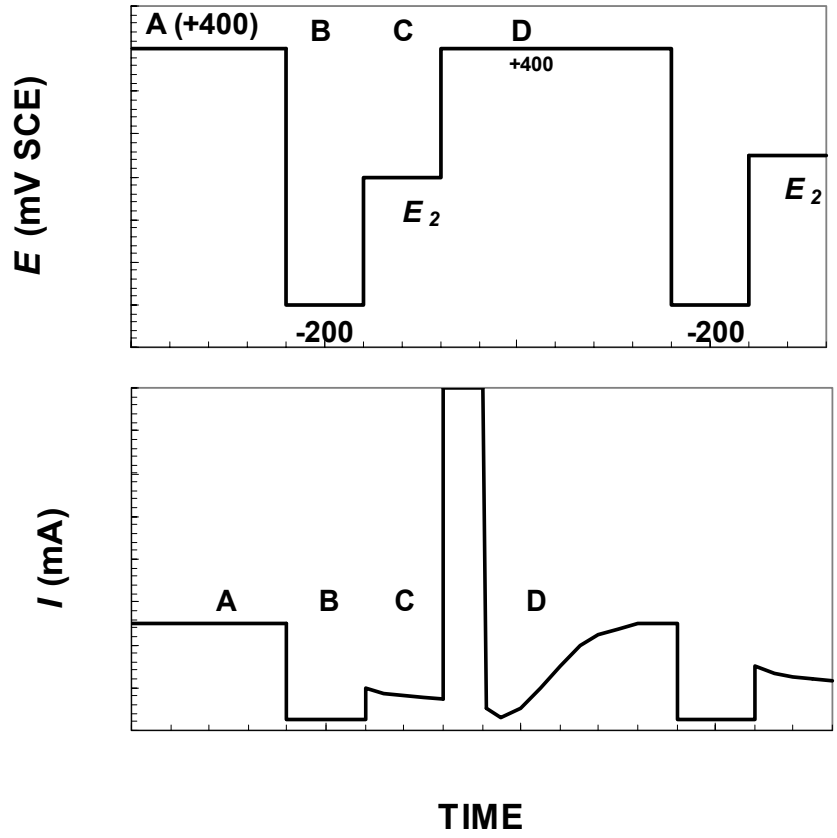

Figure 3.4. Graphical representations of the potential changes (top) and the current variations (bottom) during polarisation measurements of the solution resistance.

Referring to Figure 3.4, the R_s-values are measured as follows. Initially, the potential is kept at E = 400mV SCE (labelled A in Figure 3.4) until the desired pit depth is reached. Subsequently, E is shifted to a lower value (B, −200 mV SCE) for a few seconds to promote full dissolution of the salt film. The potential is then shifted to E_2 (C), where the maximum current (I_{max}, in mA) at super saturation is measured in the absence of a salt film on the metal surface. Before the next measurement the pit surface is reset by shifting E back to 400mV SCE (D) to restore the salt film and the diffusion-controlled state. The procedure is repeated varying E_2 from 100 to 600mV SCE in steps of 100mV. By utilizing the recorded (E_2, I_{max}) data couples, the R_s value can be determined by means of

linear regression. The measurements are repeated for several pit depths, and curve fitting of the final (R_s, δ) data allows the R_s-δ relationship to be established, according to Equation (3.7).

In a second set of experiments a.c. impedance measurements (20kHz to 1kHz) were used to determine the R_s values, employing 10mV amplitude of modulated potential and 10ohm measuring resistor. Prior to each a.c. measurement, the salt film was dissolved and the current density re-adjusted to the diffusion-controlled value. These independent R_s data provide a basis for validating the potential step measurements and Equation (3.10).

3.3.3.2 Polarisation curves

As a part of the experimental programme, polarisation curves were measured at several pit depths to establish a common overvoltage curve for a constant and close to saturation concentration of dissolved products present at the metal surface. Referring to Figure 3.5, the polarisation curves are measured as follows. Initially, the potential is kept at E = 400mV SCE (labelled A in Figure 3.5) until the desired pit depth is reached. Subsequently, E is shifted to a lower value (B, –200 mV SCE) for a few seconds to promote full dissolution of the salt film.

The potential E is then increased, tuned in and maintained for approximately 30s at a level where the current equals the initial diffusion controlled value at 400mV SCE (C). This is the same value being reached as in the potential step measurements with a salt layer present on the metal surface, ensuring that the concentration at the metal surface is close to saturation. Next, the potential is shifted to E_2 (D) where the current is measured before it is shifted to and kept at the diffusion controlled value for approximately 30 seconds. Note that the procedure is repeated varying E_2 between –200 and 200mV SCE in steps of 50mV and that all reported polarisation curves have been subjected to IR-corrections. Finally, the joint overvoltage curve is constructed via the measured polarisation curves using the correct Tafel slope (b_a).

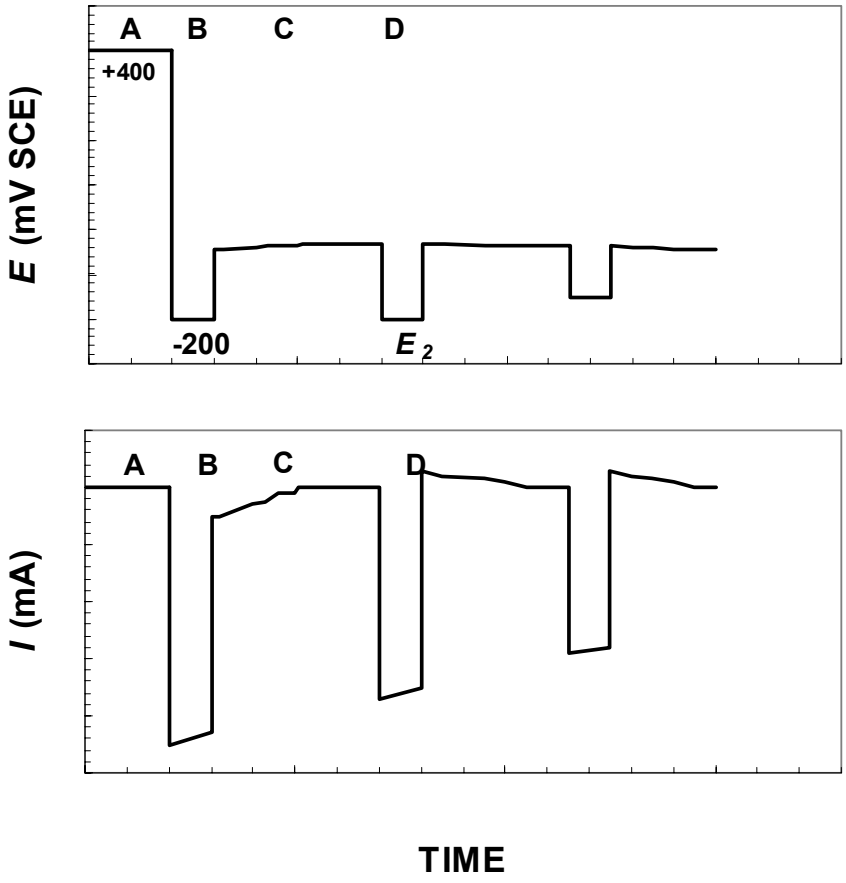

Figure 3.5. Graphical representations of the potential changes (top) and the current variations (bottom) during polarisation measurements of the overvoltage curve.

3.3.3.3 Repassivation behaviour

In addition, potential step experiments have been carried out at different pit depths and at different applied potentials to derive current decay curves for varying concentrations of corrosion products present at the metal surface. Referring to Figure 3.6, the measurements are carried out as follows. Initially, the potential is kept at E = 400mV SCE (labelled A in Figure 3.6) until the desired pit depth is reached. Subsequently, E is shifted to a lower value (B, –200 mV SCE) for a few seconds to promote full dissolution of the salt film. The potential is then increased, tuned in and kept for approximately 30s at the level where the current equals the initial diffusion controlled value at 400mV SCE (C). Finally, the applied potential is shifted to and kept at E_2 (D) until repassivation eventually occurs.

As the last step, the pit surface concentration transients have been calculated and iso-potential maps constructed, using the IR-corrected current density values i_2 (in mA/cm^2) as the ordinate and the normalised surface concentration of dissolved species (C_N) as the abscissa. The IR-correction is done according to Equation (3.11):

$$i_2 = i \cdot 10^{\frac{iAR_S}{b_a}} \qquad (3.11)$$

This equation assumes a constant value for the Tafel slope, which means that possible effects of varying metal surface conditions on the measured current densities are ignored.

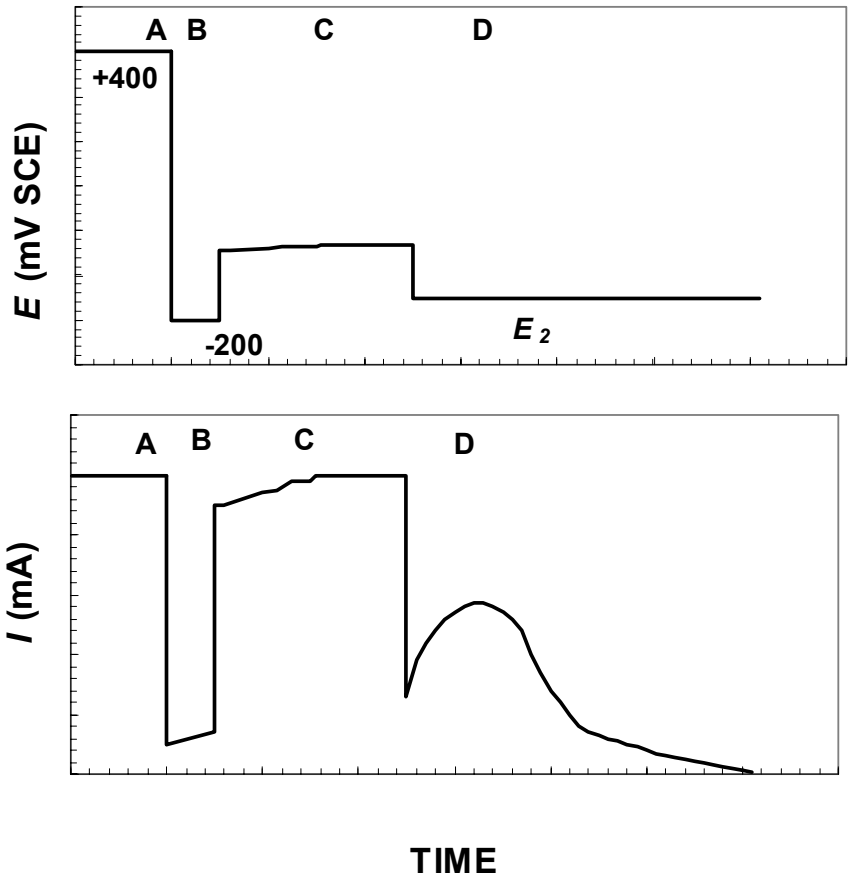

Figure 3.6. Graphical representations of the potential changes (top) and the current variations (bottom) during polarisation measurements of the repassivation transients.

3.4 RESULTS

3.4.1 Validation of the diffusion length

By plotting the diffusion-controlled current density (i_{lim}) *vs.* the inverse of the pit depth ($1/\delta$) it is possible to determine whether the actual pit depth (δ) is representative of the diffusion length[7]. As judged from the linear part of the curve in Figure 3.7, this appears to be a reasonable approximation for pit depths greater than 0.4mm.

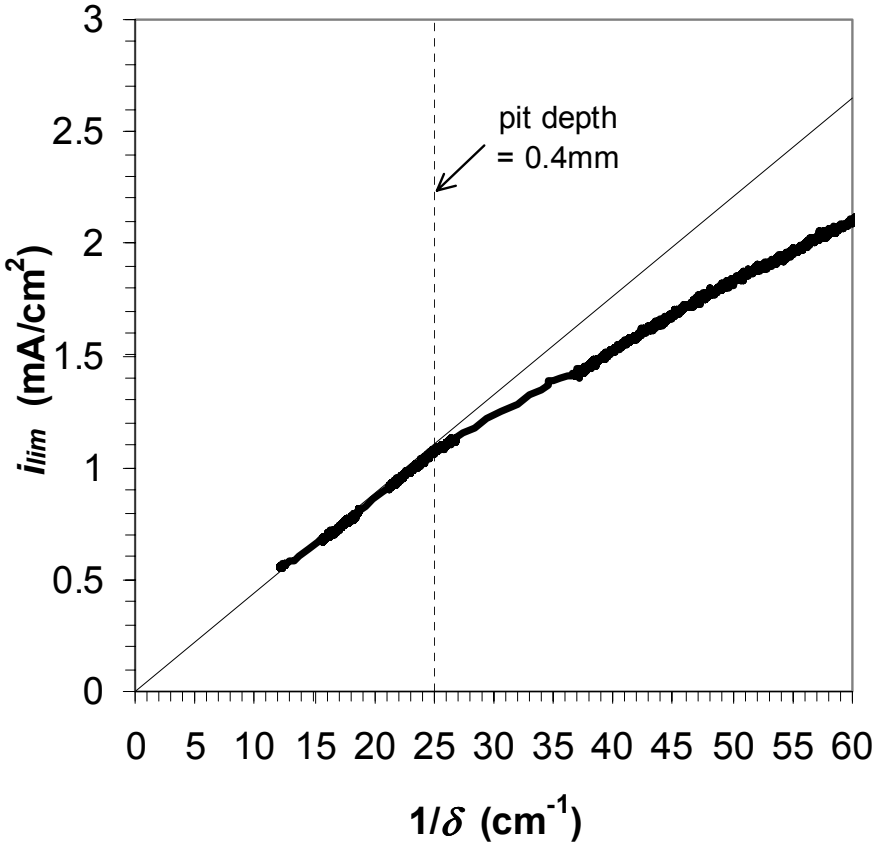

Figure 3.7. Plot of the measured diffusion-limited current density i_{lim} vs. inverse pit depth $1/\delta$ during artificial pit growth.

3.4.2 Solution resistance

The solution resistance is determined as described in the experimental procedure. The total amount of electric current passing through the system during one set of experiments was less than 0.3C. This corresponds to less than 0.015mm increase in the pit depth, and makes it possible to correlate the solution resistance to the average pit depth.

The results are shown graphically in Figure 3.8. Included in this plot are both data obtained from the potential step experiments and the independent a.c. measurements. It follows that both sets of data are well described by a common trend-line, which mathematically can be expressed as:

$$R_s = 155.9 \cdot \delta + 66 \text{ (in } \Omega) \qquad (3.12)$$

The degree of conformity achieved shows that the assumptions made in deriving Equation (3.10) are physically reasonable under the prevailing circumstances and that the present potential step measurements provide an accurate description of the solution resistance in the pit.

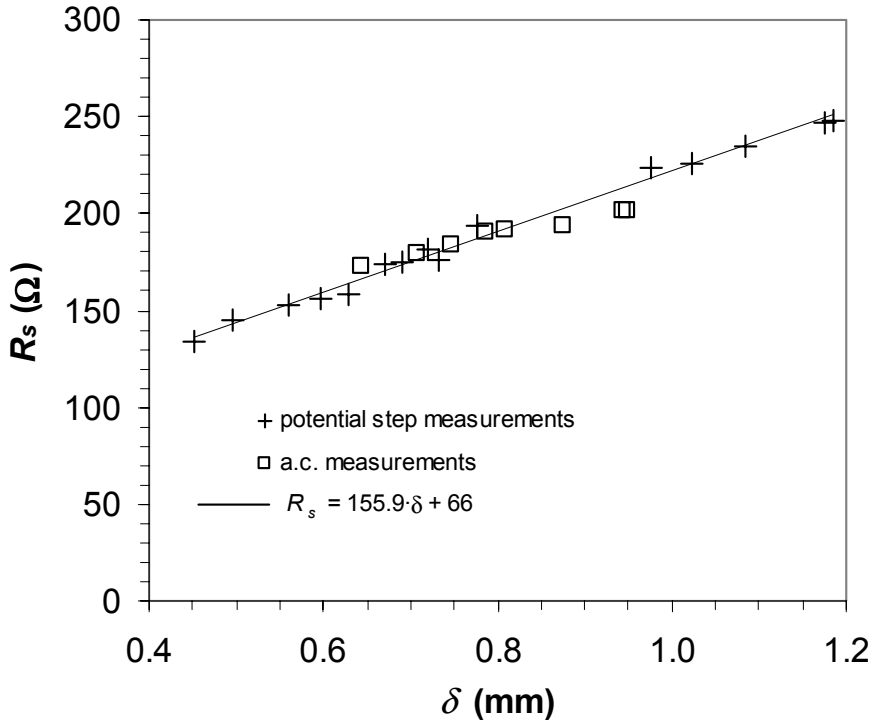

Figure 3.8. Experimental validation of Equation 3.10, based on potential step measurements and independent a.c. impedance measurements, respectively.

3.4.3 Overvoltage curve

The polarisation curves are measured as described in the experimental procedure. They refer to five pit depths in the range from 0.48 to 0.74mm. In all cases the concentration at the solution/metal interface is close to the saturation level. The potentials were IR-corrected and the curves are plotted in a log *i vs. E* diagram, as shown in Figure 3.9. It can be seen from the figure that the different

polarisation curves tend to overlap. A simple regression analysis yields the following Tafel equation:

$$E = 57 \log i - 281 \text{ (in mV SCE)} \qquad (3.13)$$

Equation (3.13) shows that the potential is independent of the pit depth and only a function of the current density as long as a salt film is not present at the metal surface.

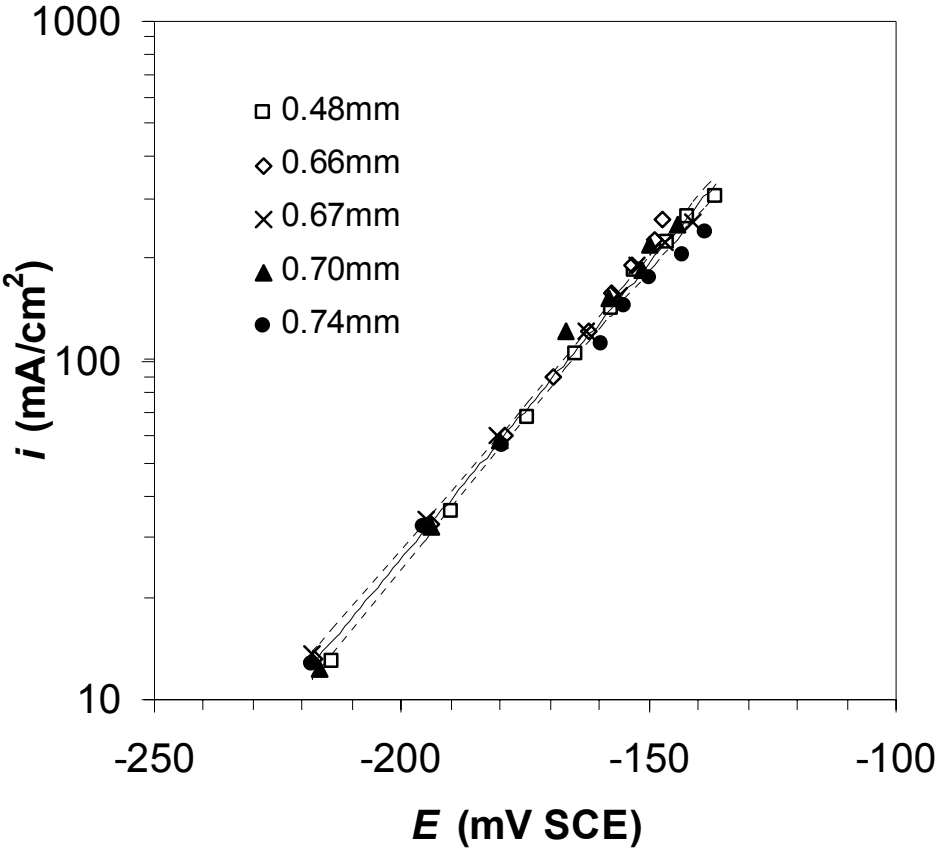

Figure 3.9. Summary of IR-corrected polarisation curves obtained at various pit depths (i.e. 0.48, 0.66, 0.67, 0.70 and 0.74mm, respectively). The solid line represents the mean overvoltage curve, while the dashed lines represent the 99% confidence intervals.

3.4.4 Repassivation

The experiments are carried out according to the experimental procedure. Repassivation measurements were carried out at varying potentials (i.e. –200, –175 and –150mV SCE) for a range of pit depths. Typical raw data curves at –200mV SCE are reproduced in Figure 3.10. The current transients progress as expected, reflecting the symbiotic relationship between the repassivation

behaviour and the surface concentration of the dissolved species. Initially, the current passes through a local maximum before the passive current is reached. At larger pit depths the maximum value is lower owing to the increased IR-drop. At the same time, the time to repassivation increases due to an enhanced diffusion path, which slows down the reduction in the concentration of dissolved species on the metal surface.

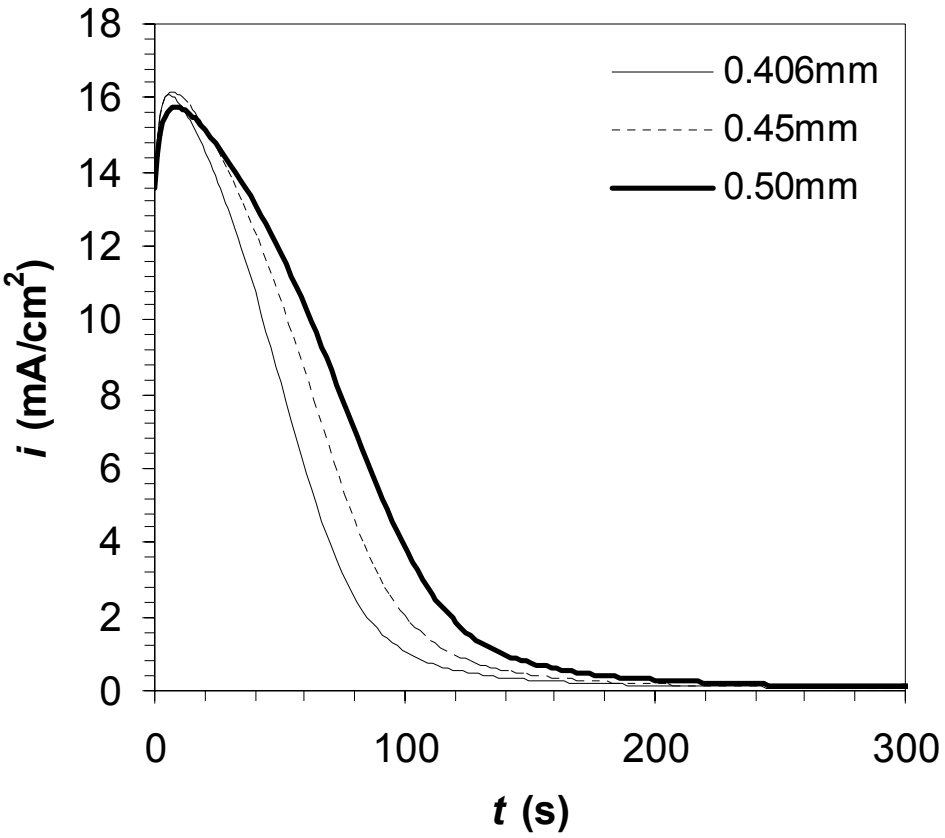

Figure 3.10. Examples of measured repassivation transients for three different pit depths.

Normalised transients of the surface concentration of the dissolved species have been calculated using the numerical diffusion model and the following input data, taken from Steinsmo and Isaacs[10]: C_{sat} = 4.2mol/litre, b = 0.69litre/mol and $D_0 = 1.16 \cdot 10^{-5}$cm^2/s. The value of D_0 has been reduced by approximately 8.5% to account for the pertinent difference in the solution temperature between the two investigations (i.e. 25°C vs. 22°C as used in the present case), according to normal practice[21]. On this basis, average repassivation *vs.* normalised concentration curves have been constructed, as shown in Figure 3.11, with error bars representing the 95% confidence intervals. It follows that all curves yield the characteristic sigmoid form, where the scatter in the experimental data is seen to diminish with decreasing potentials. Within the applied potential range

full passivation of the SMSS is achieved, as evidenced by the observed upper plateaus in the current density.

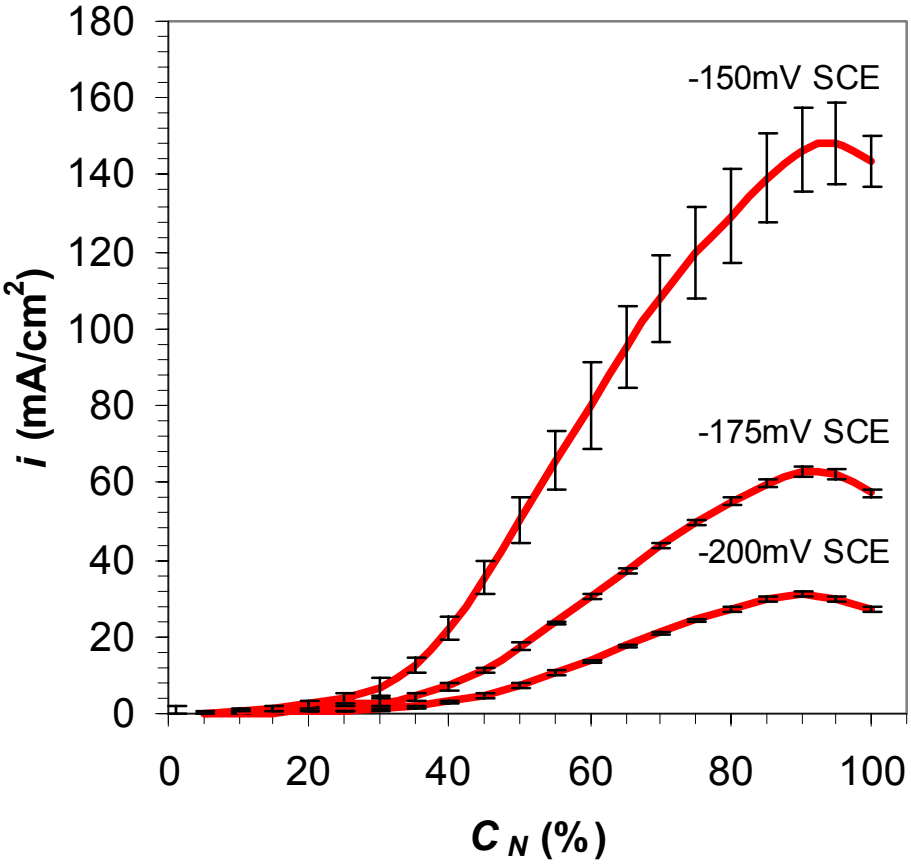

Figure 3.11. Plots showing averaged current density i *vs.* normalised concentration C_N for three different potentials (i.e. –200, –175 and –150mV SCE, respectively). The error bars represent the 95% confidence intervals.

3.5 DISCUSSION

3.5.1 IR-drop measurements

Equation (3.7) suggests that a linear relationship exist between the solution resistance and the pith depth, which, in turn, is the basis for applying the IR-corrections of the potentials. If the assumption holds, the measured R_s-values should yield a linear dependence of the pit depth, in agreement with the experimental observations in Figure 3.8. Hence, the correction procedure adopted in the present investigation is fully acceptable in view of the extent of experimental evidence being available.

Based on the measured R_s-curve in Figure 3.8, the coefficients α_1 and α_2 in Equation (3.7) are found to be 122 and 132Ωmm, respectively. Gaudet *et* al.[7] also applied potential step measurements in their investigation of a 304 stainless steel (1*M* NaCl, 25°C), and estimated α_1 and α_2 to 138 and 104Ωmm, respectively (reduced by 8.5% to account for the pertinent difference in the solution temperature), which agrees well with the present results. A different approach was taken by Laycock and Newman[11], who used an average resistivity of 50Ωmm for the concentrated pit solution at 25°C. Extrapolating back to 22°C, the values of α_1 and α_2 would be 54.3 and 150.8Ωmm, respectively for a 1*M* NaCl solution. These values depart significantly from those reported by Gaudet *et* al.[7] and confirmed by the present authors. Laycock and Newman[11] discussed this discrepancy and suggested that the resistance values obtained in earlier studies (which are similar to the those obtained in this investigation) was overestimated. Alternatively, the discrepancy reflects differences in the experimental conditions. A possible source of overestimation could be the omission of the charge transfer resistance term in Equation (3.10). The following equation represents an attempt, based on Equation (3.9), to quantify this uncertainty:

$$\varepsilon = \frac{\left(\frac{dE}{dI} - \left(\frac{dE}{dI} - \frac{b_a}{\ln 10 \cdot I}\right)\right)}{\frac{dE}{dI}} \cdot 100(\%) = \frac{b_a}{\ln 10 \cdot I} \cdot \frac{100}{\frac{dE}{dI}}(\%) \qquad (3.14)$$

By utilizing measured values of I and dE/dI and assuming b_a = 57mV/dec, the average value of ε, representing the relative overestimation of R_s, is found to be about 6%, which is far too low to account for the discrepancy mentioned above.

The relevance of Equation (3.12) is further documented by the independent a.c. impedance measurements, showing an overall good agreement between the two sets of data (see Figure 3.8). Finally, it has been demonstrated that the IR-corrections based on Equation (3.12), provide the best linear fit of the overvoltage curve in Figure 3.9 and similar curves reported by others (not shown here)[7,10,11]. Accordingly, the method adapted in the present investigation, involving the use of R_s-measurements, offers a convenient and accurate way of adjusting the applied potentials.

3.5.2 Dissolution kinetics

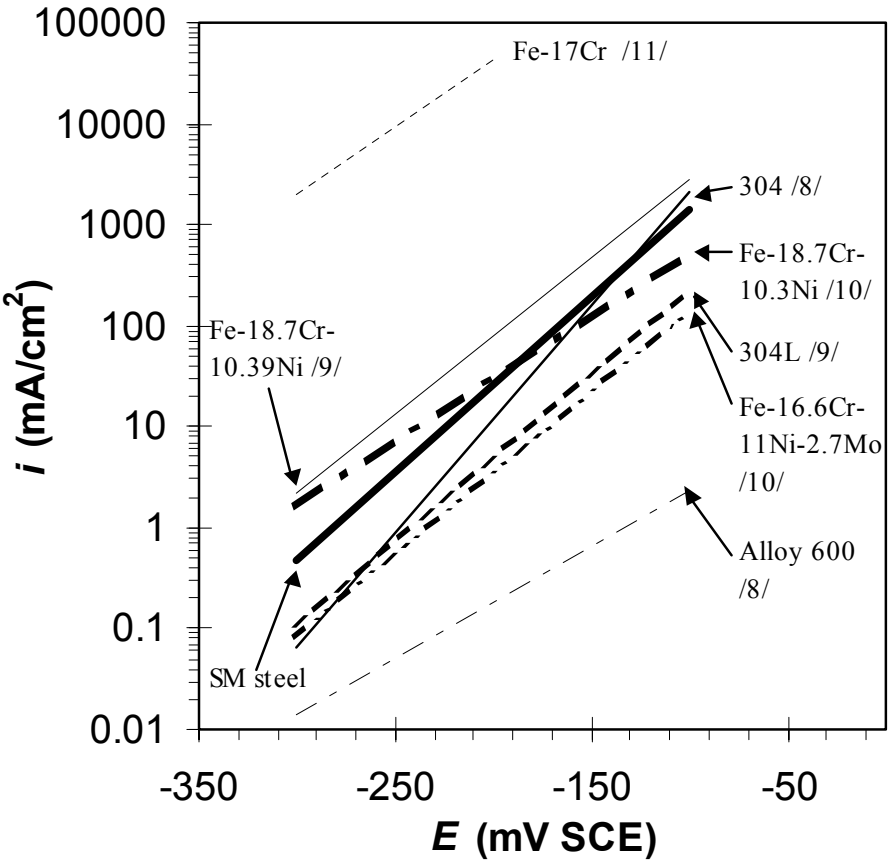

Figure 3.12. Summary of overvoltage curves for different grades of high alloyed steels. The curves are constructed on the basis of relevant literature data[7,8,9,10]. The thick solid line is the corresponding overvoltage curve for the SMSS shown in Figure 3.9.

The artificial pit technique has previously been used to characterise the active dissolution kinetics of different grades of high alloyed steels, including 304[7], 304L[8], 600[7], Fe-17Cr[10], Fe-18.7Cr-10.4Ni[8], Fe-18.7Cr-10.3Ni[9] and Fe-16.6Cr-11Ni-2.7Mo[9]. Most of these alloys were tested in a 1*M* NaCl solution at 25°C, except for the two last ones that were tested in a 1*M* KCl solution at 22°C. Overvoltage curves for the actual alloys are replotted in Figure 3.12. They are

constructed on the basis of the original curves, but are stretched to cover a wider potential range to make a direct comparison possible.

3.5.3 Repasivation kinetics

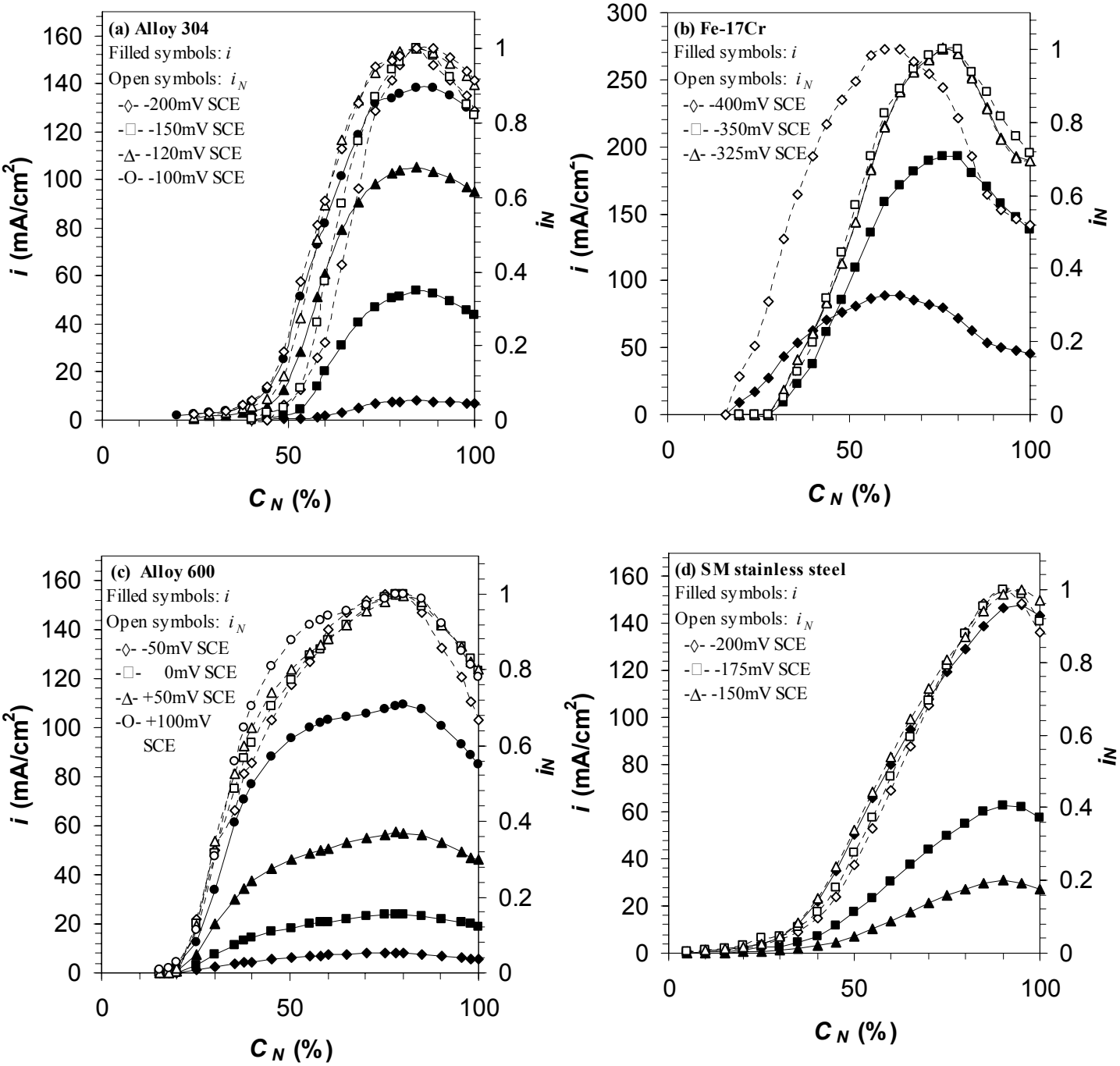

Figure 3.13. Plots showing the current density *i vs.* normalised concentration C_N for different grades of high alloyed steels; (a) Alloy 304[7], (b) Fe-17Cr[10], (c) Alloy 600[7], and (d) SMSS (present study). Curves marked by open symbols show the normalised current densities i_N.

In addition, the artificial pit technique has been used to characterise the repassivation kinetics of different grades of high alloyed steels, including 304[7], 600[7] and Fe-17Cr[10]. The alloys were all tested in a 1*M* NaCl solution at 25°C, and the characteristic *i vs.* C_N repassivation transients obtained in these tests are replotted in Figures 3.13 (a), (b) and (c), respectively. The corresponding data for the SMSS are included in Figure 3.13 (d). To enable a fair comparison of the different transient curves the right ordinate shows the normalised current density i_N, where the data have been normalised with respect to the peak current density and replotted on a scale from 0 to 1. A closer inspection of Figure 3.13 (a) – (d) reveals that the repassivation behaviour of the SMSS is similar to that observed for the other steel grades. An exception is the Fe-17Cr alloy at –400mV SCE.

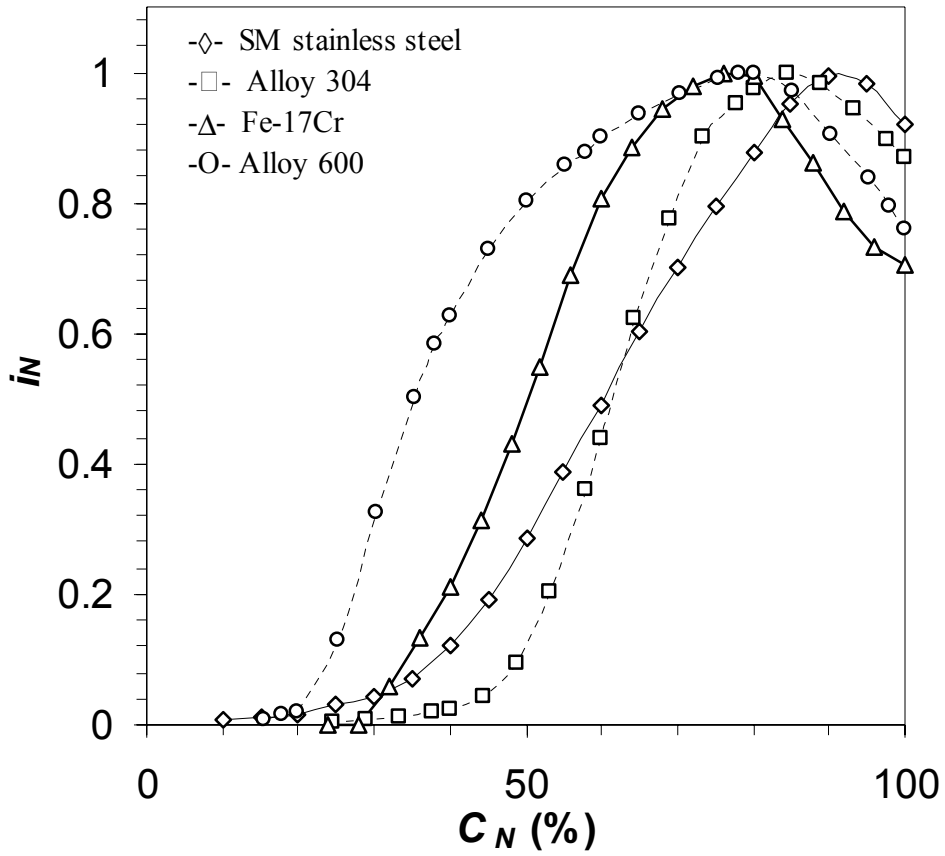

Figure 3.14. Plots showing the averaged normalised current density i_N *vs.* normalised concentration C_N, using input data from Figures 3.13 (a) – (d).

Moreover, it appears from Figure 3.13 that the different curves tend to overlap when they are plotted in a normalised fashion. This point is better illustrated in Figure 3.14, which shows a collection of the individual repassivation transients, with exception of the Fe-17Cr alloy at –400mV SCE. It follows that the repassivation behaviour of the SMSS falls between that observed for the 304

alloy and the Fe-17Cr steel, which is consistent with its intermediate content of Mo and Ni. On the other hand the repassivation of the nickel based 600 alloy follows a different pattern. For nickel based alloys, the active dissolution rates are much lower, even at high potentials, as can be seen from Figure 3.13 (c). Similarly, they passivate at relatively low surface concentrations of dissolved species (< 20% for the 600 alloy) due to the fact that nucleation and growth of a protective chromium oxide is slower in nickel based alloys as compared to iron based alloys[22].

3.6 CONCLUSIONS

The dissolution and repassivation kinetics of a SMSS exposed to a 1*M* NaCl solution at 22°C has been characterised using the so-called "artificial pit" technique. The basic conclusions that can be drawn from the investigation can be summarised as follows:

The active dissolution behaviour of an artificial SMSS pit can be described by a simple Tafel type of approach. For concentrations close to the saturation level, the Tafel slope and the current density is found to be approximately 57mV/dec and 0.5mA/cm^2 at –300mV SCE, respectively.

A comparison with relevant literature data shows that the active dissolution behaviour of the SMSS is consistent with that observed for other high-alloyed steel grades. Hence, the SMSS exhibits a slower dissolution rate than Fe-17Cr, Fe-18.7Cr-10.4Ni and Fe-18.7Cr-10.3Ni, in spite its lower chromium content. This is most likely a result of the higher molybdenum content in the SMSS. The dissolution rate is, on the other hand, faster than that reported for the high-alloyed Fe-16.6Cr-11Ni-2.7Mo steel grade because of a leaner alloying content.

Active pits in the SMSS will normally repassivate as the concentration of dissolved species at the pit surface decreases below about 30% of the saturation level. The repassivation behaviour of the SMSS is found to be reasonable and consistent with that reported for other high-alloyed steel grades.

To summarise, the observed response of SMSS to localised corrosion is deemed to be in accordance with its content of Cr, Ni and Mo. The comparison between different steel grades has therefore disclosed no anomalies that cannot readily be accounted for by compositional effects.

3.7 REFERENCES

1. M. Bonis, J.-L. Crolet: *Corrosion/94*, paper no. 7, (Houston, TX: NACE International, 1994).
2. K. Tamaki: *Corrosion/89*, paper no. 469, (Houston, TX: NACE International, 1989).
3. Miyasaka. H. Ogawa: *Corrosion/90*, paper no. 67, (Houston, TX: NACE International, 1990).
4. S. Hashizume, T. Takaoka, Y. Minami, Y. Ishizawa, T. Yamada: *Corrosion/91*, paper no. 28, (Houston, TX: NACE International, 1991).
5. M. Ueda, T. Kushida, T. Mori: *Corrosion/95*, paper no. 80, (Houston, TX: NACE International, 1995).
6. J. Enerhaug, S. L. Eliassen, P. E. Kvaale: *Corrosion/97*, paper no. 60, (Houston, TX: NACE International, 1997).
7. G. T. Gaudet, W. T. Mo, T. A. Hatton, J. W. Tester, J. Tilly, H. S. Isaacs, R. C. Newman, *AIChE J.*, 1986, vol. 32, pp. 949-958.
8. R. C. Newman, H. S. Isaacs, in *Passivity of Metals and Semi-Conductors*, Proceedings of the 5th International Symposium in Passivity, Elsevier, Amsterdam, 1983, pp.269-274.
9. R. C. Newman, *Corr. Sci.*, 1985, vol. 25, pp. 341-.
10. U. Steinsmo, H. S. Isaacs, *J. Electrochem. Soc.*, 1993, vol. 140, pp. 643-653.
11. N. J. Laycock, R. C. Newman, *Corros. Sci.*, 1997, vol. 39, pp. 1791-1809.
12. Z. Szklarska-Smialowska, *Pitting Corrosion of of Metals*, NACE, 1986.
13. H. S. Isaacs, *J. Electrochem. Soc.*, 1973, vol. 120, pp. 1456-1462.
14. J. W. Tester, H. S. Isaacs, *J. Electrochem. Soc.*, 1975, vol. 122, pp. 1438-1445.
15. H. S. Isaacs, R.C. Newman, in *Corrosion and Corrosion Protection*, R. P. Frankenthal and F. Mansfeld. Editors, Proceedings vol. 81-8, The Electrochemical Society Softbound Proceedings Series, Pennington, NJ, (1983), pp. 120-130.
16. H. S. Isaacs, R. C. Newman, in *Corrosion Chemistry within Pits, Crevices and Cracks*, A. Thurnbull, Editor, HMSO Publ., London, 1987, pp. 45-59.
17. H. S. Isaacs, *Corros. Sci.*, 1989, vol. 29, pp. 313-323.
18. R. C. Newman, E. M. Franz, *Corrosion*, 1984, vol. 40, pp. 325-330.
19. S. U. Patankar: *Numerical Heat Transfer and Fluid Flow* (3rd ed.), McGraw-Hill, 1986.
20. M. D. Greenberg: *Foundation of applied mathematics*, Prentice-Hall, 1978.
21. D. R. Lide (ed): *Handbook of Chemistry and Physics*, CRC Press (1994).
22. L. L. Shreir, R. A. Jarman, G.T. Burstein: *Corrosion vol. 1* (3rd ed.), Butterworth Heinemann, 1994, §4.5.

APPENDIX 3.1. NOMENCLATURE

A wire cross-sectional area, cm^2
b viscosity coefficient, litre/mol
b_a anodic Tafel slope, mV/decade
C_{Me} surface concentration of dissolved species, mol/litre
C_N normalised surface concentration of dissolved species
C_{sat} saturated metal ion concentration, mol/litre
D diffusivity, cm^2/s
D_0 infinite dilution diffusivity, cm^2/s
E potential, mV SCE
E_{pit} critical pitting potential, mV SCE
E_T transition potential between instable and stable pit growth, mV SCE
F Faraday constant, 96 485 C/mol
i current density, mA/cm^2
i_2 IR-corrected current density, mA/cm^2
i_{lim} diffusion-controlled current density, mA/cm^2
i_N normalised current density
k constant
I current, mA
I_{max} maximum current, mA
M_w average molecular weight, g/mol
n average metal valence, equivalent/mol
q total electricity, C
R_b bulk solution resistance, Ω
R_s total resistance, Ω
R_p pit solution resistance, Ω
r wire radius, mm
t time, s
x pit length, coordinate, mm
α solution resisitivity, Ωmm
ε error in estimated solution resistance by neglecting the charge transfer resistance, %
δ pit depth, mm

PART IV: A STUDY OF THE EFFECT OF H_2S ON DISSOLUTION AND REPASSIVATION KINETICS OF A 12.3Cr-2.6Mo-6.5Ni SUPER MARTENSITIC STAINLESS STEEL

4.1 INTRODUCTION

The so-called super martensitic stainless steels (SMSS) with improved weldability and corrosion resistance are becoming industrially important. These grades are now in commercial use, also as pipelines transporting corrosive well stream containing CO_2 and traces of H_2S[1,2]. Typical design values for such pipelines are 30 000 - 100 000ppm Cl^-, 90-140°C (maximum), 2 - 40mbar H_2S, 1 - 20bar CO_2 and *pH* 4.5 – 5.5.

Although localized pitting corrosion is a potential problem for most stainless steels in H_2S-containing environments, the problem is particularly prominent in SMSS pipelines inasmuch as they are among the lowest alloyed stainless grades. Pipe producers, test houses and end-users have published corrosion test results of SMSS parent material and weldments[3,4,5,6,7,8]. There have, however, been a great scatter in the test results[9], and it has been difficult to determine the specific effects of *pH*, temperature, H_2S and of chloride. A possible reason for the scatter may stem from the till now disregarded effect of root surface condition and the role of H_2S on occurrence and growth of localized corrosion in SMSS weldments, referring to the results obtained in Part II and Part V of the present thesis. In fact, the root surface of SMSS weldments are found to be vulnerable to localized corrosion in the as-welded condition at ambient temperatures in the presence of H_2S[1]. These surfaces are probably not fully passive as a result of high temperature oxidation of the root surface occurring during welding. The main effects of H_2S are probably to may be to hinder repassivation in the most oxidized area close to the fusion boundary and to accelerate anodic dissolution, referring to Part V and Part VI. The dissolution and repassivation kinetics of the SMSS are consistent with that observed for other high-alloyed grades. This was demonstrated in the comparative study in Part III, where a Fe-12.3Cr-6.5Ni-2.6Mo steel were characterized in a 1*M* NaCl solution at ambient temperature using the "artificial pit technique". The comparison between different steel grades disclosed no anomalies that cannot readily be accounted for by compositional effects.

The next step is to examine the effect of H_2S and CO_2 on dissolution and repassivation kinetics of SMSS pits. The "artificial pit technique" was successfully employed in Part III to capture the properties of the SMSS alloy in the absence of H_2S/CO_2. The same test methodology is therefore adopted also in the present study. By comparing these results with the results obtained in Part III and with relevant literature data for other classes of stainless steels, the underlying corrosion mechanisms can be disclosed and correlated to reported effects of H_2S/CO_2.

4.2 THEORETICAL BACKGROUND ON THE IMPACT OF H_2S ON CORROSION

This study is concerned with dissolution and repassivation kinetics in a pit of a SMSS alloy exposed to a corrosive well stream water phase at ambient temperature. It appears to be a fair simplification to keep the CO_2 level constant and only vary the H_2S concentration in the course of this study, since CO_2 not influences pitting corrosion in CRA's apart from its impact on the *pH* value in the bulk solution[10,11]. The pitting potential in CRA's is more or less unaffected by the partial pressure of CO2. E.g., in a study on super duplex stainless steel at 200°C, Miyaki *et* al[12] found a constant pitting potential in the range of 0 to 30bar CO_2. In fact, Rogne *et* al.[13,14] showed that traces of oxygen (i.e. 50ppb) were sufficient to overrule the effect of 2 bar CO_2 as regards pitting in duplex and 254 SMO stainless steels. Sulfur compounds are, on the other hand, surface active species[15] and are reported to influence the pitting properties of stainless steels[16,17,18].

The effects of H_2S and other sulphur compounds on corrosion of metals and alloys are generally ascribed to the influence of specifically adsorbed sulfur atoms (denoted S_{ads}) on the alloy surface[17]. S_{ads} promote pitting corrosion as follows: Firstly, S_{ads} may stabilize otherwise unstable (or metastable) pits, whereby the critical pitting potential is reduced. Secondly, S_{ads} may preclude and hinder repassivation by sustaining active dissolution at conditions where the pit otherwise would repassivate. Thirdly, S_{ads} may accelerate anodic dissolution due to the catalytic nature of the accelerating effect of S_{ads}.

Atomic sulphur adsorbed on metal surfaces is thermodynamically stable[17], also under conditions where the metal sulphides not are stable, and can be adsorbed according to:

$$H_2S + H_2O_{ads}(M) \rightarrow S_{ads}(M) + 2H^+ + 2e \qquad (4.1)$$

and desorbed according to:

$$S_{ads}(M) + 5H_2O(l) \leftrightarrow HSO_4^- + O_{ads}(M) + 9H^+ + 8e \qquad (4.2)$$

where M denotes metal. A schematic *E vs. pH* diagram is shown in Figure 4.1, where the bold lines represent the stability domains for adsorbed species on pure Fe[19] according to Equations (4.1) and (4.2), and define the potential area for S-

induced dissolution. The corresponding stability domains for Cr[20] and Ni[21] differs somewhat from Fe, but it is assumed that the properties of active surfaces of the SMSS alloy containing about 78%Fe is best represented by the Fe stability diagram.

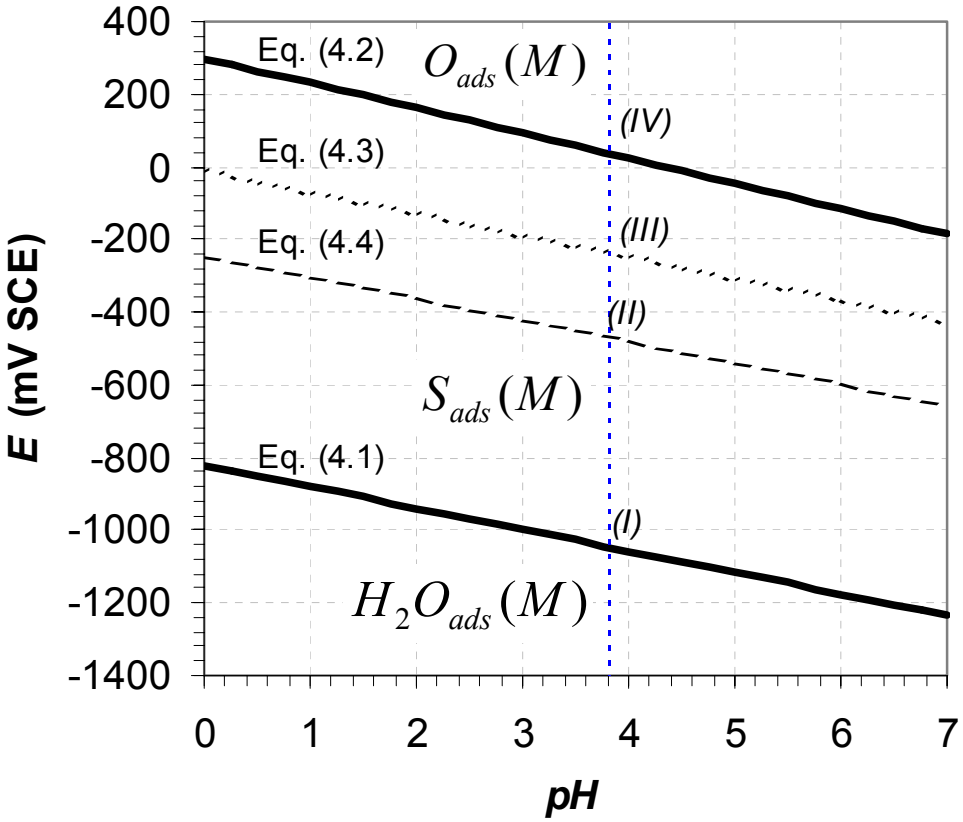

Figure 4.1. Simplified re-plot of a stability diagram for adsorbed species on pure Fe (i.e. denoted M). The data are taken from Ref. [19].

The stability domains for S_{ads} imply a potential dependency where the effect of H_2S should vanish at potentials above line (IV) and below line (I) in Figure 4.1. This has, in fact, been observed in studies of CRA's in the presence of sulphur compounds. Newman[22] examined a Fe-19Cr-10Ni alloy in thiosulphate solutions (i.e. *pH* 7.3, 0.25*M* Na_2SO_4 and 0.025*M* $Na_2S_2O_3$) and found that corrosion attacks only repassivated above –250mV SCE. The effect of thiosulphate was ascribed to specifically adsorbed sulphur. Consequently, the observed potential dependency was explained in terms of the stability potential of S_{ads} (i.e. Equation (4.2)). Other studies have, on the other hand, shown that oxidation of H_2S at the alloy surface may result in depletion of H_2S, whereby the H_2S effect ceases even within the stability domins of S_{ads}. This was experienced by Mat and Newman[18] in a study of alloy 316L in 0.6*M* NaCl and 0.03*M* H_2S at 80°C. A sharp decrease of the anodic current density was observed at −130mV SCE during a potentiodynamic scan. They ascribed that phenomenon not to the

stability of S_{ads}, but actually to depletion of H_2S due to its oxidation on the passive surface, thus no longer being available to activate the pits. Oxidation of H_2S to bulk sulphur occurs according to:

$$H_2S(aq) \rightarrow 2H^+ + S(s) + 2e^- \quad (4.3)$$

and its redox potential is included in Figure 4.1. Comparing the stability lines for Equation (4.2) and Equation (4.3) indicate oxidation of and hence depletion of H_2S within the stability domain of S_{ads}. Note that the redox potential for water reduction:

$$H_2O + 2e \leftrightarrow H_2(g) + 2OH^- \quad (4.4)$$

is also included in Figure 4.1.

It follows from Figure 4.1 that S_{ads} are replenishing adsorbed water molecules at (I). Thermodynamically, S_{ads} is stable until (IV), where oxygen atoms replenish the S_{ads} atoms, whereby S-induced dissolution is believed to cease. However, as a fraction of S_{ads} atoms normally are removed together with dissolving metal ions[17], will an insufficient replenishment of these promote repassivation below (IV). Re-adsorption of S_{ads} presupposes a certain H_2S level at the metal surface, whilst adsorption of S_{ads} as well as H_2S oxidation (i.e. Equation (4.4)) reduces the H_2S level at the surface and creates an H_2S gradient towards the surface. Oxidation of H_2S above (III) similar to that observed by Mat and Newman[18] may therefore promote repassivation of the SMSS alloy beneath (IV).

4.3 EXPERIMENTAL PROCEDURES

4.3.1 Materials and specimen preparation

The material to be tested was received in the form of a cold-drawn SMSS Ø1mm Thermanite 13/06 welding wire (produced by Böhler Thyssen) with a martensitic microstructure and a chemical composition as shown in Table 4.1. The wire was slightly ground with a 1000-grit paper before it was cleaned with acetone and embedded in rods of epoxy, as shown in Figure 4.2. Prior to any corrosion test the end face of the rod was ground with a 1000-grit paper and washed with acetone.

Table 4.1. Chemical composition of the base material (in wt%).

C	Cr	Mo	Ni	S	Si	Mn	V	Cu
0.02	12.3	2.6	6.5	0.003	0.50	0.69	0.03	0.04

4.3.2 Test setup

The rod was mounted in a 200ml-glass cell, with the ground end facing upwards, as shown in Figure 4.3. A saturated calomel electrode (SCE) was used as a reference electrode, while a platinum wire served as counter electrode. The electrolyte was 1*M* NaCl at 22 ± 2°C. Prior to any measurements the solution was purged with nitrogen to remove any oxygen, followed by purging with CO_2, and finally purging with the actual H_2S/CO_2 gas mixture for the rest of the test. A Solatron SI 1286 unit, controlled by the PC programme Galvanostat, was used to carry out the electrochemical measurements.

4.3.3 Test solution

A gas mixture of H_2S and CO_2 is purged through a deaerated 1*M* NaCl solution at ambient temperature and pressure. The bulk electrolyte is adequately described by the chemical composition in Table 4.2 in terms of *pH* and concentrations of H_2S, HS^- etc., calculated by means of MultiScale[23]. The bulk concentrations of H_2S in the solutions purged with gas mixtures of 10 and 40mbar H_2S (i.e. balanced with CO_2) are calculated to about 1m*M* and to about 4m*M*, respectively. The dominating sulphur is H_2S, whilst similar CO_2 concentrations provide *pH* values of about 3.8.

Table 4.2. Calculated bulk concentrations of dissolved species.

	10mbar H_2S/ 0.99 bar CO_2	40mbar H_2S/ 0.96 bar CO_2
CO_2 (bar)	0.99	0.96
pH	3.8	3.8
H_2S (m*M*)	0.95	3.8
HS^- (m*M*)	10^{-4}	0.004
S^{2-} (m*M*) [1]	$3 \cdot 10^{-17}$	$1.2 \cdot 10^{-16}$
CO_2 (m*M*)	28.1	29
H_2CO_3 (m*M*)[1]	0.079	0.076
HCO_3^- (m*M*)	0.17	0.17
CO_3^{2-} (m*M*)	$2.7 \cdot 10^{-7}$	$2.6 \cdot 10^{-7}$
NaCl (*M*)	1	1

[1] From the Kjeller Sweet Corrosion model.

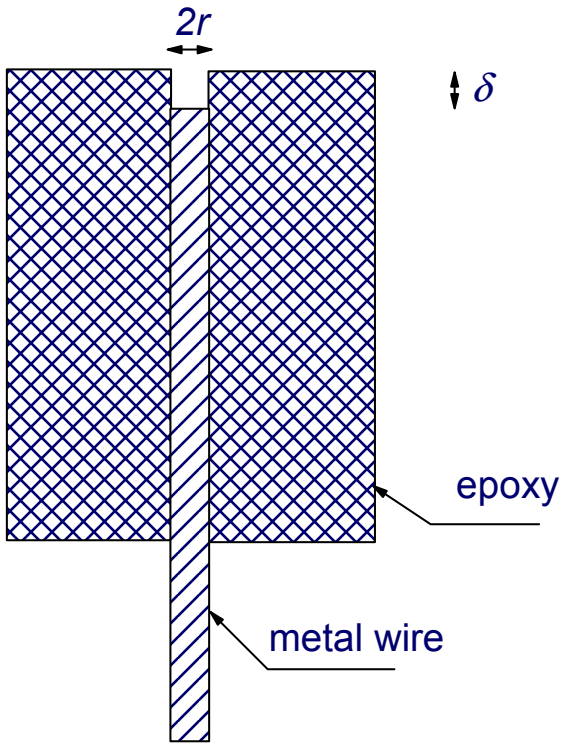

Figure 4.2. Sketch of the artificial pit model (r is the pit radius and δ is the pit depth).

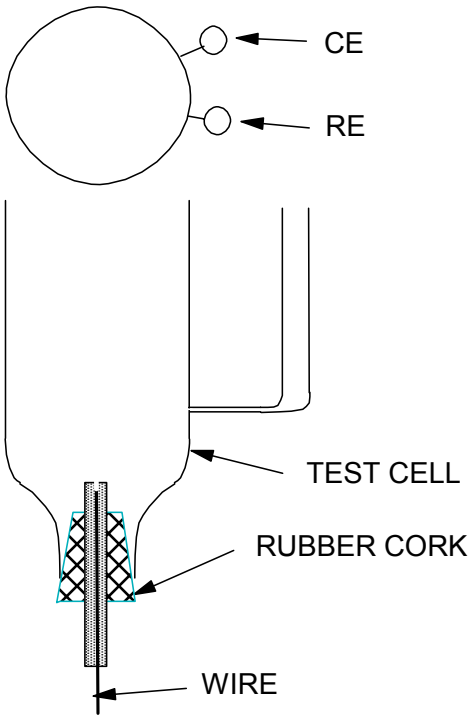

Figure 4.3. Schematic illustration of the artificial pit test set up.

4.3.4 Electrochemical measurements

During the measurements, the value of the pit depth δ (in mm), is controlled by means of the following expression:

$$\delta = \frac{QM_{Me}}{n_{Me}F\rho_{Me}} \tag{4.5}$$

where M_w is the average molecular weight (in g/mol), n_{Me} is the average metal valence (equivalent/mol), F is Faraday's number (in C/mol) and ρ_{Me} is the average density (in g/cm^3). Moreover, the accumulated charge Q (in C) is calculated by integrating the current I (in mA) vs. time t (in s) curve as:

$$Q = \int I \cdot dt \tag{4.6}$$

As regards the actual alloy M_{Me} was estimated to 56.16g/mole, n_{Me} to 2.163 and ρ_{Me} to 7.9g/cm^3. As a rule of thumb Q = 23.07C correspond to δ = 1mm. The wire surface of the stainless steel is first polarised to an applied potential E of 400mV SCE to generate a general break down of the passivity and to subsequently grow pits with certain depths. The dissolved products diffuse towards the pit opening and create a concentration gradient in the pit. At high current densities the solution concentration exceeds supersaturation and a thin salt film precipitates on the metal surface[7]. The current then becomes diffusion controlled, and any further rise in the potential does not increase the current, even though it declines slowly with time as the pit grows deeper[7,10].

4.3.4.1 Solution resistance

In general, a comparison of current decay curves or single data points measured at unequal pit depths requires an adequate IR-correction and consequently an expression for the solution resistance as a function of pit depth. The solution resistance R_s (in ohm) in an artificial pit is given as[7]:

$$R_s = R_p + R_b = \alpha_1\left(\frac{\delta}{\pi r^2}\right) + \alpha_2\frac{1}{4r} \tag{4.7}$$

where α_1 and α_2 are the average solution resistivities within and outside the pit, respectively. The first term (R_p) expresses the solution resistance in the pit, increasing linearly with the pit depth. The second term is the approach resistance in the mouth of the pit, and is therefore only a function of the pit radius r.

In Part III, an expression for R_s *vs.* δ for the actual SMSS artificial pit in a 1*M* NaCl solution was established using potential step experiments and confirmed by a.c. impedance experiments, given as:

$$R_s = 155.9 \cdot \delta + 66 \text{ (in } \Omega) \qquad (4.8)$$

which has been adopted for the IR-corrections in the present study.

4.3.4.1 Polarisation curves

As a part of the experimental programme, polarisation curves were measured at several pit depths to establish a common overvoltage curve for a constant and close to saturation concentration of dissolved products present at the metal surface. Referring to Figure 4.4, the polarisation curves are measured as follows. Initially, the potential *E* is kept at 400mV SCE (labelled A in Figure 4.4) until the desired pit depth is reached. Subsequently, *E* is shifted to a lower value (B, –200 mV SCE) for a few seconds to promote full dissolution of the salt film. *E* is then increased, tuned in and maintained for approximately 30s at a level where the current equals the initial diffusion controlled value at 400mV SCE (C). This is the same value being reached as in the potential step measurements with a salt layer present on the metal surface, ensuring that the concentration at the metal surface is close to saturation. Next, *E* is shifted to E_2 (D) where the current is measured before it is shifted to and kept at the diffusion-controlled value for approximately 30s. Note that the procedure is repeated varying E_2 between –200 and 200mV SCE in steps of 50mV and that all reported polarisation curves have been subjected to IR-corrections. Finally, the joint overvoltage curve is constructed via the measured polarisation curves using the correct Tafel slope (b_a).

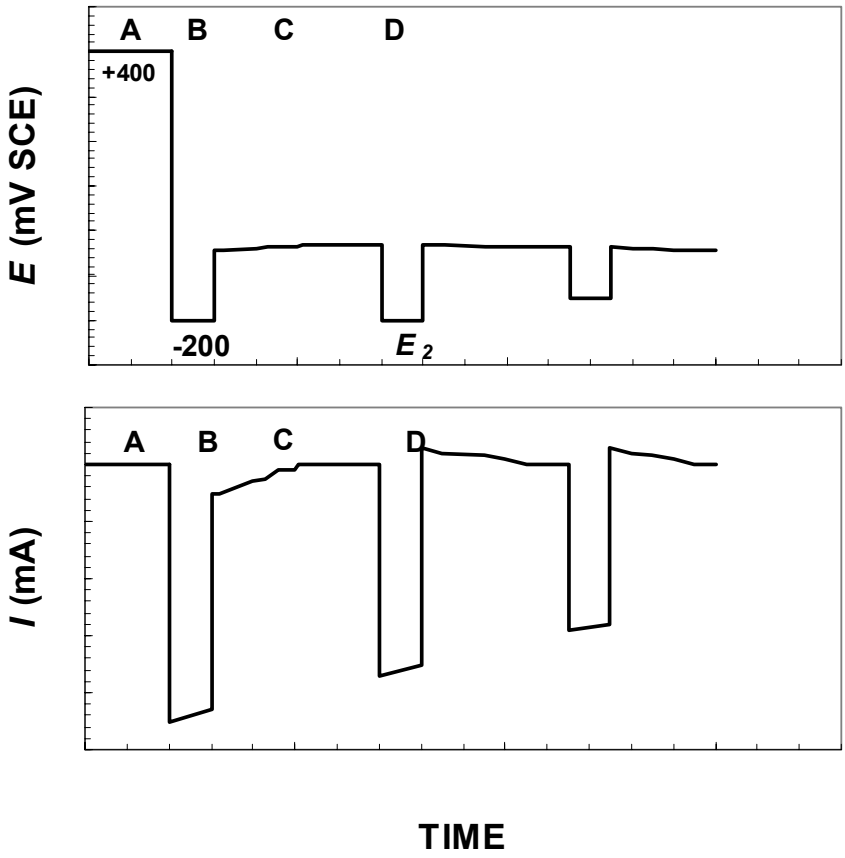

Figure 4.4. Graphical representations of the potential changes (top) and the current variations (bottom) during polarisation measurements of the overvoltage curve.

4.3.4.2 Repassivation behaviour

In addition, potential step experiments have been carried out at different pit depths and at different applied potentials to derive current decay curves for varying concentrations of corrosion products present at the metal surface. Referring to Figure 4.5, the measurements are carried out as follows. Initially, E is kept at 400mV SCE (labelled A in Figure 4.5) until the desired pit depth is reached. Subsequently, E is shifted to a lower value (B, −200 mV SCE) for a few seconds to promote full dissolution of the salt film. The potential is then increased, tuned in and kept for approximately 30s at the level where the current equals the initial diffusion controlled value at 400mV SCE (C). Finally, the potential is shifted to and kept at E_2 (D) until repassivation eventually occurs.

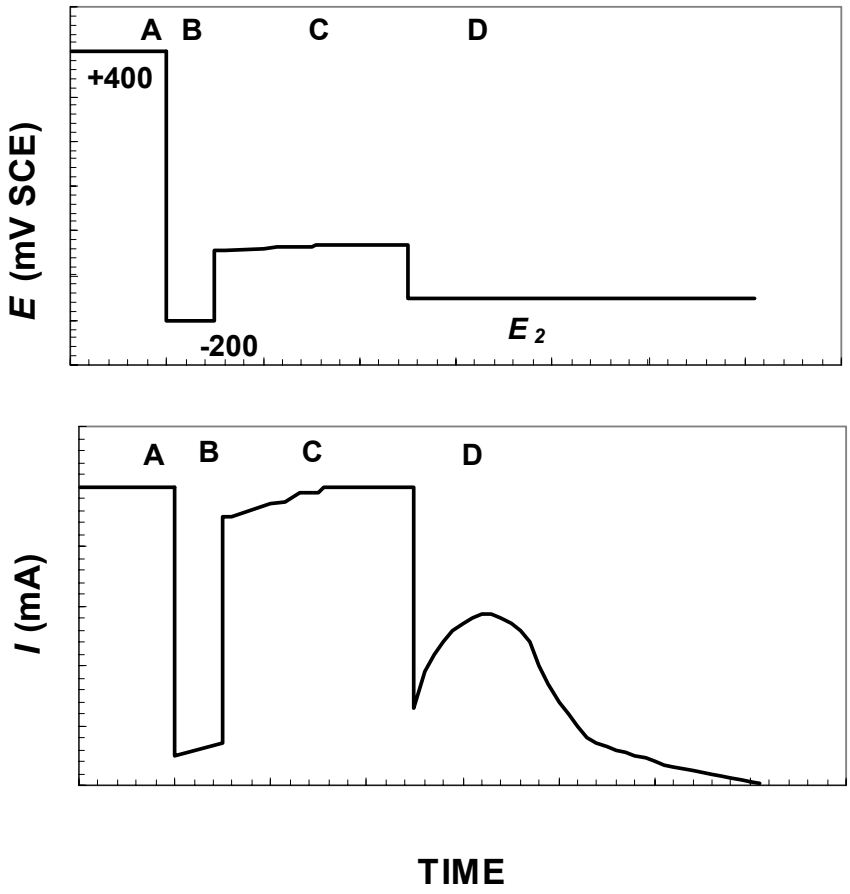

Figure 4.5. Graphical representations of the potential changes (top) and the current variations (bottom) during polarisation measurements of the repassivation transients.

4.3.5 Pit diffusion calculations

The diffusion processes in the pit during potential step experiments are calculated by means of a numerical algorithm (i.e. a PC-programme) that was developed in Part III, based on the diffusion model described by Gaudet *et* al.[7] with basis in Fick's 2nd law. The output from the calculation is the concentration of dissolved species at the pit surface as a function of time.

4.4 RESULTS AND DISCUSSION

The concentration of CO_2 and hence the bulk *pH* is approximately the same in the two electrolytes that are applied in the corrosion tests. Therefore only variations in the H_2S concentration are considered in the present evaluation. First, possible effects of H_2S on the initial pit growth are evaluated. After that, the results from the various tests are presented and discussed, starting with the tests where the test methodologies from previous studies[7] were applied.

4.4.1 Pit growth characteristics

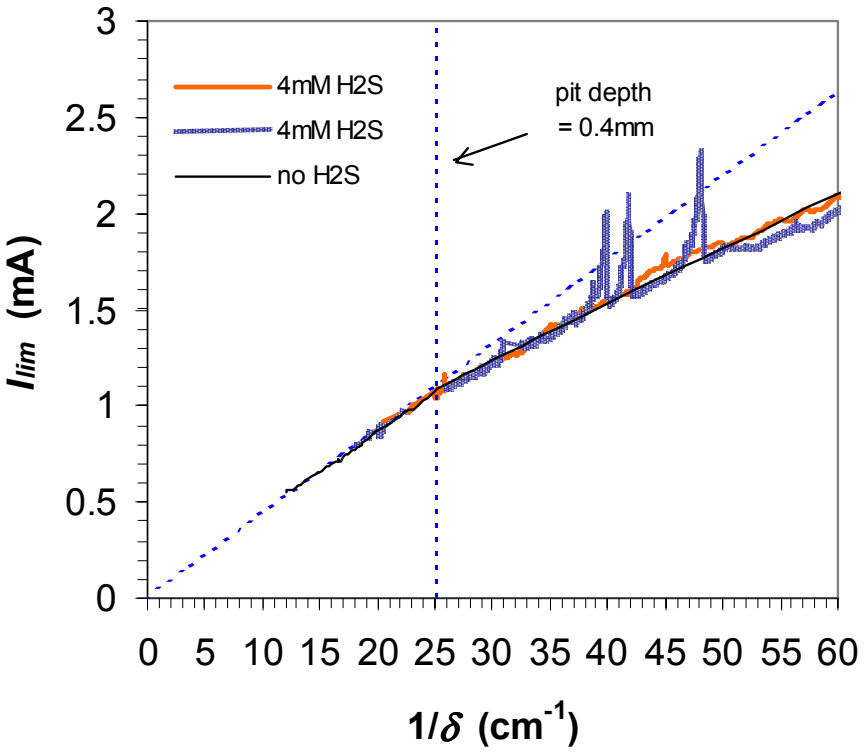

Figure 4.6. Plot of the measured diffusion-limited current I_{lim} vs. inverse pit depth $1/\delta$ during artificial pit growth.

Pit growth curves recorded in the 4m*M* H_2S solution are plotted in the *I vs.* $1/\delta$ diagram shown in Figure 4.6. A corresponding curve recorded in the absence of H_2S in Part III is included in the diagram to enable a fair comparison. Generally, after a short period involving the breakdown of the passive film and a subsequent activation of the surface, a salt film precipitate on the surface whereby the current becomes diffusion-controlled and the adjacent pit solution

reaches its saturation concentration of dissolved species. The curves overlap independent of any H_2S/CO_2 as the pits grow beyond 0.1mm (i.e. below $25cm^{-1}$), which therefore disclose any influence of CO_2 or H_2S as regards the pit growth kinetics. As judged from the linear part of the curves in Figure 4.6, it appears as a reasonable approximation to assume that the actual pit depth (δ) is representative of the diffusion length[7] for pit depths greater than 0.4mm (i.e. lower than $25cm^{-1}$), independent of H_2S/CO_2. As a consequence, the numerical diffusion model[7] is assumed valid for calculating the surface concentration of dissolved species with H_2S/CO_2 present in the test solution. The transient responses in one of the curves in Figure 4.6 may stem from instable S-induced dissolution, but are regarded as insignificant to the measurements since these phenomena not are observed beyond 0.4mm.

4.4.2 Overvoltage curve

The polarisation curves are measured in the 1m*M* H_2S solution as described in the experimental procedure and they refer to three pit depths (i.e. 0.40, 0.50 and 0.67mm). In all cases the concentration at the solution/metal interface is close to the saturation level. The potentials were IR-corrected and the curves are plotted in the log *i vs. E* diagram in Figure 4.7. It can be seen from the figure that the different polarisation curves tend to overlap. A simple regression analysis yields the following Tafel equation:

$$E = 51 \cdot \log i - 279 \text{ (in mV SCE)} \qquad (4.9)$$

Equation (4.9) shows that the potential is independent of the pit depth and only a function of the current density as long as a salt film is not present at the metal surface. To enable a fair comparison the corresponding overvoltage curve obtained in the absence of H_2S in Part III are plotted in the same diagram. This curve has a Tafel slope of 57mV/dec. It follows that the overvoltage curves established in the absence and in the presence of H_2S tend to overlap. This indicates that H_2S/CO_2 not influence the dissolution kinetics, even when the salt film is removed beforehand.

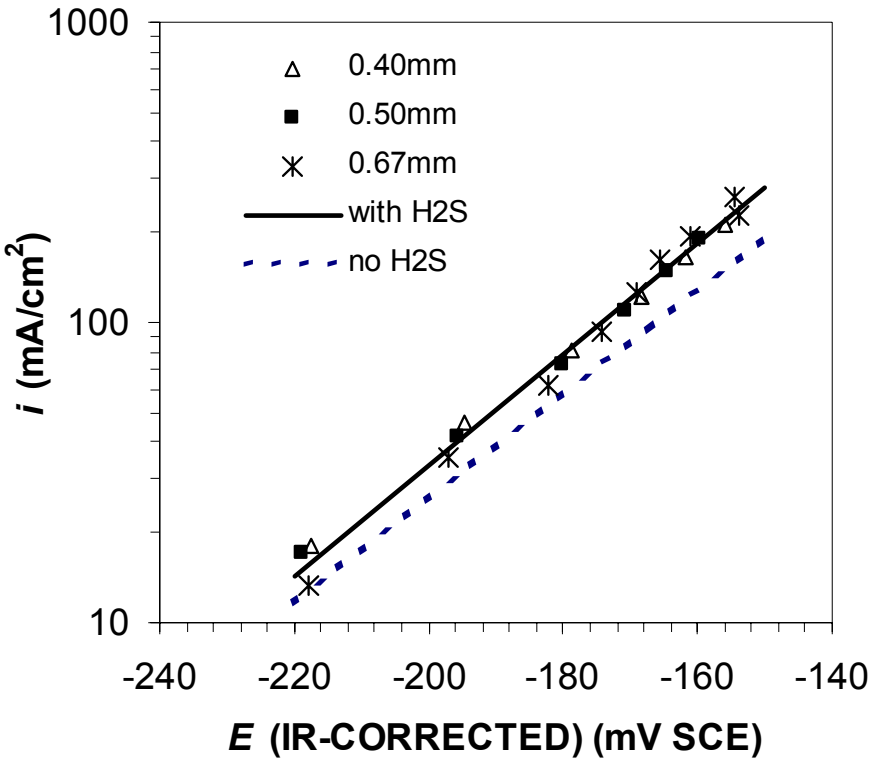

Figure 4.7. Summary of IR-corrected polarisation curves obtained at various pit depths (i.e. 0.40, 0.50 and 0.67mm, respectively) in the 1m*M* H_2S solution. The solid line represents the mean overvoltage curve obtained in the absence of H_2S in Part III.

4.4.3 Repassivation measurements

Repassivation measurements are carried out as described in the test procedure, in 1m*M* and 4m*M* H_2S solutions, at varying potentials (i.e. –250, –200 and –150mV SCE) for a range of pit depths. Raw data curves (i.e. current density transients without IR-corrections) from measurements in the 1 and 4m*M* H_2S solutions are shown in Figures 4.8 (a), (b), (c) and (d), (e), (f), respectively. To enable a fair comparison, corresponding data recorded in the absence of H_2S in Part III at –150 and –200mV SCE are plotted in the notified figures marked as "no H_2S", whilst no data are available at –250mV SCE. These transients reflect the symbiotic relationship between the dissolution kinetics and the surface concentration of dissolved species. Initially, the current passes through a local maximum before the passive current is reached. At larger pit depths the maximum value is lower owing to the increased IR-drop. At the same time, the time to repassivation increases due to a slower reduction of the concentration of dissolved species on the metal surface. Any deviation from this behaviour could therefore indicate a possible effect of H_2S/CO_2.

(a)

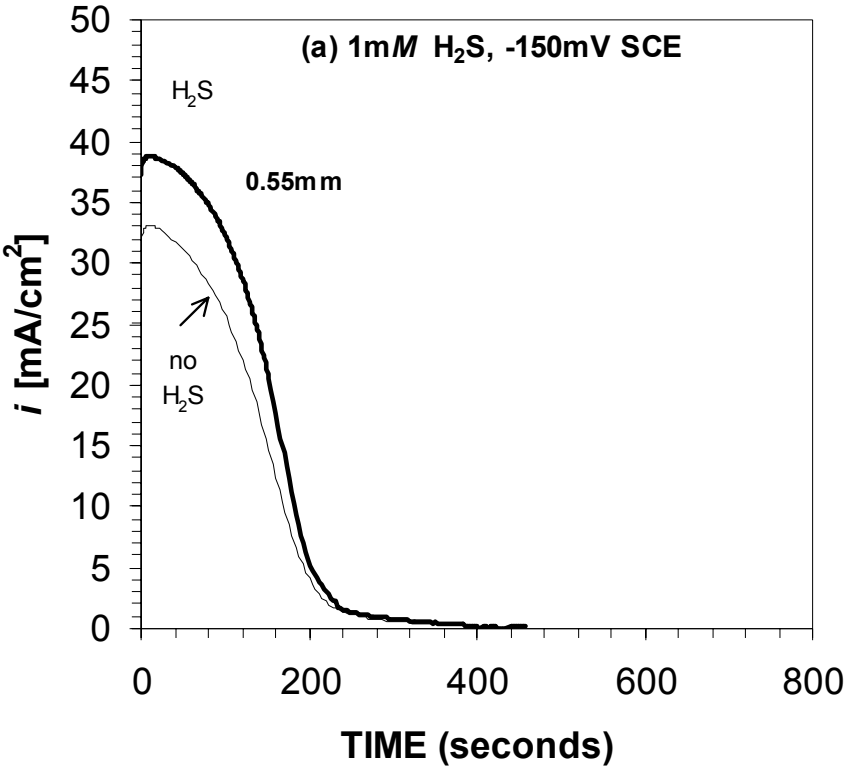

(b)

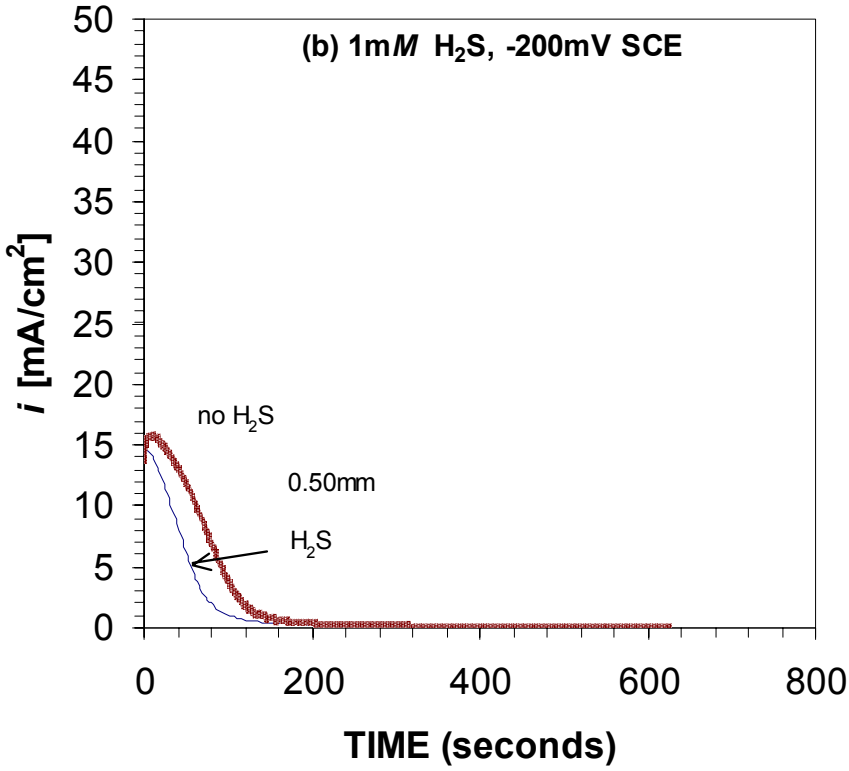

(c)

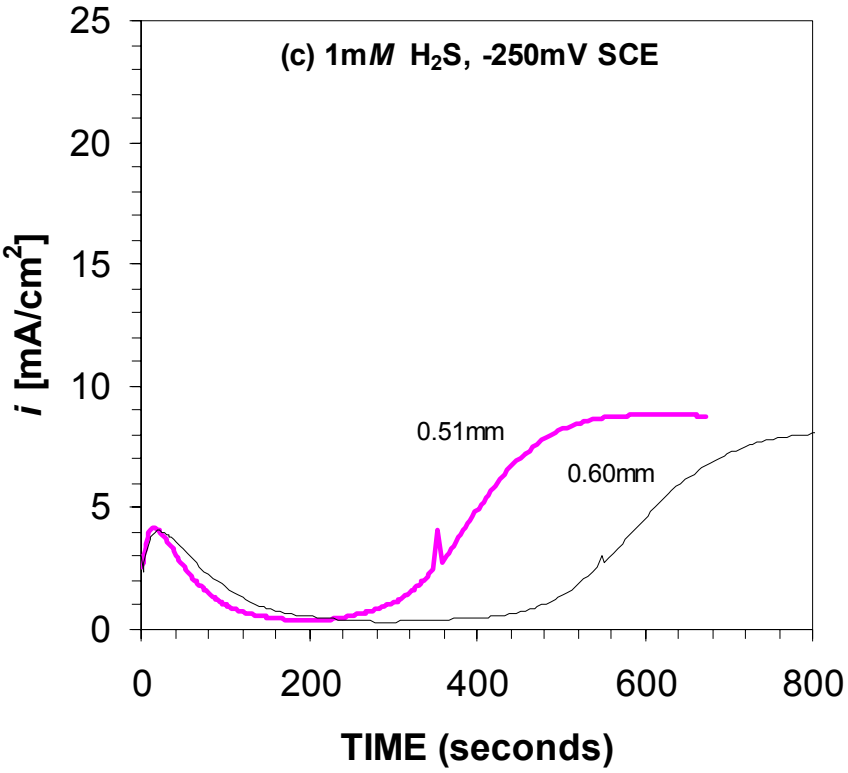

(d)

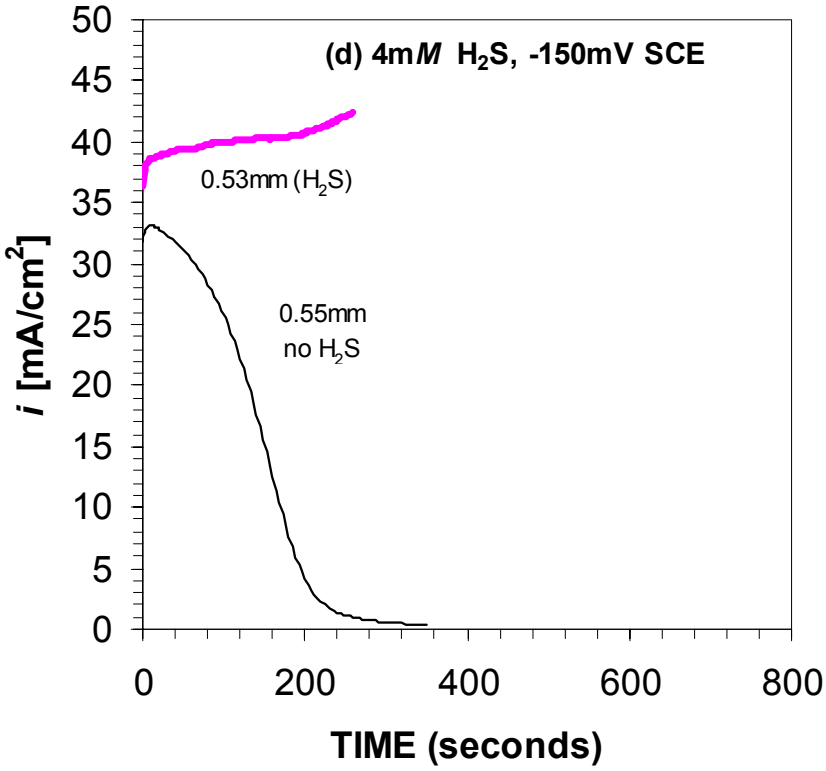

(e)

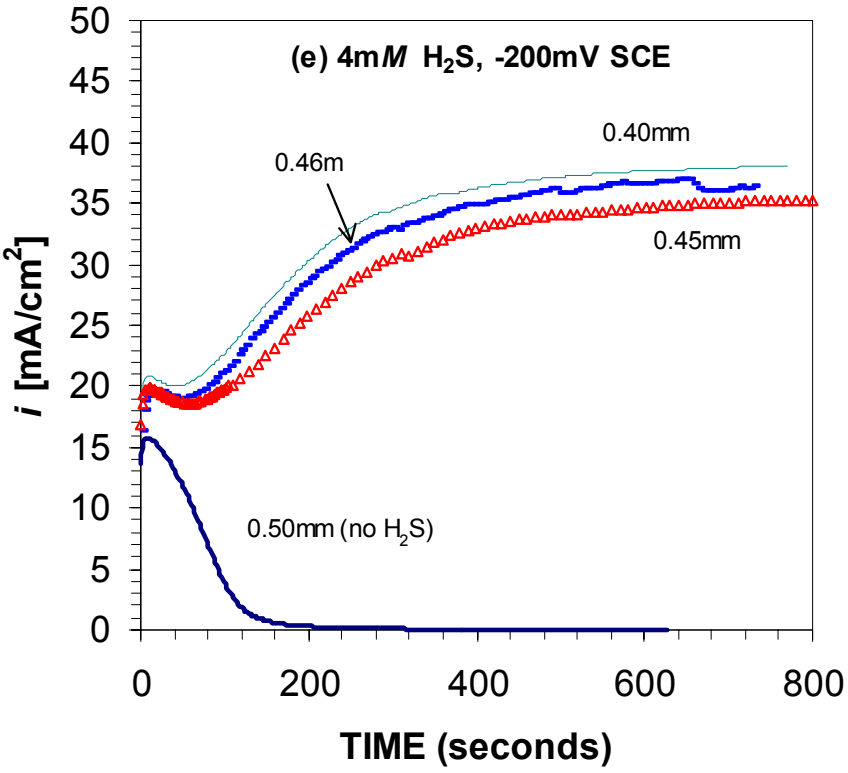

(f)

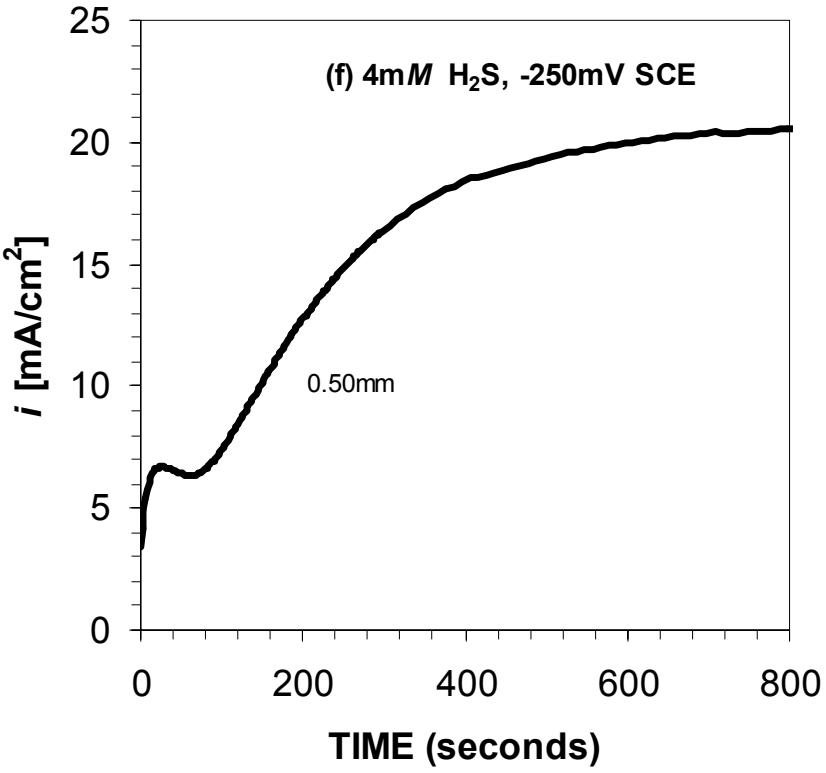

Figure 4.8. Summary of measured repassivation transients in 1m*M* H_2S at (a) −150mV SCE, (b) −200mV SCE and (c) −250mV SCE, and in 4m*M* H_2S at (d) −150mV SCE, (e) −200mV SCE and (f) −250mV SCE.

Starting with the 1m*M* H_2S solution, Figures 4.8 (a) and (b) show that the transients recorded at −150 and −200mV SCE followed similar paths as without any H_2S/CO_2 in the test solution, which indicate a lack of impact of H_2S on the dissolution and repassivation kinetics. However, at −250mV SCE, the transients deviate from the behaviour outlined above, referring to Figure 4.8 (c). These commenced along the normal path during the first 200 seconds, but rather than completing the repassivation process, re-activation and even acceleration of active dissolution occurred. Finally, the transients approach steady state levels. At 4m*M* H_2S, there is only a small tendency to repassivation at −200mV SCE, whilst no such tendency is observed at −150mV SCE, referring to Figures 4.8 (d), (e) and (f). Note that the measurement at −150mV SCE was terminated before any steady state level was reached. The prevention of repassivation and acceleration of active dissolution of the surface is, as shown, strongly linked to the H_2S concentration. Also the magnitude of the current reached during steady state is found to be H_2S dependent, as seen by comparing Figures 4.8 (c) and 4.8 (f). The current increased from 9 to 20mA/cm^2 as the H_2S content was increased from 1 to 4m*M*. This strongly indicates that the phenomenon observed is a demonstration of H_2S influenced corrosion.

As shown, the effect of H_2S is dependent on the potential and is favoured by low potentials. This potential dependency is contrary to pitting corrosion in stainless steels[12], but bears a close resemblance with reported effects of small amounts of thiosulphate on a Fe-19Cr-10Ni alloy[18]. Fe-19Cr-10Ni was, as referred earlier, found to repassivated above −250mV SCE. This was explained in terms of overstepping the stability potential of S_{ads}. It will later be discussed if the potential dependency observed in the 1m*M* H_2S solution may be associated with this effect and if it occurs also in the 4mM solution.

To get an impression of the concentration of dissolved species at the pit surface, calculations are done by means of the numerical algorithm[23] from Part III. Normalised surface concentration C_N of dissolved species are calculated based on the actual measurements are calculated and plotted in the *i vs.* C_N diagram in Figure 4.9. A closer inspection of the Figure 4.9 reveals that active dissolution is maintained at C_N levels of only 5 – 10% of saturation, which is well below the critical concentration of about 30% observed in the 1*M* NaCl solution in Part III.

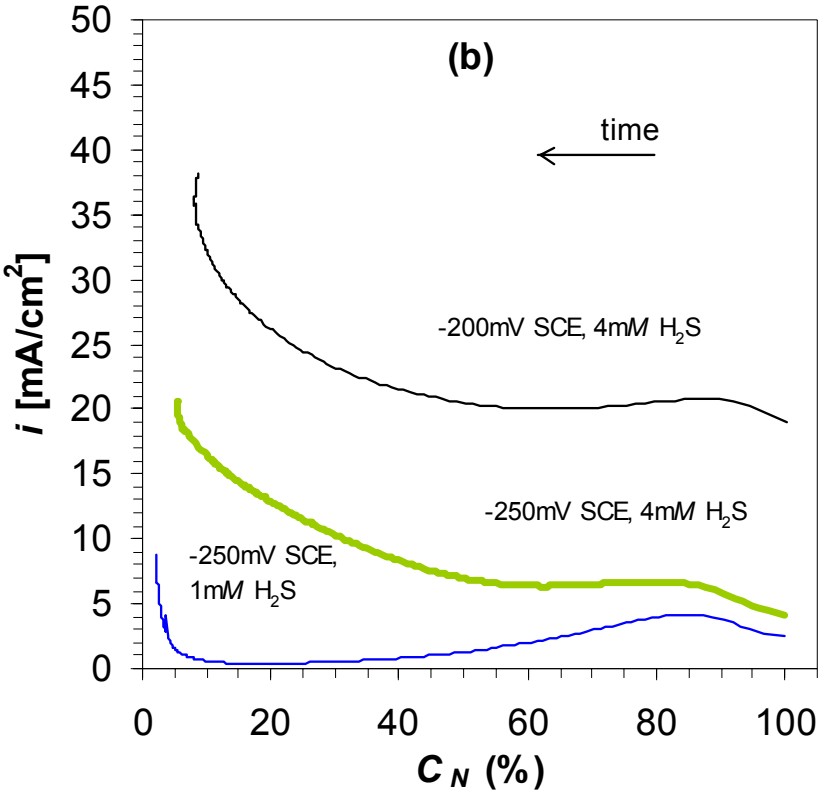

Figure 4.9. Plots showing current density *i vs.* normalised concentration C_N in H_2S solutions with re-activation.

4.4.4 Assessment of the relationship between the potential and the occurrence of S-induced dissolution

Separate measurements were carried out in the 1m*M* H_2S solution to examine the relationship between S-induced dissolution and the electrochemical potential more in detail. The first part of the measurement was carried out according to the repassivation test procedure, whereby the concentration gradient in the pit was established with saturation concentration at the pit surface. But rather than maintaining *E* at a certain value, *E* was varied to arouse and to choke S-induced dissolution in order to determine a possible threshold potential. The results from this measurement are shown in Figures 4.10 (a) and (b), and can be summarised as follows. As *E* was reduced to –200mV SCE at (*I*), the current density transient declined as if no H_2S was present. The small increase in *i* observed after 380s was probably due to an automatic change of the measuring resistor. At (*II*), *E* was lowered 50mV and further 25mV to –275mV SCE at (*III*) in an attempt to re-activate the surface. The response transient shows a gradually increase at (*II*) that becomes even more pronounced at (*III*). In fact, *i* increased

one order of magnitude in less than one minute. At that moment time the value of C_N was esteemed lower than 1%. This shows that corrosion may initiate and propagate at near bulk concentrations. The results also confirm the previously observed relationship between re-activation and potential. In order to substantiate this further, E was reset to −200mV SCE at (*IV*) whereby i immediately dropped nearly two orders of magnitude in less then one minute. As E was shifted back to −275mV at (*V*), the pit re-activated again inasmuch as i increased two orders of magnitude in 20s. For the purpose of determining the threshold potential for re-activation, E was then (i.e. from 560s off) increased in steps until a distinctive repassivation could be observed. It appears from Figure 4.10 (b) that repassivation occurred as E was shifted from −240 to −230mV SCE at (*VIII*). For the purpose of validating the observed threshold potential further, E was lowered at (*IX*) (i.e. from 700s off) in small steps until re-activation occurred at about −235mV SCE.

These measurements have demonstrated a certain "on/off" potential associated with activation and deactivation of S-induced dissolution in the 1m*M* H_2S solution, and is determined to be about −235mV SCE under the prevailing test conditions in what is assumed to be a diluted pit solution. The *pH* in the bulk solution is determined by the concentration of CO_2 and is calculated to be 3.8. Comparing this level of the "on/off" potentials with the equilibrium potentials plotted in Figure 4.1 indicates a coincidence with H_2S oxidation (i.e. Equation (4.4)) at a *pH* of about 3.8. This tends to affirm the conclusions in the previous section, which is H_2S depletion at the pit surface due to oxidation that may promote repassivation of S-induced dissolution below the upper stability limit for S_{ads}. Further, this is consistent with literature data[17] suggesting that S_{ads} atoms are removed with dissolving metal atoms.

(a)

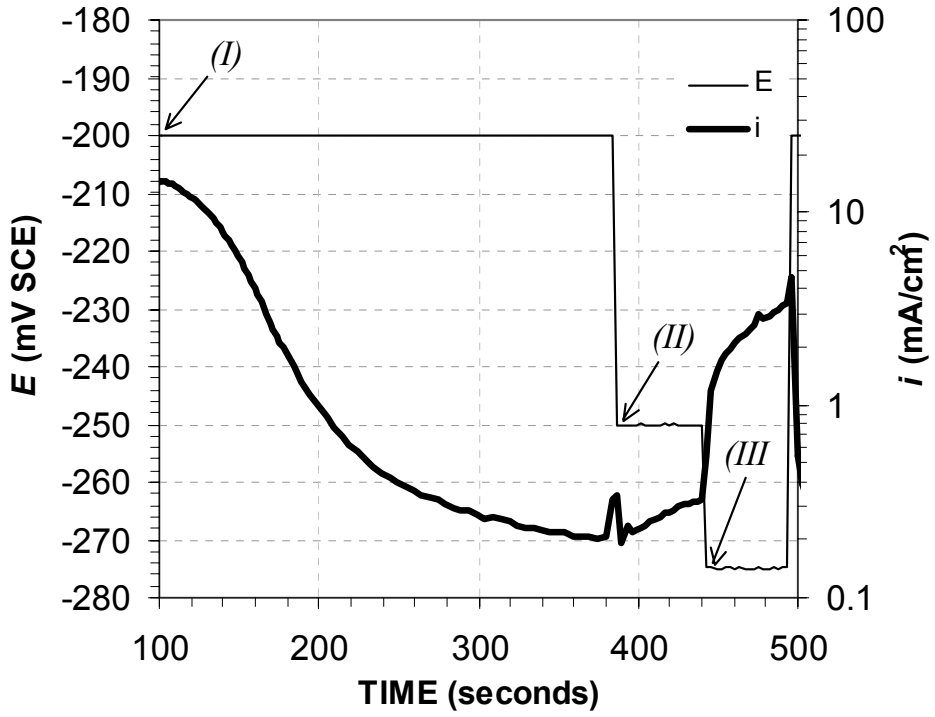

(b)

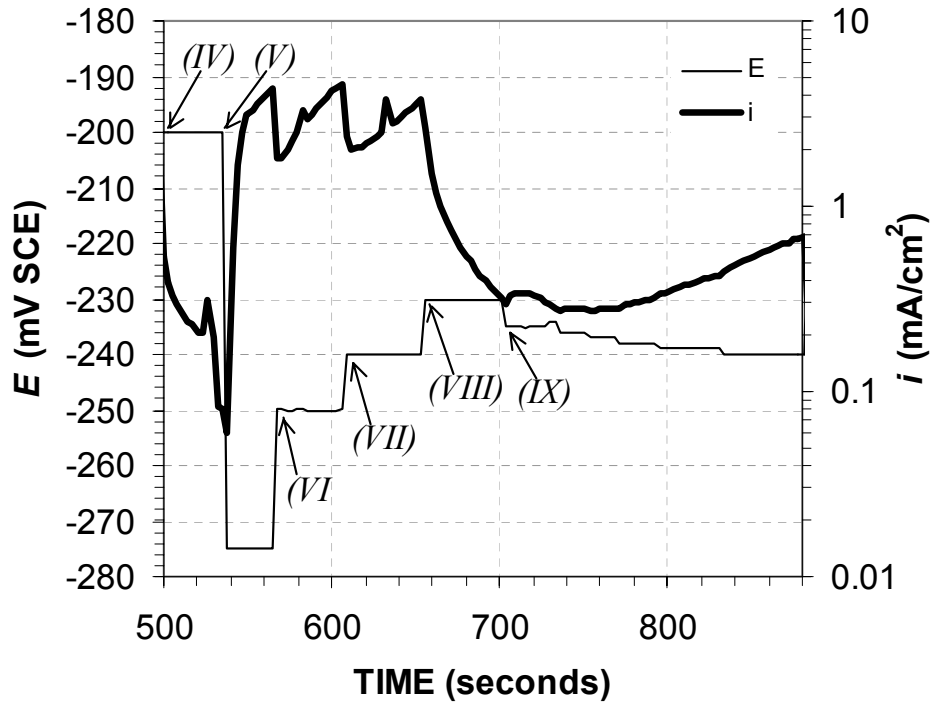

Figure 4.10. Plot of the applied potential and the current density transients from a potentiostatic test in a 1m*M* H_2S solution, where (a) shows the first 500s and (b) from 500s off.

4.4.5 Potentiodynamic measurements of S-induced dissolution

A modified potentiodynamic test procedure was invented to provide further information about the impact of H_2S on anodic dissolution of the SMSS alloy. First, the desired pit depth was obtained by anodic dissolution at 400mV SCE. Next, S-induced dissolution was generated by utilizing galvanostatic control (i.e. 0.5mA/cm^2), whereby E finally stabilized at about −500mV SCE. Then the galvanostatic control was turned off and potentiostatic control immediately re-established at about −500mV SCE until the current density stabilised. After that, E was elevated in steps of 20mV/minute up to 0mV SCE.

Measurements were carried out in the 1 and 4m*M* H_2S solutions and the IR-corrected results are plotted in the *E vs.* log *i* diagram in Figure 4.11 (a) together with the overvoltage curve obtained in the absence of H_2S in Part III (i.e. "no H_2S"). Notice that each data couple was recorded just prior to the elevation of E. Each curve followed, referring to Figure 4.11 (a), characteristic patterns comprising active dissolution from –500mV SCE until repassivation occurred at about –250mV SCE in 1m*M* H_2S or –200mV SCE in 4m*M* H_2S, followed by a passive region, before a gradually rise in the current density finally occurred above –200mV SCE. The high dissolution rates from −500mV SCE off represent S-induced active dissolution, where the H_2S contents account for different dissolution rates. Repassivations of S-induced dissolution occur immediately at similar potentials as in the previous measurements and are hence associated with H_2S depletion at the pit surface. A comparison between the transient responses during repassivation supports that conclusion. Figure 4.11 (b) shows the transients during repassivation of the 0.32mm pit in the 1m*M* H_2S solution, and bears a close resemblance to the transient at observed following the respective escalations of the potential at (*VI)* and (*VII)* in Figure 4.10 (b).

Referring to Figure 4.11 (a), the increases in current densities from –200mV SCE off represent probably development of active dissolution in an increasingly aggressive pit solution. In fact, as the applied potential was kept constant at 0mV SCE, the current density approached steady state level. This appears from Figure 4.11 (c), where the IR-corrected potentials have been plotted versus the current density at a constant applied potential of 0mV SCE. The cross indicate the steady state values, and a comparison with the re-plot of the overvoltage curve from Figure 4.7 substantiate further that the H_2S effect vanishes above a certain potential level.

(a)

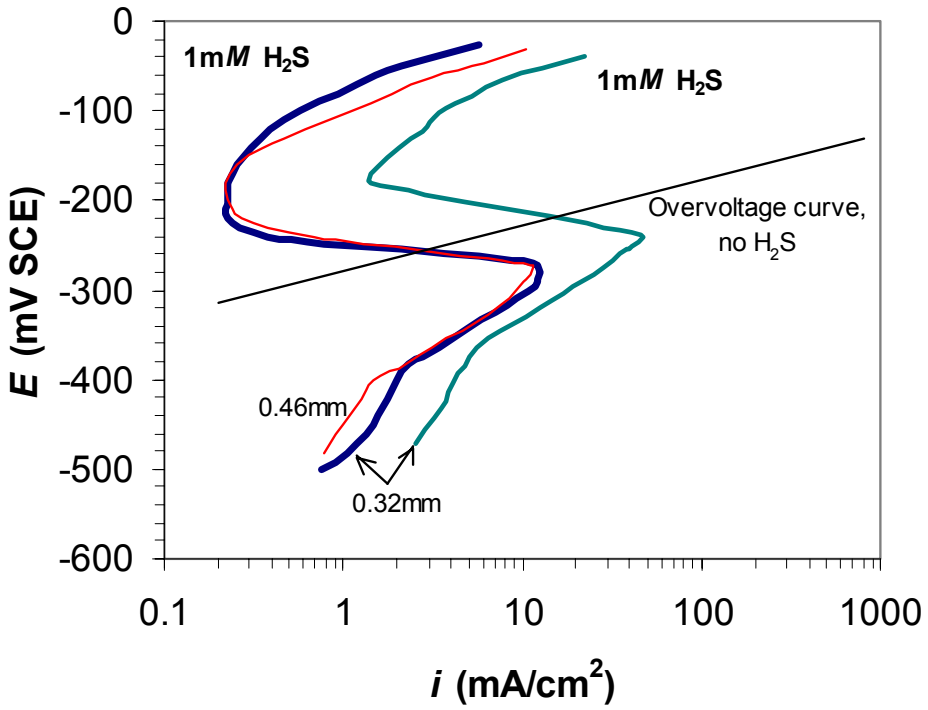

(b)

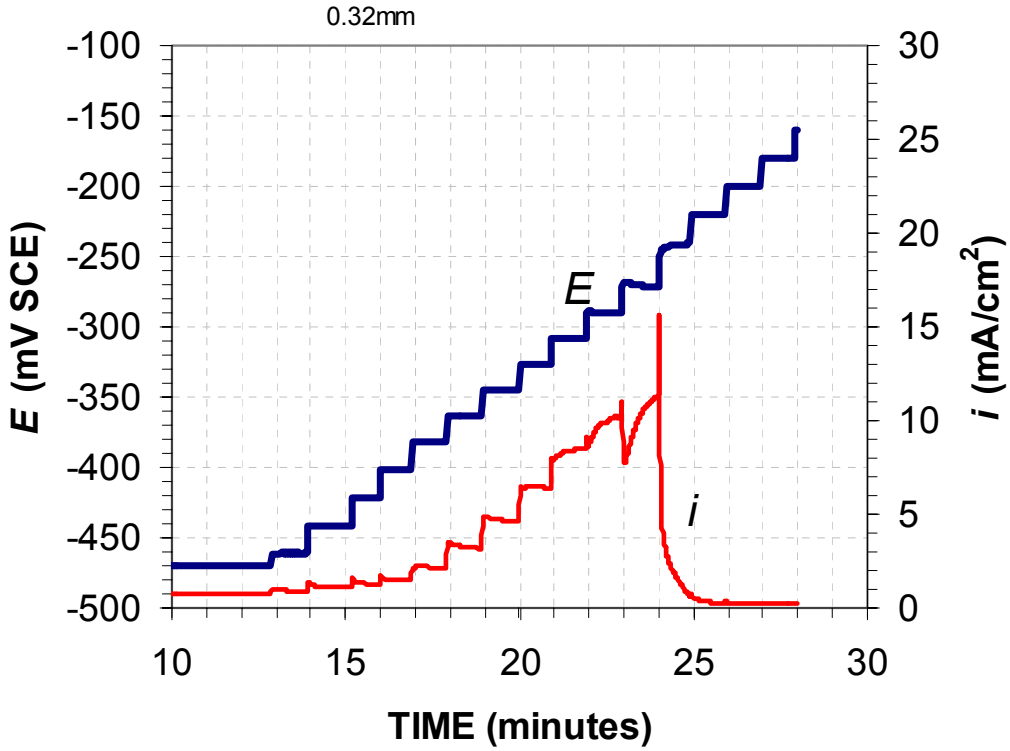

(c)

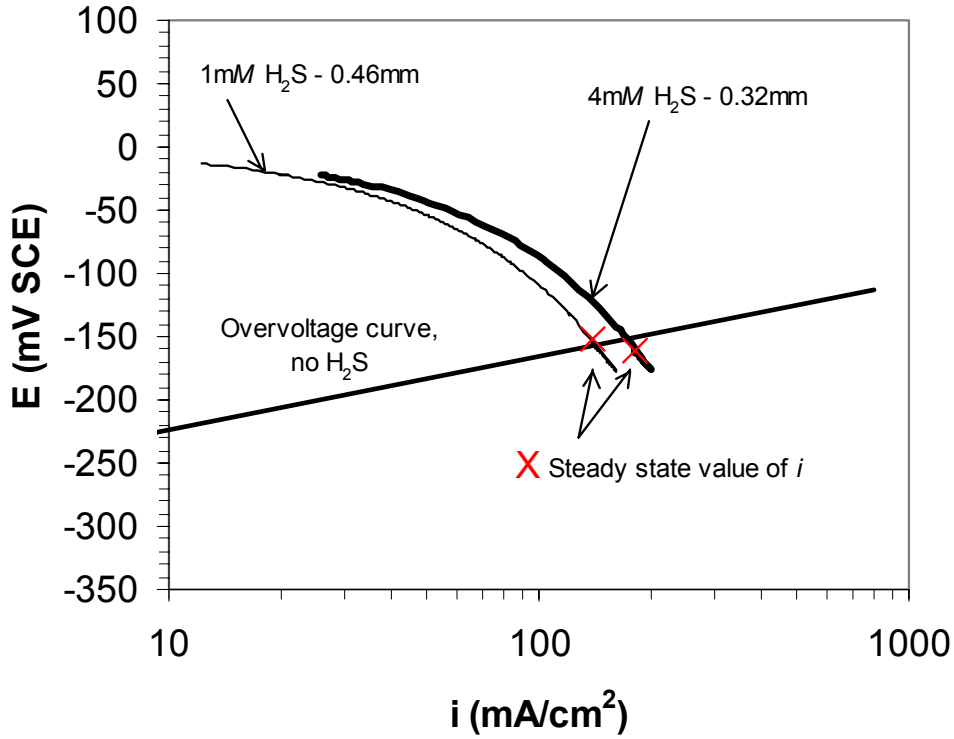

Figure 4.11. IR-corrected plots from potentiostatic measurements at various H_2S concentrations. (a) Plot of data couples recorded just prior to the elevation of E using a scan rate of 20mV/minute. (b) Plot of current density transients *vs.* *E* as the applied potential are maintained at 0mV following the potential step measurements plotted in (a). (c) Plot of raw data for the 0.32mm deep pit in 1m*M* H_2S.

4.5 CONCLUSIONS

The dissolution and repassivation kinetics of a super martensitic stainless steel (SMSS) exposed to a 1*M* NaCl solution at ambient pressure and 22°C with 10mbar (i.e. 1m*M*) and 40mbar (i.e. 4m*M*) H_2S has been characterised using the so-called "artificial pit" technique. The basic conclusions that can be drawn from the investigation can be summarised as follows:

Addition of a critical amount of H_2S is found to hinder repassivation and accelerate active dissolution of an artificial SMSS pit. The active dissolution sustained by H_2S is denoted "S-induced dissolution".

The effect of H_2S is observed within the potential-*pH* stability domain of specifically adsorbed sulphur.

The effect of H_2S is found to be dependent on potential and H_2S concentration and is favoured by low potentials.

Above what is assumed to be the redox potential of H_2S/S, the effect of H_2S ceases and a simple Tafel type of approach can hence describe the dissolution kinetics of the SMSS alloy.

The S-induced dissolution rate depends on the H_2S concentration.

S-induced dissolution appears stable and SMSS pits do not repassivate even at low surface concentrations.

4.6 REFERENCES

1. J. Enerhaug, S. L. Eliassen, P. E. Kvaale: *Corrosion/97*, paper no. 60, (Houston, TX: NACE International, 1997).
2. J. Enerhaug, P.E. Kvaale, M. Bjordal, J.M. Drugli, T. Rogne: *Corrosion/99*, paper no. 587, (Houston, TX: NACE International, 1999).
3. K. Tamaki: *Corrosion/89*, paper no. 469, (Houston, TX: NACE International, 1989).
4. A. Miyasaka. H. Ogawa: *Corrosion/90*, paper no. 67, (Houston, TX: NACE International, 1990).
5. S. Hashizume, T. Takaoka, Y. Minami, Y. Ishizawa, T. Yamada: *Corrosion/91*, paper no. 28, (Houston, TX: NACE International, 1991).
6. M. Ueda, T. Kushida, T. Mori: *Corrosion/95*, paper no. 80, (Houston, TX: NACE International, 1995).
7. M. Kimura, Y. Miyata, T. Toyooka, F. Murase: *Corrosion/99*, paper no. 582, (Houston, TX: NACE International, 1999).
8. H. Amaya, M. Ueda: *Corrosion/99*, paper no. 585, (Houston, TX: NACE International, 1999).
9. J. M. Drugli, T. Rogne, *A literature Study of SSC- and Corrosion testing of alloyed Chromium Steels*, SINTEF report STF24 F02226, Trondheim, 2002.
10. J. M. Drugli, *Korrosjon av skjøter – Korrosjon av rustfrie stål i miljø med høye partialtrykk av CO_2 – en litteraturstudie,* SINTEF report STF16 F85118, Trondheim, 1985.
11. T. Rogne, J. M. Drugli, "*Elektrokjemiske egenskaper for sveiser på rustfrie stål i brønnstrømsmiljø,*" SINTEF report STF16 F86130, Trondheim, 1986.
12. H. Miyuki, J. Murayama, T. Kudo, T. Moroishi: *Corrosion/84*, paper no. 293, (Houston, TX: NACE International, 1984).
13. T. Rogne, R. Johnsen: *Corrosion/92*, paper no. 295, (Houston, TX: NACE International, 1992).
14. T. Rogne, J. M. Drugli: *Corrosion/93*, paper no. 644, (Houston, TX: NACE International, 1993).
15. J. Oudar: *Introduction to Surface Reactions: Adsorption from Gas Phase*. ("Corrosion Mechanisms in Theory and Practice", P. Marcus and J. Oudar eds.). Marcus Dekker, 1995, pp. 19-53.
16. P. Süry, *Corros. Sci.*, 1976, vol. 16, pp. 879-901.
17. P. Marcus: *Sulfur-Assisted Corrosion Mechanisms and the Role of Alloyed Elements*. ("Corrosion Mechanisms in Theory and Practice", P. Marcus and J. Oudar eds.). Marcus Dekker, 1995, pp. 239-263.
18. S. Mat, R. Newman: *Corrosion/94*, paper no. 228, (Houston, TX: NACE International, 1993).

19. P. Marcus, E. Protopopoff, *J. Electrochem. Soc.,* 1990, vol. 137, pp. 2709-2712.
20. P. Marcus, E. Protopopoff, *J. Electrochem. Soc.*, 1997, vol. 144, pp. 1586-1590.
21. P. Marcus, E. Protopopoff, *J. Electrochem. Soc.*, 1993, vol. 140, pp. 1571-1575.
22. R. C. Newman, *Corrosion*, 1985, vol. 41, pp. 450-453.
23. MultiScale® is a computer programme developed at NTNU, Trondheim, by Baard Kaasa and Terje Østvold for Statoil, Norsk Hydro and Saga Petroleum.
24. G. T. Gaudet, W. T. Mo, T. A. Hatton, J. W. Tester, J. Tilly, H. S. Isaacs, R. C. Newman, *AIChE J.*, 1986, vol. 32, pp. 949-958.
25. U. Steinsmo, H. S. Isaacs, *J. Electrochem. Soc.*, 1993, vol. 140, pp. 643-653.
26. Z. Szklarska-Smialowska, *Pitting Corrosion of Metals*, NACE, 1986.

APPENDIX 4.1. NOMENCLATURE

b_a anodic Tafel slope, mV/decade
C_N normalised surface concentration of dissolved species
E potential, mV SCE
F Faraday constant, 96 485 C/mol
i current density, mA/cm^2
I current, mA
I_{lim} diffusion-controlled current, mA
I_{max} maximum current, mA
M_w average molecular weight, g/mol
n average metal valence, equivalent/mol
Q total electricity, C
R_b bulk solution resistance, Ω
R_s total resistance, Ω
R_p pit solution resistance, Ω
r wire radius, mm
S_{ads} specifically adsorbed sulphur
t time, s
α solution resisitivity, Ωmm
δ pit depth, mm
ρ density, g/cm^3

PART V: EFFECTS OF SURFACE CONDITION AND H_2S ON LOCALIZED CORROSION IN SUPER MARTENSITIC STAINLESS STEEL WELDMENTS

5.1 INTRODUCTION

The oil companies involved in the recent field development projects such as Gullfaks Satellites, Åsgard[1,2] and Tune carried out their test programmes on the super martensitic stainless steel (SMSS) girth welds in accordance with guidelines provided by EFC 17[3]. They demonstrated satisfactorily pitting resistances of the SMSS weldments at elevated temperatures of 90-140°C, whereas corrosion tests carried out in artificial formation water (40mbar H_2S, *pH* 4.5-6) and in simulated condensed water (8mbar H_2S, *pH* 3.5) at ambient temperature revealed a susceptibility to localized corrosion[2,4] of the inner pipe surface close to the fusion boundary. These attacks were characterised by rather high dissolution rates of the order of 1-5mm/year at potentials of about −500mV SCE. These results contradict the normal temperature dependency of CRA's, and reopen the whole question whether the corrosion properties of SMSS alloys differ in a fundamentally manner from those of other classes of CRA's. It is thus of vital importance for the end-users of such flowlines to clarify whether this is merely a laboratory effect or if it represents a potential operational problem which needs to be considered in the future.

5.2 SUMMARY OF CURRENT KNOWLEDGE AND SCOPE OF WORK

In Part II of this thesis, the quality of the root surface was judged to be a key factor regarding occurrence of pitting corrosion in SMSS weldments under slightly sour conditions and to be more important than the underlying microstructure. These results showed that the high temperature oxidation reactions occurring during welding modified the root surface and reduced the resistance towards pitting corrosion, in spite of the low oxygen content in the root shielding gas (i.e. <150ppm O_2). During electrochemical measurements, pitting occurred in the HAZ close to the fusion boundary in the solution which contained H_2S, whereas the oxidised root surface repassivated in the H_2S-free solution after a certain amount of anodic dissolution. This is thought to occur following the removal of the thin Cr-depleted zone in the oxidized region[5]. Hence, it is suggested that H_2S, in combination with an oxidized root surface, is the primary cause of the anomalous temperature dependence observed in SMSS weldments during corrosion testing. This implies that initiation of H_2S assisted dissolution is extremely sensitive to the initial surface condition of the CRA.

In the comparative study of the dissolution and repassivation behaviour of SMSS and other stainless grades in Part III, the evolution of single, artificial pits

in a 12.3Cr-6.5Ni-2.6Mo alloy was examined in a 1*M* NaCl solution. The SMSS alloy behaved as the other CRA's in the sense that no anomalies were disclosed that couldn't readily be accounted for by compositional effects. However, by adding H_2S to the test solution, the pitting corrosion mechanism changed, as shown in Part IV. For example, it was found that the addition of 1m*M* H_2S (i.e. 10mbar) hindered repassivation even at potentials below −500mV SCE, and did increase the anodic dissolution rate by several orders of magnitudes to a level which is comparable to that observed in the previous corrosion tests[1,2].

Generally, the effects of H_2S and other sulphur compounds on corrosion of metals and alloys are ascribed to the influence of specifically adsorbed sulfur atoms (denoted S_{ads}) on the alloy surface[6]. S_{ads} is found to be stable, also beyond the stability domain of the metal sulphides, and may promote pitting corrosion as follows[6]: Firstly, S_{ads} may stabilize otherwise unstable (or metastable) pits, whereby the critical pitting potential is reduced. Secondly, S_{ads} may preclude and hinder repassivation by sustaining active dissolution under conditions where the pit otherwise would repassivate. Thirdly, S_{ads} may accelerate anodic dissolution due to the catalytic nature of the accelerating effect of S_{ads}. This corrosion mechanism is, however, a potential problem in all CRA's and is not restricted to SMSS alloys. Other sulphur compounds are reported to have similar effects by contributing to S_{ads}, and an example is thiosulphate in contact with Fe-19Cr-10Ni[7].

In summary, it may be stated that the combination of H_2S and a vulnerable root surface is the main reason for pitting corrosion in SMSS weldments at ambient temperatures. The increased resistance towards S-induced pitting at elevated temperatures can accordingly be explained in terms of effective dissolution and repassivation processes occurring at such temperatures, which, in turn, removes the surface that is vulnerable to S-induced dissolution. The present study therefore seeks to substantiate the effect of the initial root surface condition and the role of H_2S in a more explicit manner and to establish a descreptive model that takes these factors into account in an attempt to explain the underlying experimental observations.

5.3 EXPERIMENTAL PROCEDURE

5.3.1 Materials and welding

The base material was received in the form of 10'' diameter seamless pipe from a Japanese steel manufacturer (Sumitomo) through the Åsgard Project. The wall

thickness was 20mm and the pipe was delivered with pickled surfaces, using HNO_3 + HF and H_2SO_4. The steel chemical composition is shown in Table 5.1. The base composition of approximately 12%Cr, 2.5%Mo and 6.5%Ni places this pipe material in the "high alloyed" category of the SMSS.

Table 5.1. Chemical compositions of pipe material, filler wire and weld metal (in wt%).

	C	Cr	Mo	Ni	P	S	Si	Mn	V	Cu	W	Co	Al	Ti
Pipe	0.01	12.2	2.5	6.4	0.018	0.002	0.12	0.48	0.04	0.08	0.03	0.11	0.03	0.12
Wire	0.012	12.37	2.65	6.37	0.01	0.001	0.50	0.67						
Weld	0.011	12.2	2.7	6.5				0.49		0.06				

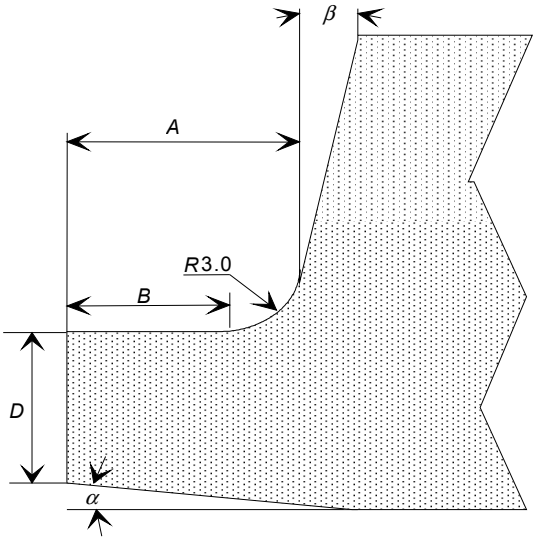

D= 2.75 ± 0.25 mm, *B*= 2.25 ± 0.2 mm,
A= 5.25 ± 0.3 mm, α= 6° and β= 7°

Figure 5.1. Schematic diagram showing the pipe bevel preparation.

Table 5.2. Summary of welding parameters.

Pass type	Welding current (I_p/I_b), [A]	Arc voltage [V]	Weaving amplitude [mm]	Weaving rate [mm/s]	Welding speed [mm/s]	Wire feed rate [m/min]	Dwell time on high pulse [ms]
Root weld	170/90	13	1.0	2.5	1.0	0.50	400

Two girth welds (i.e. W1 and W2) were made in a remotely controlled welding chamber, using GTAW with pulsed current. A Ø1mm Thermanite 13/06 filler wire (produced by Böhler/Thyssen) was selected as welding consumable, which is a "high alloyed" wire developed for matching the SMSS base material, with chemical composition as given in Table 5.1. The two pipe ends to be joined were bevelled in a lathe machine, and the final groove joint geometry is shown in Figure 5.1. The root face (land thickness) was machined to 2.75 mm, and no joint misalignment between the pipes was allowed. The welding was performed with zero root gap. Further, the torch was located in the 11 o'clock position during the root pass welding (i.e. the 1G position), using the welding parameters listed in Table 5.2. Before welding, the chamber was flushed with inert gas mixture, while a shielding gas consisting of 70%He and 30%Ar was purged through the chamber during welding. The oxygen content in the chamber was estimated to about 150ppm prior to deposition of W1, while it was maintained at 140ppm during production of W2 by adding a certain gaseous mixture to the chamber. The chemical composition of the weld metal is given in Table 5.1.

5.3.2 Corrosion testing

The aim of the corrosion testing is to reproduce the corrosion attacks observed in SMSS girth welds in the previous tests[1,2] by means of potentiodynamic (PM) and galvanostatic (GM) measurements. To enable a fair comparison, some few tests were carried out in a deaerated 1*M* NaCl solution (i.e. PM), while the main part of the program (i.e. PM and GM) was carried out in a 1m*M* H_2S (i.e. 10mbar H_2S and CO_2 (balance)) and 1*M* NaCl solution. In the latter case 4.88m*M* sodium acetate (i.e. 0.4 g/litre) was added as a buffer and the *pH* was adjusted to 4.5 by addition of HCl.

Specimens were taken from the base plate and the actual weldments (i.e. W1 and W2), and the width and length of the specimens was about 13mm and 40mm, respectively. The specimens that were used in the potentiodynamic tests were covered with either bees' wax or lacquer. However, due to problems with crevice corrosion, the subsequent tests were accomplished without any cover, where the side edges apart from the intact root surface were ground with a 1000 grit paper. In a separate galvanostatic test the intact root surface was carefully modified, using a rotating grinding paper until the colourful oxide layer was removed. All specimens were provided with a ∅2mm drilled hole for connection of the platinum wire. Finally, the specimens were rinsed in an ultrasonic bath (i.e. in acetone) and washed in ethanol.

The corrosion tests were carried out at ambient temperature (22±1°C) and pressure in 2 litres glass cells. A saturated calomel electrode (SCE), separated

from the test solution by a salt bridge, was used as reference electrode, while a platinum net served as counter electrode. Each specimen was coupled, mechanically and electrically, to a platinum wire through the lid, as shown in Figure 5.2.

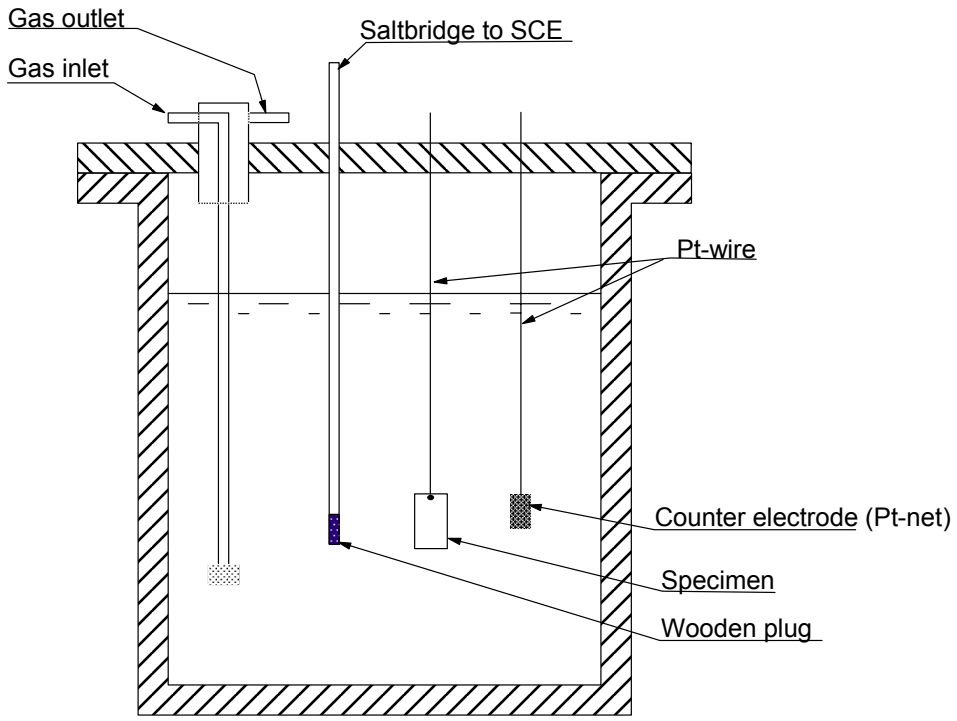

Figure 5.2. Test equipment for corrosion testing (schematic).

Firstly, the oxygen was removed from the test solution by means of nitrogen purging for at least 15 hours before the specimen was inserted into the test solution. Next, the purging rate was increased as the specimen was inserted into the solution. After some more minutes, the nitrogen gas was replaced with the actual gaseous mixture (i.e. 1% H_2S and 99% CO_2), except in the initial tests containing no H_2S. The electrochemical measurements were carried out using a Solatron SI 1286 unit, controlled by in-house PC programmes. In the potentiodynamic measurements the potential of the specimens was swept from the open circuit potential to well above the pitting potential, using a sweep rate of 20mV/min. In the galvanostatic measurements current densities of 0.01 or 0.02A/m^2 were imposed on the specimens. The current was then calculated on the basis of the total area of the specimen. During each test the potential transient was recorded. Further details are given in Table 5.3.

Table 5.3. Summary of experimental conditions in potentiodynamic and potentiostatic corrosion measurements.

Sample	Weld	Measuring method	Test solution
A	Base metal	Potentiodynamic	1*M* NaCl
B	W1	Potentiodynamic	1*M* NaCl
C	W1	Potentiodynamic	1*M* NaCl
D	W2	Potentiodynamic	1m*M* H_2S, 4.88m*M* NaAc, 1*M* NaCl
E	Base metal	Potentiodynamic	1m*M* H_2S, 4.88m*M* NaAc, 1*M* NaCl
F	W2	Potentiodynamic	1m*M* H_2S, 4.88m*M* NaAc, 1*M* NaCl
G	W2	Potentiodynamic	1m*M* H_2S, 4.88m*M* NaAc, 1*M* NaCl
H	W1	Potentiodynamic	1m*M* H_2S, 4.88m*M* NaAc, 1*M* NaCl
I	W1	Potentiodynamic	1m*M* H_2S, 4.88m*M* NaAc, 1*M* NaCl
J	W1	Galvanostatic – 0.01A/m^2	1m*M* H_2S, 4.88m*M* NaAc, 1*M* NaCl
K	W2	Galvanostatic – 0.02A/m^2	1m*M* H_2S, 4.88m*M* NaAc, 1*M* NaCl
L	W2	Galvanostatic – 0.01A/m^2	1m*M* H_2S, 4.88m*M* NaAc, 1*M* NaCl
M	W2 ground surface	Galvanostatic – 0.01A/m^2	1m*M* H_2S, 4.88m*M* NaAc, 1*M* NaCl

5.4 RESULTS AND DISCUSSION

In Part II of this thesis, it was shown that an iron-rich oxide covered the oxidized root surface of weld W1 with a maximum thickness of about 250nm close to the fusion boundary. This underlines the fact that the root surfaces in SMSS weldments are oxidized during welding. The various notations applied in the text to describe the welded samples are defined in Figure 5.3. It follows that the "parent material" includes the bulk pipe material apart from the HAZ. The "oxidized root surface" and the "non-oxidized pipe surface" confine the inner pipe surface that is modified by high temperature oxidization during welding and the intact pipe surface, respectively, whilst the "fusion boundary" is the boundary between the weld metal and the pipe material.

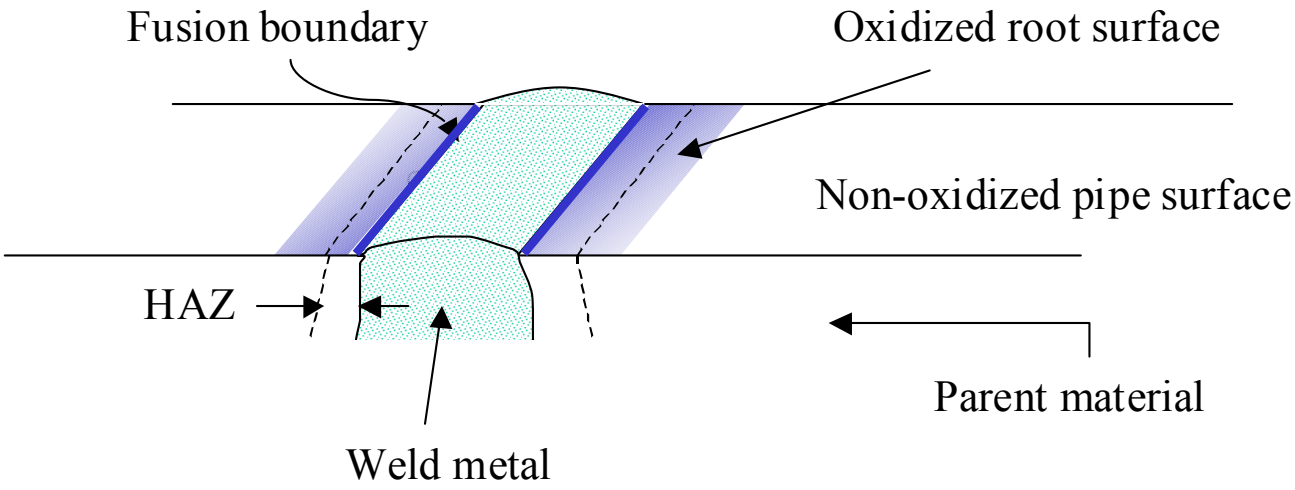

Figure 5.3. Definitions and notations used in the text to describe the root side of the SMSS weld.

In the following, the results from the corrosion tests will be presented and discussed, starting with potentiodynamic measurements in test solutions with and without H_2S, respectively. Next, results from the galvanostatic tests in the presence of H_2S are presented and discussed. Finally, a descriptive pitting corrosion model is proposed to explain the effect of the root surface condition and the role of H_2S.

5.4.1 Potentiodynamic measurements in the absence of H_2S

The polarisation curves are measured in a deaerated 1*M* NaCl solution, as described in the experimental procedure and plotted in the *E vs.* log(*i*) diagram in Figure 5.4. Notice that the fluctuation in *i* close to E_{CORR} is due to instable measuring resistors. It follows that the base material specimen (A) is passive

below the pitting potential of about −100mV SCE. The weld samples (B, C, D) exhibit, on the other hand, two pitting potentials; one lower and one upper.

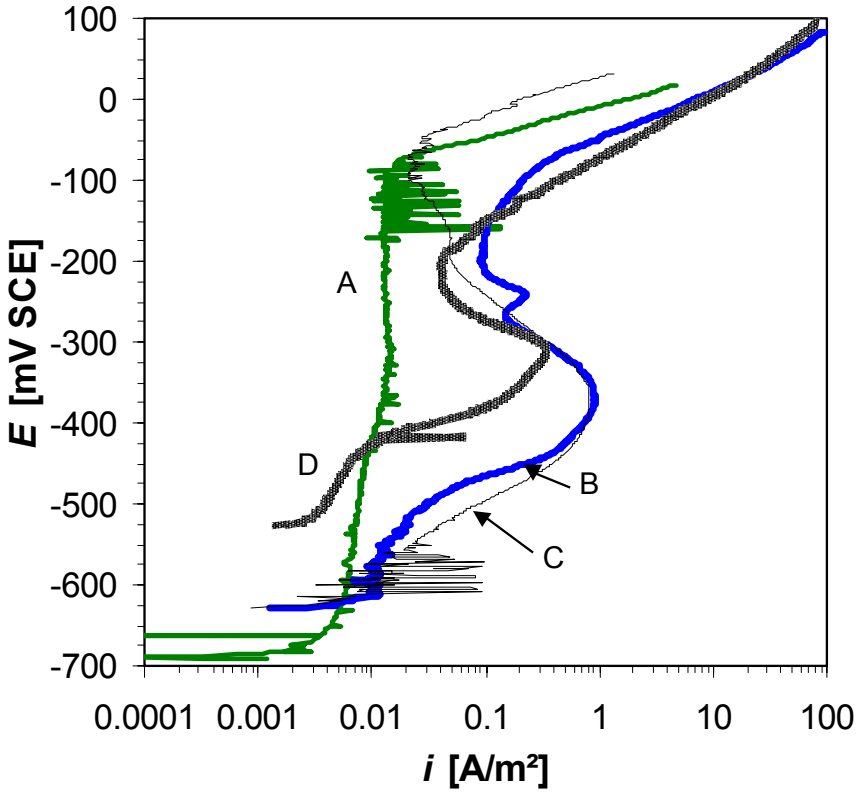

Figure 5.4. Measured polarisation curves in deaerated 1*M* NaCl without any H_2S.

A closer inspection of Figure 5.4 shows that samples (B), (C) and (D) are passive below the lower pitting potentials of −550mV SCE for (B) and (C) and −420mV SCE for (D), respectively. The open circuit potential of sample (D) is about 100mV higher than the corresponding values for the other specimens. This is probably due to traces of oxygen in the solution. Above their lower pitting potential, the weld samples (B, C, D) seem to first undergo active dissolution, followed by repassivation. This corresponds to the "nose"-shaped part of the polarisation curves ranging from −500mV SCE to −200mV SCE. This appearance bears a resemblance to the shape of the potential transients recorded in the galvanostatic measurements carried out under similar experimental conditions in Part II. Some representative transients are re-plotted in Figure 5.5 to enable a fair comparison. Referring to this figure, the characteristic plateau of about −500mV SCE is assumed to represent an ongoing modification process of the oxidized root surface, involving both active dissolution and repassivation, whereas the final increase in *E* indicates the completion of repassivation.

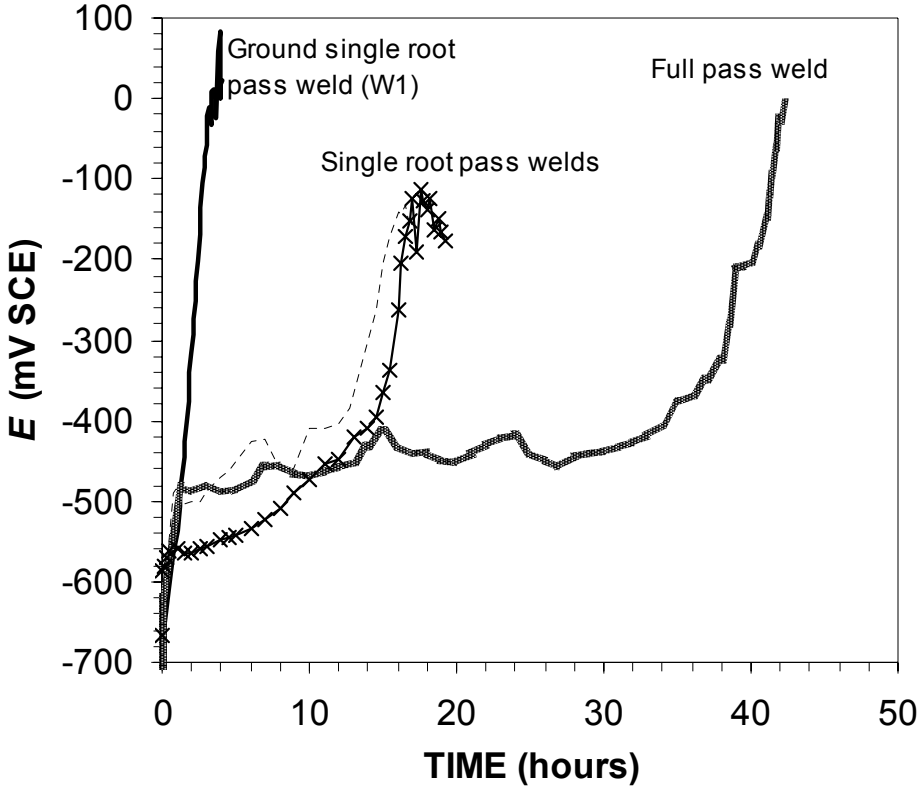

Figure 5.5. Measured potential transients during galvanostatic testing of SMSS weldments in deaerated 1*M* NaCl (from Part II of this thesis).

The upper pitting potential, on the other hand, lies about −200mV SCE in all cases, as shown in Figures 5.4 and 5.5. A visual inspection of samples (B), (C) and (D) displayed 100μm deep pitting attacks located about 8 to 9mm from the fusion boundary as well as in the weld metal. On the other hand, no attacks were observed in the oxidized root surface close to the fusion boundary, which again is consistent with the results from the galvanostatic measurements.

5.4.2 Potentiodynamic measurements in the presence of H_2S

The measured polarisation curves in the presence of H_2S are plotted in Figure 5.6. It follows that the parent material specimen (E) displays a lower and an upper pitting potential at −350 and 0mV SCE, respectively. The lower pitting potential probably reflects the occurrence of S-induced pitting corrosion, whereas the subsequent drop in the current density at −275mV SCE needs some further explanation. A sharp decrease in the anodic current density of this kind has also been observed by Mat and Newman[8] at −130mV SCE during a potentiodynamic scan of 316L stainless steel carried out at 80°C in a 0.6*M* NaCl solution containing 0.03*M* H_2S. The authors ascribed this phenomenon to depletion of H_2S due to oxidation taking place on the passive surface, which will occur above the H_2S/S redox potential. Hence, there will be no supply of H_2S to

activate the pits, which most likely contributes to the repassivation observed in the present investigation. Moreover, a comparison between Figure 5.6 and Figure 5.4 shows that the levels of the upper pitting potentials in the parent material samples are quite similar, which implies that the effect of H_2S is rather weak under the prevailing circumstances.

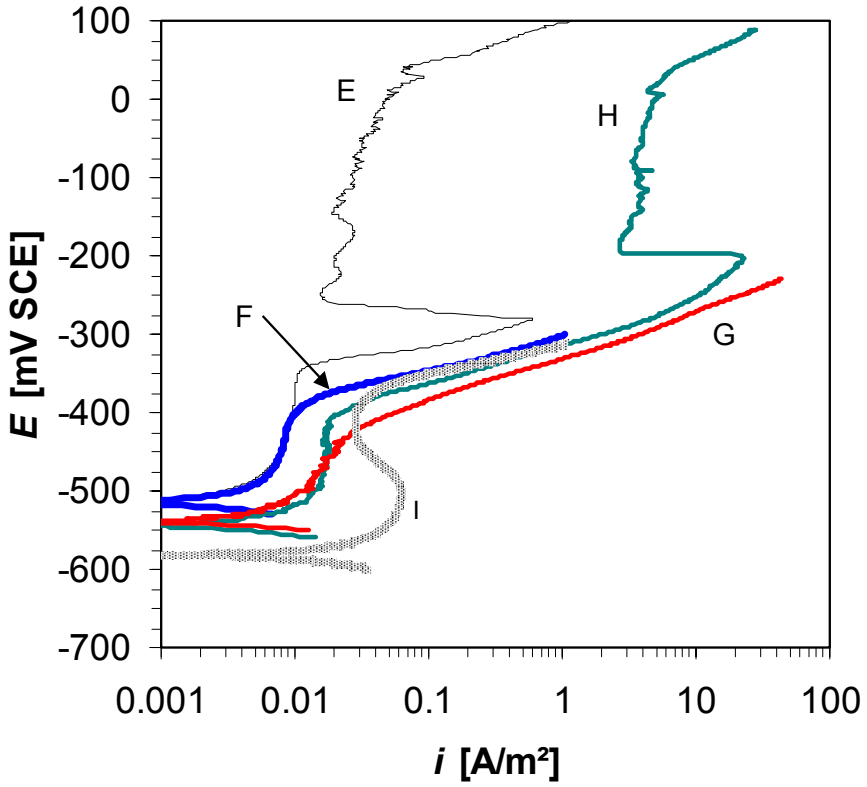

Figure 5.6. Measured polarisation curves in the solution containing 1m*M* H_2S (10mbar H_2S, CO_2 (balance)).

Furthermore, Figure 5.6 reveals the existence of a lower pitting potential in the weld samples (D, F, G, H, I) in the presence of H_2S at about –400mV SCE. This is about 100mV higher than the corresponding values observed in the H_2S-free solution, shown in Figure 5.5. The results seem to be in conflict with the reported effect of H_2S, which is to assist the pitting corrosion[6]. This is probably due to a higher oxidizing power of the (CO_2+H_2S) saturated solution, which leads to a modification of the surface prior to the polarisation measurement. Such surface oxidation phenomena can also explain the observed variations in passivity and the open circuit potential E_{CORR}, where sample (F) is seen to exhibit the lowest passive current and hence the highest E_{CORR}. A comparison between the weld sample (H) and the parent material sample (E) in Figure 5.6 shows a similar behaviour for the former sample, including an abrupt drop in the current density at about –200mV SCE, and a recorded upper level of the pitting corrosion potential at about 0mV SCE.

The visual inspection of the tested samples revealed localized attacks in three distinct regions; located 0-3mm, 5-6mm and 9-10mm, respectively, from the fusion boundary. These regions were examined in a Scanning Electron Microscope (SEM) and the results are shown in Figures 5.7 (a) - (c). Figure 5.7 (a) shows a close-up of corrosion attacks 3mm from the fusion boundary in sample (I). The pits appear shallow and concave, and the growth seems to occur laterally rather than in-depth in the vulnerable root area, which is characteristic of S-induced pitting corrosion. Moreover, Figure 5.7 (b) shows a close-up of corrosion attacks 5-6mm from the fusion boundary in sample (F). In this region, the corrosion occurs by spalling of the thick weld oxide and not by pitting corrosion, similar to that reported in Part II of the thesis in the absence of H_2S. Finally, Figure 5.7 (c) shows a close-up of pitting corrosion 9mm from the fusion boundary in sample (I). These pits are deep and resemble classical pitting attacks in stainless steels.

(a)

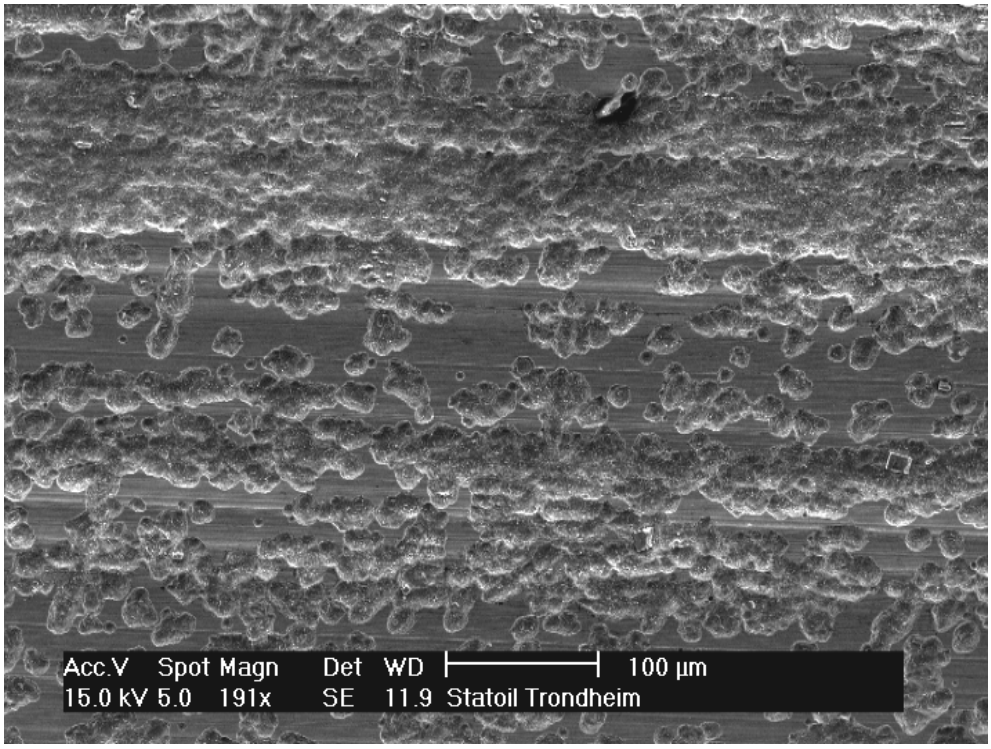

(b)

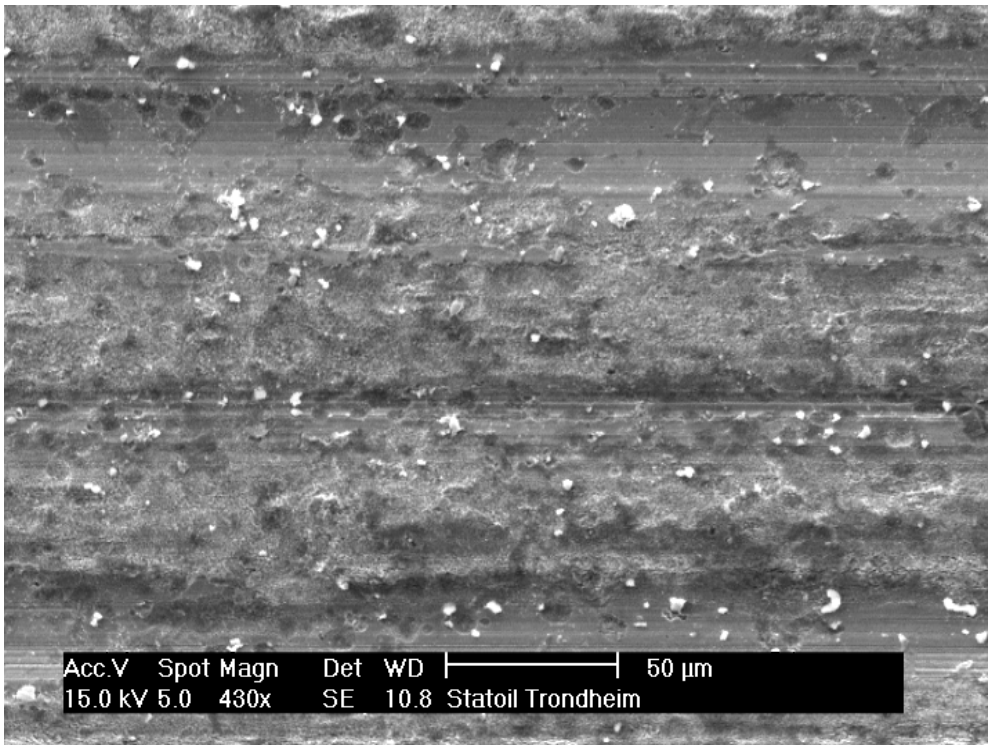

(c)

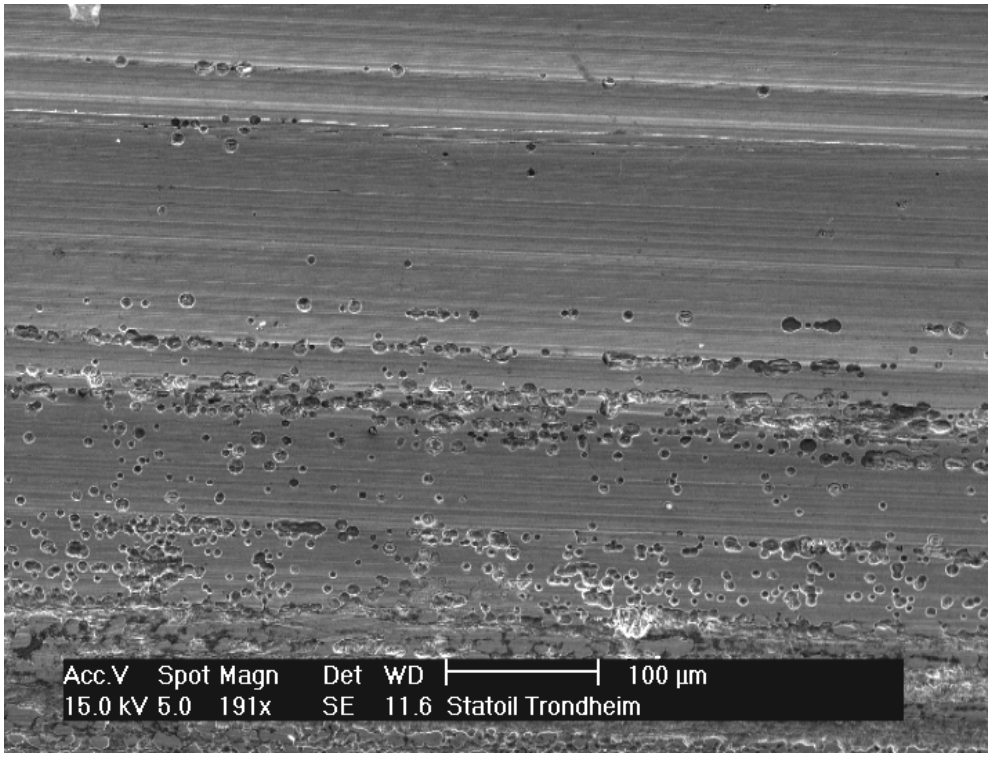

Figure 5.7. Scanning electron micrographs of corrosion attacks; (a) 3mm from the fusion boundary in sample (I), (b) 5mm from the fusion boundary in sample (F), and (c) 9mm from the fusion boundary in sample (I).

5.4.3 Galvanostatic measurements in the presence of H_2S

During the potentiodynamic measurements in the presence of H_2S, numerous localised attacks occurred in the oxidized root surface area. The attacks observed in previous SSC tests[1,2] are, on the hand, fewer, but deeper and wider. In an attempt to reproduce the pitting corrosion attacks observed during free exposure, an additional series of galvanostatic measurements has been performed using the H_2S containing test solution. The recorded potential transients are shown in Figure 5.8. It follows that the potential increases rapidly during the first minutes to about –400mV SCE, which corresponds to the lower pitting potential observed in the foregoing potentiodynamic measurements. A closer inspection of Figure 5.8 shows that the potential transients of the intact weld samples (J, K, L) pass through maxima before the stable potentials of about –540mV SCE are reached. This value is lower than the initial open circuit potential. These results indicate the occurrence and development of stable corrosion attacks, which is confirmed by visual inspection of the tested samples, displaying single attacks in the region located 0-3mm from the fusion boundary. The deepest attacks (50μm) correspond to an average dissolution rate of 0.5mA/cm^2 or about 5mm/year. These attacks appear as clusters of pits that seem to grow together beneath a surface layer, as shown in Figure 5.9. The attacks are hardly visible, but after scratching the surface with a sharp tool, a corroded structure appeared beneath. Moreover, shallow pits were observed in the region located 5-6mm from the fusion boundary. Also some random distributed attacks were detected in the oxidised root surface region, but no pits could be observed in the non-oxidized pipe surface.

The ground weld sample (M) stabilized, on the other hand, at –400mV SCE, where the transient response after 3 hours was due to a power failure. An inspection of the tested sample showed no signs of preferential corrosion in the region corresponding to the oxidized root surface (see Figure 5.3).

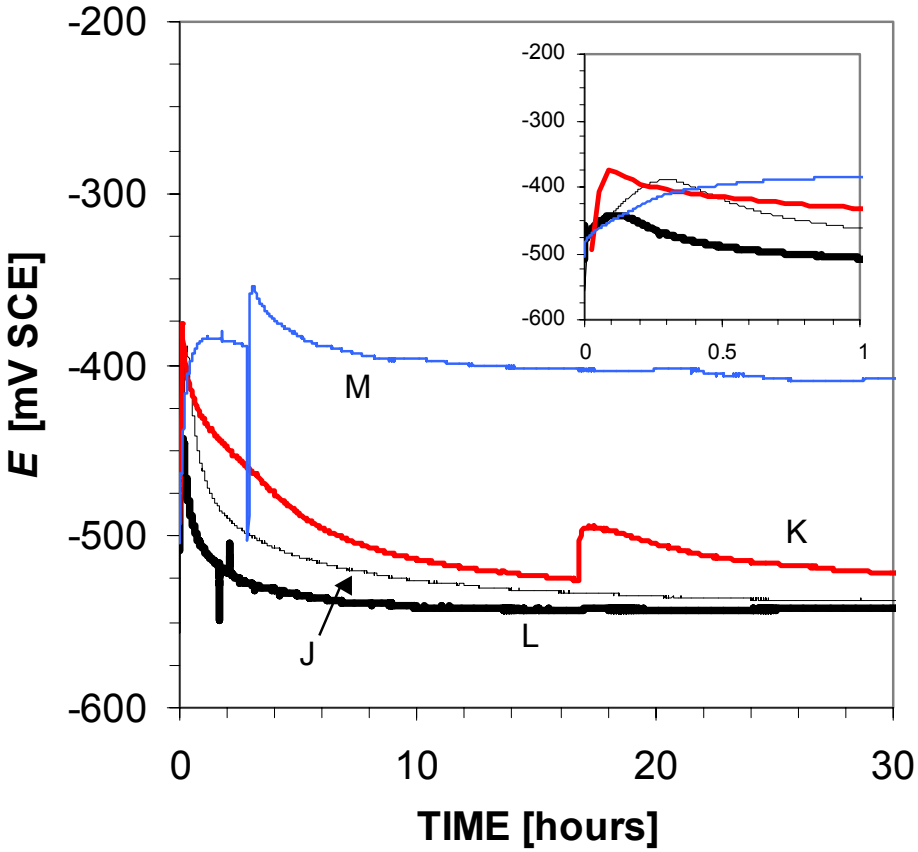

Figure 5.8. Measured potential transients during galvanostatic testing in a solution containing 1m*M* H_2S (10mbar H_2S, CO_2 (balance)).

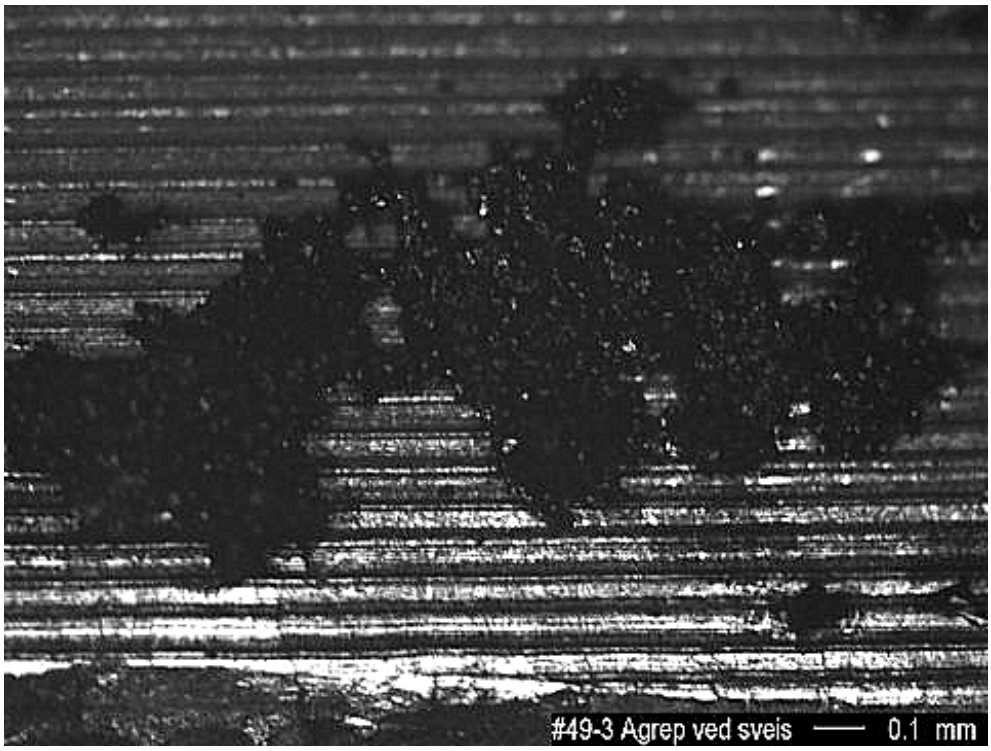

Figure 5.9. Close-up of localized corrosion attacks in the region 0-3mm from the fusion boundary in sample (K).

5.4.4 Descriptive models of pitting corrosion in SMSS weldments

The results from the corrosion testing can be summarized as follows, using the definitions given in Figure 5.3. High temperature oxidation processes occurring during welding[5] modify the SMSS pipe surface near the fusion boundary, as shown previously in Part II of this thesis. It follows that the "oxidized root surface" is more vulnerable to initiation of pitting corrosion than the non-oxidized pipe surface. This vulnerability is reflected by the "lower" pitting potential in the potentiodynamic measurements, which again can be attributed to initiation of localized dissolution in the oxidized regions. During the galvanostatic measurements the maximum potentials were limited to about –400mV SCE, and consequently visible, localized corrosion attacks occurred in the most oxidized root surface region. Furthermore, the observed decline in the potential transients subsequent to initiation of pitting corrosion confirms that H_2S hinders repassivation and accelerate anodic dissolution[6]. In fact, the H_2S assisted pitting corrosion occurs at a potential level that is comparable to the open circuit potentials in similar environments. This, in turn, explains the severe pitting corrosion observed at ambient temperature during the previous SSC corrosion tests[1,2].

In the following, a descriptive pitting model is proposed to explain the effect of the root surface condition and the role of H_2S, starting with the H_2S-free condition. Subsequently, the descriptive model is modified to account for the role of H_2S.

5.4.4.1 Pitting corrosion behaviour in the absence of H_2S

A descriptive model must account for the observations made in the corrosion tests, including the lower $E_P^{'}$ and the upper E_P pitting potentials as well as the repassivation process. Figure 5.10 (a) shows a sketch of an imaginary cross-section from the oxidized root surface region. It is assumed that the outermost metal (i.e. some few nanometres below the surface) is Cr-depleted owing to oxidation reactions occurring during welding. When $E_P^{'}$ is exceeded, micro-pits will start to form, as indicated in Figure 5.10 (a). The single pits are assumed to develop as suggested in Figure 5.10 (b). It follows that stage 1 represents the initiation period, whereas stage 2 represents a period of inwards and laterally growth, before the pit growth is limited to only laterally expansion. This is due to repassivation of the pit bottom as it approaches the bulk steel, which is higher in Cr. The Cr-depleted sidewalls do not repassivate, and the lateral expansion therefore continues until the pit impinge with other expanding pits. The repassivation process is completed when the corrosion process has removed the Cr-depleted layer and this defines the onset of stage 3. Schematic responses

during potentiodynamic and galvanostatic measurements are shown in Figure 5.11 (a) and Figure 5.11 (b), respectively.

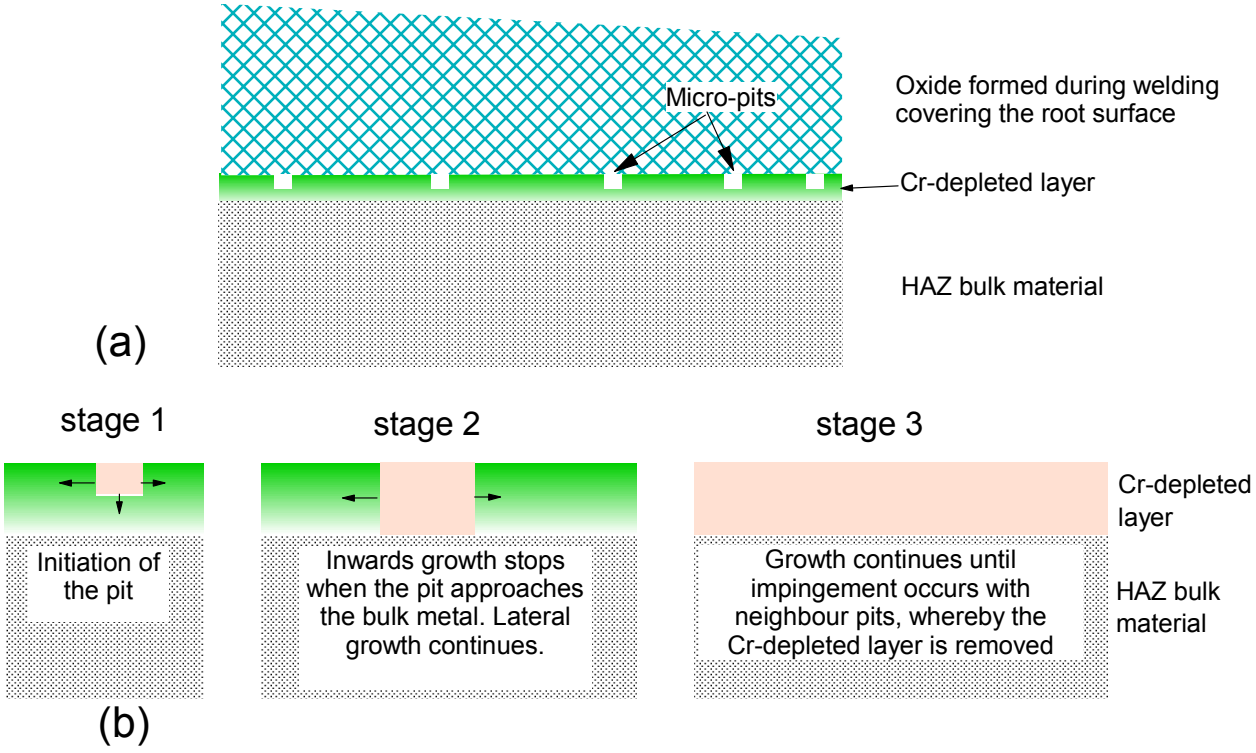

Figure 5.10. (a) Sketch of a cross-section from the root side in HAZ. The root surface is covered by an oxide that has been formed during welding. It is assumed that the substrate material contains a narrow layer that has been Cr-depleted. (b) Illustration of pit growth beneath the oxidized root surface during corrosion testing in the absence of H_2S.

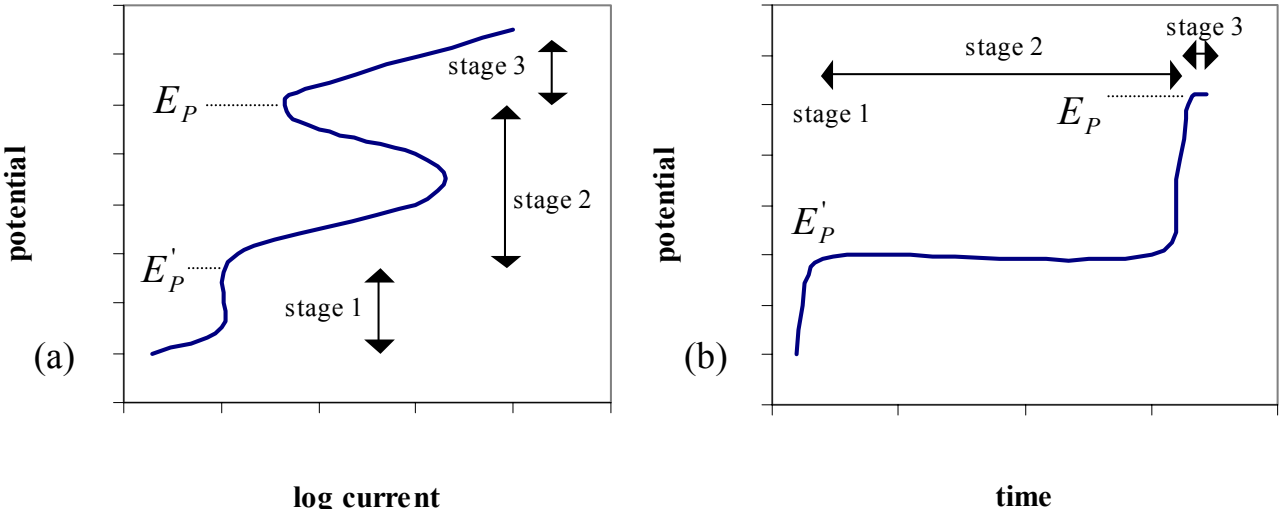

Figure 5.11. Schematic diagrams showing the corresponding responses during (a) potentiodynamic and (b) galvanostatic measurements in the absence of H_2S.

5.4.4.2 Pitting corrosion behaviour in the presence of H_2S

The descriptive pitting model can also be modified to include the observed effects of H_2S in the potentiodynamic and galvanostatic measurements. It is assumed that H_2S transforms the metastable pits in the oxidized root surface region into stable pits[6]. Hence, it is suggested that H_2S hinders repassivation as the pits penetrate the Cr-depleted layer, as outlined in Figure 5.12. Stage 1 represents initiation, whereas stage 2 represents the further development of the pit. The pit expands in all directions conforming to stage 2, whereby visible pits finally are created. Schematic responses during potentiodynamic and galvanostatic measurements are shown in Figure 5.13 (a) and Figure 5.13 (b), respectively.

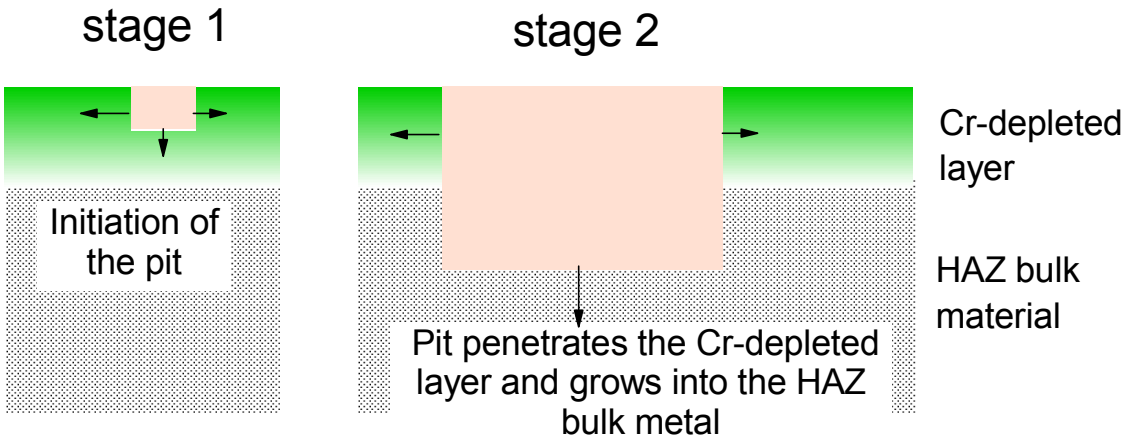

Figure 5.12. Illustration of pit growth beneath the oxidized root surface region during corrosion testing in the presence of H_2S.

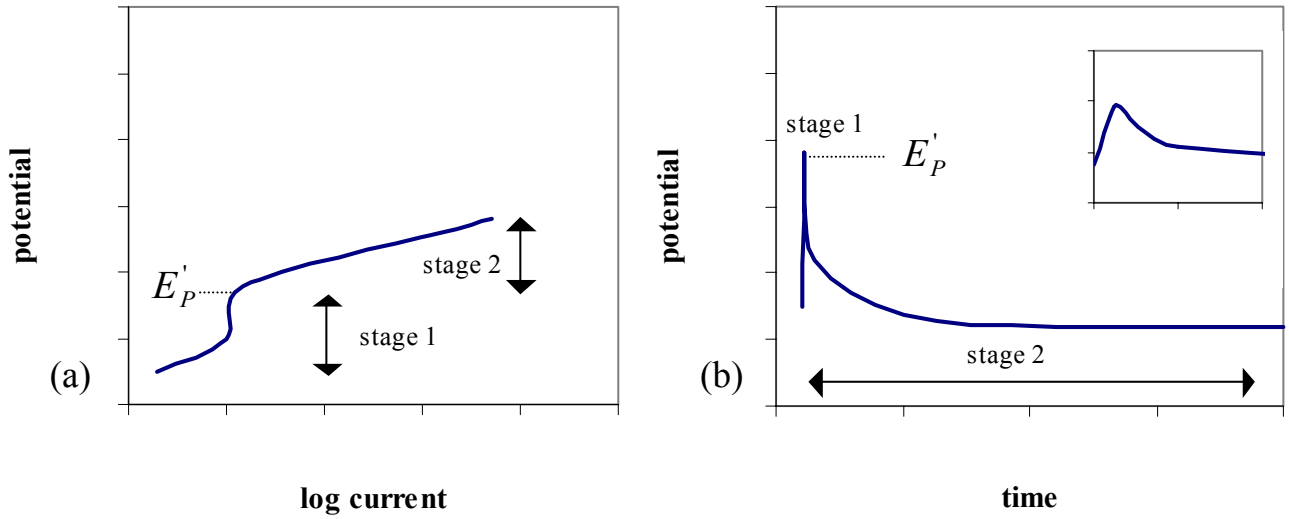

Figure 5.13. Schematic diagrams showing the corresponding responses during (a) potentiodynamic and (b) galvanostatic measurements in the presence of H_2S.

5.5 CONCLUSIONS

This investigation has demonstrated that high temperature oxidation processes occurring during welding lowers the measurable pitting potential in SMSS weldments.

In the absence of H_2S, metastable pitting corrosion occurs in the oxidized root surface close to the fusion boundary at the lower pitting potential $E_P^{'}$, whereas stable pitting corrosion occurs in the pipe surface outside the oxidized region at the upper pitting potential E_P.

In the presence of H_2S, the metastable pits become stable, whereby visible pits finally appear in the oxidized root surface 0 to 3mm from the fusion boundary.

Galvanostatic measurements carried out in the presence of H_2S at room temperature are found to produce pitting corrosion attacks that are similar to those observed in previous corrosion tests.

A descriptive pitting corrosion model is proposed to explain the effect of the root surface condition and the role of H_2S. This model is sufficiently relevant and comprehensive to account for the experimental observations.

5.6 REFERENCES

1. J. Enerhaug, S. L. Eliassen, P. E. Kvaale: *Corrosion/97*, paper no. 60, (Houston, TX: NACE International, 1997).
2. J. Enerhaug, P.E. Kvaale, M. Bjordal, J.M. Drugli, T. Rogne: *Corrosion/99*, paper no. 587, (Houston, TX: NACE International, 1999).
3. EFC publication no. 17, "Corrosion Resistant Alloys for Oil and Gas Production: *Guidance on General Requirements and Test Methods for H_2S Service*. The Institute of Materials, London, 1996.
4. S. Olsen, P. E. Kvaale, J. Enerhaug: *SUPERMARTENSITIC STAINLESS STEELS '99*, Brussels, Belgium, 1999, Belgian Welding Institute, Belgium, pp. 84-87.
5. J. Vagn Hansen, E. Maahn, P. Aastrup, P. F. Larsen: *Beskyttelsesgasdækning, og korrosionsbestandighed efter svejsning af rustfrie stålrør*. Report 87.66, Korrosjonssentralen ATV, Denmark, 1987.
6. P. Marcus, *Sulfur-Assisted Corrosion Mechanisms and the Role of Alloyed Elements*, ("Corrosion Mechanisms in Theory and Practice," P. Marcus and J. Oudar eds.), Marcus Dekker, 1995, pp. 239-263.
7. R. C. Newman, *Corrosion*, 1985, vol. 41, pp. 450-453.
8. S. Mat, R. Newman: *Corrosion/94*, paper no. 228, (Houston, TX: NACE International, 1994).

PART VI: A NEW APPROACH TO THE EVALUATION OF PITTING CORROSION OF SUPER MARTENSITIC WELDMENTS

6.1 INTRODUCTION

A major concern in the qualification and quality control of super martensitic stainless steel (SMSS) weldments for unprocessed well stream environment containing CO_2 and traces of H_2S (slightly sour conditions) has been the resistance to environmentally cracking (EC). The European Federation of Corrosion publication No. 17 (EFC 17)[1] has been adopted as a general guideline for the assessment of corrosion resistant alloys (CRAs) in sour service. EFC 17 is mainly concerned with EC, but stresses the importance of verifying an adequate general and localized corrosion resistance prior to performing EC tests[1]. As guidance, EFC 17 points out that the worst conditions for general and localized corrosion are those normally associated with the maximum service temperature. Thus, corrosion tests should be performed under such severe conditions.

The qualification of SMSS weldments for the Åsgard and Gullfaks Satellite field development projects[2,3] was accomplished in accordance with these principles[3] with H_2S partial pressures of 4-8mbar (i.e. Gullfaks) and 40mbar (i.e. Åsgard). Consequently, pitting tests were carried out at anticipated maximum service temperatures of 90-140°C, demonstrating adequate properties of the actual weldments[2,3]. Since pitting corrosion is not a major concern under the prevailing circumstances this has cleared the way for EC tests in the form of constant load (CL) and four-point bend (FPB) testing. EC tests soon showed, however, that the SMSS weldments were sensitive to general corrosion (experienced in simulated condensed water, 8mbar H_2S, *pH* 3.5-3.8, low $[Cl^-]$)[4,5] and to pitting corrosion (experienced in simulated formation water, 40mbar H_2S, *pH* 4.5-6, high $[Cl^-]$)[3] at ambient rather than at elevated temperatures. This contradicts the anticipated behavior of CRAs, thus indicating a subtle, new corrosion mechanism that most probably involves H_2S. Moreover, in agreement with the martensitic microstructure and with the nature of SSC, cracks occurred within regions characterized by active dissolution at ambient temperature, while no cracks were observed at the elevated temperatures.

The aim of the present chapter is to clarify why pitting occurs in SMSS weldments at ambient rather than at elevated temperatures and how this can be prevented. Moreover, results from a series of corrosion tests designed to examine the repassivation of “as-welded” root surfaces of SMSS weldments are included. Finally, some practical implications with respect to qualification of SMSS weldments for use are discussed.

6.2 EFFECT OF THE ROOT SURFACE CONDITION

It is well-known that welding of stainless steels modifies the nearby surface due to high temperature oxidation reactions, reducing the immediate chloride pitting resistance[6]. Hence, color maps representing various amounts of oxygen in the root shielding gas have been prepared to assert possible quality control of CRA weldments[6]. In piping and in vessels, pickling and grinding of the root surface are possible to restore acceptable passivity, whereas for flowlines, no post-weld treatment is possible and hence the "as-welded" surface must meet the actual requirements.

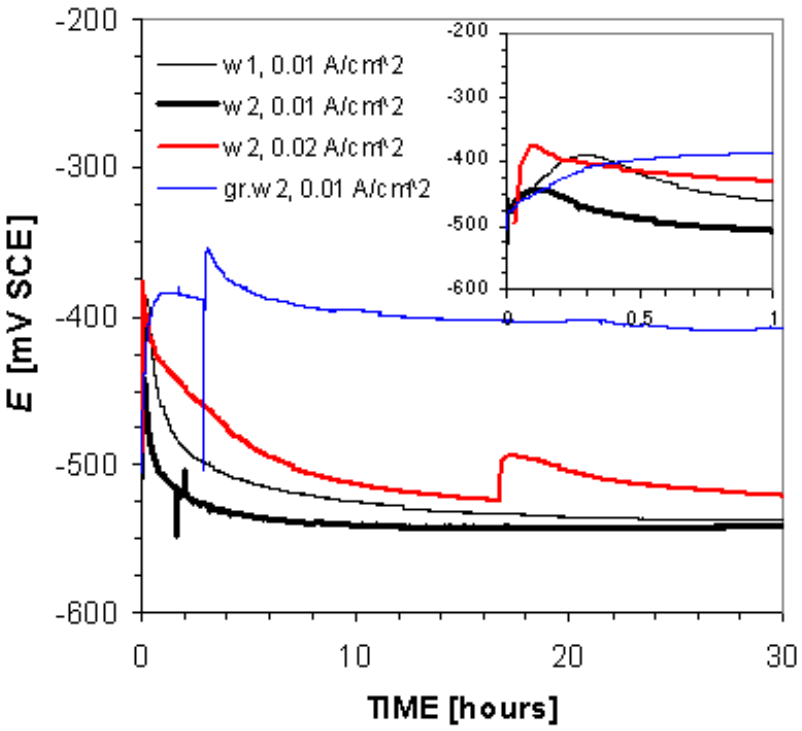

Figure 6.1. Summary of the results obtained in galvanostatic corrosion tests in 1m*M* H_2S (10mbar H_2S, 0.99mbar CO_2) in Part V. The three lowest transients represent the intact root surface of a 1-string weld, whereas the upper one represents the ground root surface.

Referring to the results obtained in Part V, there is a need to distinguish between chloride induced pitting occurring above, typically, –200mV SCE, and so-called S-induced dissolution (a term used by Marcus[7]) occurring locally in the region close to the fusion boundary even below –400mV SCE, depending on the root surface condition and on the H_2S content. Moreover, it was shown in Part II that the high temperature oxidations processes occurring during welding destroy the passivity of the region about 0-6mm from the fusion boundary, even at very low

oxygen potentials (i.e. 150ppm) in the root shielding gas. As a result of this, localized corrosion occurs at low potentials that are about −500mV SCE, referring to the results obtained in Part V. The main effect of H_2S seems to be to hinder repassivation by specific absorption of sulfur atoms and to accelerate corrosion occurring in the oxidized region close to the fusion boundary[7].

The results presented in Figure 6.1 shows potential transients from galvanostatic measurements of as-welded and ground SMSS root surfaces carried out in 1m*M* H_2S (10mbar H_2S, 0.99bar CO_2) in artificial formation water at ambient temperature in Part V. During these tests, localized attacks, corresponding to dissolution rates of 5 mm/year, occurred 0-3mm from the fusion boundary on the as-welded specimens, whereas no attacks occurred near the fusion boundary on the ground specimen. This test method is particularly suitable to disclose regions that are susceptible to pitting corrosion. These results show that pitting corrosion occurred at a very low potential (–400mV SCE) and high local dissolution rates even at –540mV SCE (assuming no IR-drop). They also show that surface modification by means of grinding prevents the occurrence of pitting in the weld region.

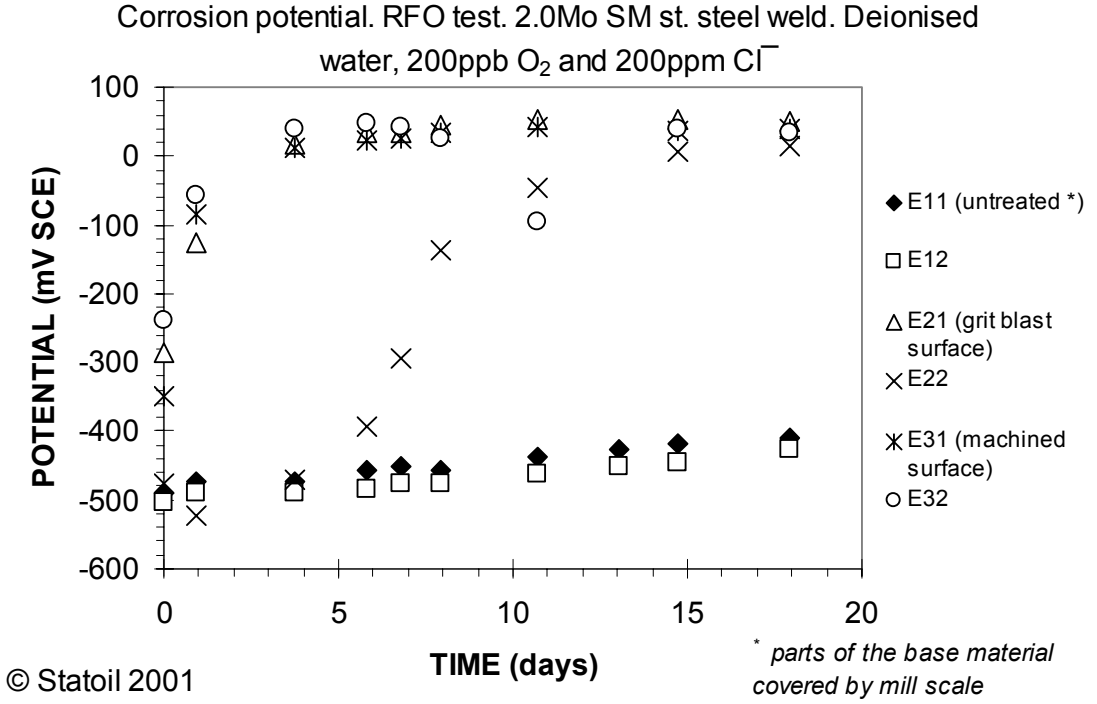

Figure 6.2. Open circuit potential transients from a test where the flowline commissioning was simulated by exposing SMSS weldments to deionised water with 200ppb O_2 and 200ppm Cl^-[8].

Moreover, there are observations supporting that as-welded SMSS root surfaces are modified and even fully passivated during initial exposure following commissioning and start up of the flowline. These issues must be sorted out in

order to understand the corrosion behavior of the weldments. The potential transients recorded during simulation of the commissioning of SMSS flowlines[8] are shown in Figure 6.2. In this test, the open circuit potential of as-welded, blast cleaned and machined SMSS root surfaces in fresh water with 200ppm O_2 at ambient temperature were measured over a period of 14 days. It appears from the gradually increase in the potential that the samples undergo a passivation process, and that the rate of passivation depends on the surface condition prior to exposure. Notice that the pipe surfaces adjacent to the weld region are covered with mill scale and that this, in turn, influences the potential transient.

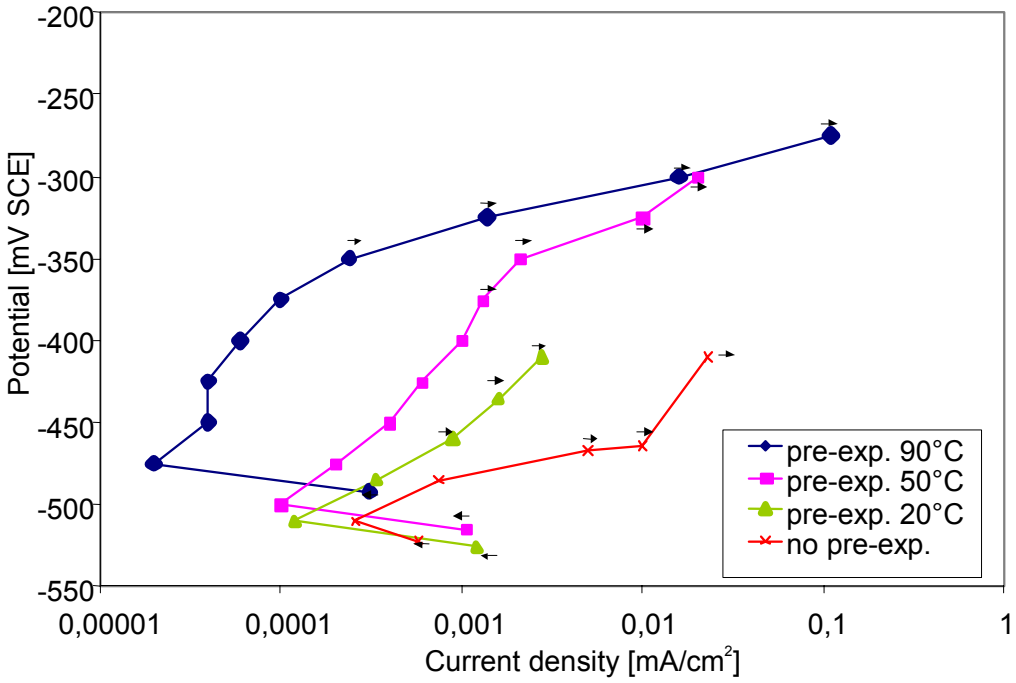

Figure 6.3. Pitting measurements carried out by Bjordal *et* al.[9]. 20°C, 30 000 ppm Cl^-, 100 mbar H_2S, scan rate 12.5mV/12 hour. The specimens had been pre-exposed for 48 hours in a CO_2 saturated solution at various temperatures prior to the pitting measurements.

Bjordal *et* al.[9] carried out potentiodynamic tests to assess the pitting susceptibility of SMSS weldments from the Åsgard project (pulsed GMA welding, duplex filler metal in the root pass). Prior to testing the weldments were exposed to different conditions simulating different start up situations with no H_2S present. The root surfaces were modified by pre-exposure to an oxidizing electrolyte (1 bar CO_2, formation water) for 48 hours at 20, 50 and 90°C, respectively. It appears from the results in Figure 6.3 that the pre-exposure increases the critical pitting potential during the subsequent testing in

10m*M* H_2S (100mbar H_2S, 0.9 bar CO_2) at ambient temperature, where the pre-exposure at the higher temperatures seems most favorable.

The results obtained in earlier investigations hence shows that the surface generated during the welding process, as a result of the high temperature oxidation, is characterized by high corrosion susceptibility. The corrosion properties seem to be significantly improved during exposure to electrolytes typically for the commissioning period. The higher corrosion susceptibility might therefore not be a problem for the use of these pipelines. It is, however, a problem during qualification of SMSS steel following the present EFC guidelines[3]. A study has therefore been undertaken to see if it is possible to define a test procedure that includes a defined and relevant weld surface.

6.3 EXPERIMENTAL PROCEDURE

6.3.1 Welding

The base material was received in the form of 10'' diameter seamless pipe from a Japanese steel manufacturer (Sumitomo) through the Åsgard Project. The wall thickness was 20mm and the pipe was delivered with pickled surfaces, using HNO_3 + HF and H_2SO_4. The steel chemical composition is shown in Table 6.1. The base composition of approximately 12%Cr, 2.5%Mo and 6.5%Ni places this pipe material in the "high alloyed" category of the SMSS.

Girth welds were made in a remotely controlled welding chamber, using the gas tungsten arc (GTA) welding process with pulsed current. A Ø1mm Thermanite 13/06 filler wire (produced by Böhler/Thyssen) was selected as welding consumable, which is a "high alloyed" wire developed for matching the SMSS base material, with chemical composition as given in Table 6.1.

Table 6.1. Chemical compositions of pipe material, filler wire and single root pass weld (in wt%).

	C	Cr	Mo	Ni	P	S	Si	Mn	V	Cu	W	Co	Al	Ti
Pipe	0.01	12.2	2.5	6.4	0.018	0.002	0.12	0.48	0.04	0.08	0.03	0.11	0.03	0.12
Wire	0.012	12.37	2.65	6.37	0.01	0.001	0.50	0.67						
Weld	0.011	12.2	2.7	6.5				0.49		0.06				

The two pipe ends to be joined were bevelled in a lathe machine, and the final groove joint geometry is shown in Figure 6.4. The root face (land thickness) was machined to 2.75 mm, and no joint misalignment between the pipes was allowed. The welding was performed with zero root gap. The pipe was rotated with the torch in a fixed position. The torch was located in the 11 o'clock position during root pass welding and 12 o'clock position for filler and cap

layers, i.e. the 1G position. The shielding gas composition was 70% helium, and 30% argon. No extra shielding gas was supplied from the bottom side of the weld, but the chamber was flushed with inert gas mixture before welding. Both single pass and full pass welds were produced, using the welding parameters listed in Table 6.2. The chemical composition of the former weld is given in Table 6.1. The oxygen content in the chamber was measured to be about 150ppm and 250ppm before deposition of root layer of the single pass weld and full weld, respectively.

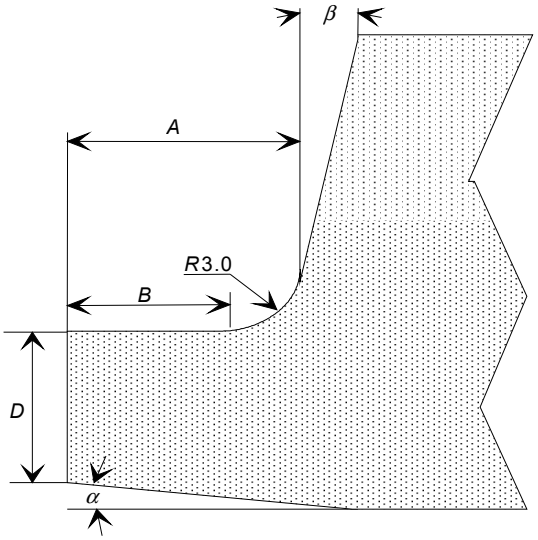

D= 2.75 ± 0.25 mm, B= 2.25 ± 0.2 mm,
A= 5.25 ± 0.3 mm, α= 6° and β= 7°

Figure 6.4. Schematic diagram showing the pipe bevel preparation.

Table 6.2. Summary of welding parameters of the 1-string weld (i.e. only root weld-layer) and the full weld (i.e. all layers).

Pass type	Welding current (I_p/I_b), [A]	Arc voltage [V]	Weaving amplitude [mm]	Weaving rate [mm/s]	Welding speed [mm/s]	Wire feed rate [m/min]	Dwell time on high pulse [ms]
Root weld	170/90	13	1.0	2.5	1.0	0.50	400
Bottom layer	200/100	13	3.0-3.25	6.0-6.5	1.0	0.90	500
Layers 1 and 2	210/110	13	3.0-3.25	6.0-6.5	1.0	1.3	500
Layers 3, 4, 5	220/120	13	2.75-3.5	5.5-7.0	1.0	1.3	500
Layers 6 and 7	220/120	13.5	1.0-4.5	2.0-9.0	1.0	1.3	500
Cap layer	220/120	14	6.0	6.0	1.0	1.55/0.75	400

6.3.2 Corrosion testing

The aim of the corrosion tests is to simulate and substantiate the repassivation of root surfaces of SMSS girth welds when they are exposed to fresh water (low in chloride and oxygen) during the commissioning (Ready for Operation - RFO) periods and to the well stream in the start up period before H_2S is present. In the first part of this survey, galvanostatic measurements were applied to simulate the oxidizing conditions at high (1*M* NaCl) or low (7m*M* Na_2SO_4) chloride levels. In the second part, the test solutions were saturated with 1 bar of gases that simulated either small amounts of oxygen during commissioning (1% O_2, rest N_2) or CO_2-corrosion during the start up of the flowline (100% CO_2). Seabed-like temperatures of 5±3°C were obtained by immersing the test cell in a water reservoir where the temperature was controlled by means of a heating element and "cold finger". In addition, some few measurements have been carried out in aerated 1*M* NaCl.

Table 6.3. Summary of experimental conditions in the corrosion tests.

Sample	Weld	Root surface condition	Measuring method	Test solution
A	Full weld	As-welded	Galvanostatic	Deaerated, 1*M* NaCl
B	1-string weld	As-welded	Galvanostatic	Deaerated, 1*M* NaCl
C	1-string weld	Ground	Galvanostatic	Deaerated, 1*M* NaCl
D	Full weld	Ground	Galvanostatic	Deaerated, 7m*M* Na_2SO_4
E	Full weld	As-welded	Galvanostatic	Deaerated, 7m*M* Na_2SO_4
F	Full weld	As-welded	Free exposure	1%O_2, 7m*M* Na_2SO_4
G	Full weld	As-welded	Free exposure	1%O_2, 7m*M* Na_2SO_4 at 5°C
H	Full weld	As-welded	Free exposure	CO_2, 7m*M* Na_2SO_4
I	1-string weld	As-welded	Free exposure	Air-saturated, 1*M* NaCl

Each specimen was taken from the actual weldment, and prior to the measurement the side edges apart from the intact root surface were cut and ground with a 1000 grit paper, and a hole was drilled for the connection of a platinum wire. Moreover, the specimen was mounted in 2-litre glass cell and electrically connected to the measuring unit. A saturated calomel electrode (SCE) was used as a reference electrode, while a platinum wire served as counter electrode. Details about the test conditions are given in Table 6.3.

Prior to each test the solution was purged with N_2 gas for more than 6 hours before the specimens were immersed into the solution. As the potential stabilized at a certain level below −650mV SCE, the galvanostat was switched on, or alternatively, the solution was saturated with the actual reactive gas. A Solatron SI 1286 unit, controlled by an in-house PC program, was used to carry out the galvanostatic measurements in 1*M* NaCl at $i = 0.8\mu A/cm^2$. Similarly, a Wenking test unit was used for the galvanostatic measurements in 7m*M* Na_2SO_4

at i = 1μA/cm^2. The free exposure tests were accompanied by galvanostatic measurements in order to verify that full repassivation is achieved in the first part of the test.

6.4 RESULTS AND DISCUSSION

6.4.1 Corrosion tests

6.4.1.1 Galvanostatic measurements

The different samples and test conditions employed are summarized in Table 6.3. Notice that in samples (C) and (E) the surface oxide was removed by grinding prior to testing. Figure 6.5 (a) shows the characteristic evolution of the potential with time during the galvanostatic measurements.

Initially, the open circuit potential decreased to values below −650mV SCE within a few hours of the free exposure period. Subsequently, as the galvanostat was switched on a passivation process took place, characterized by an increase in potential that levelled off to some sort of a plateau value after a few minutes. Eventually, the potential began to increase again until the value exceeded the chloride dependent pitting potential when rapid fluctuations of the potential was observed (not shown in the figure). A closer inspection of Figure 6.5 (a) reveals that the passivation process occurs slower on the oxidized root weld surfaces compared with the ground surfaces. This follows from a comparison between the curves representing the ground 1-string weld specimen (C) and the intact 1-string weld specimen (B) in a 1*M* NaCl solution and the ground full weld specimen (D) and the intact full weld specimen (E) in a 7m*M* Na_2SO_4 solution. The difference in chloride level is not found to have any effect.

The results show that the “as-welded” root surfaces are modified and eventually passivated as they are introduced into oxidizing solutions. The impressed current densities applied in the tests (i.e. about 1μA/cm^2) correspond to the passive current measured under similar conditions in Part IV and the measurements are therefore believed to represent realistic simulations of the flowlines when they are filled with fresh water (low in chloride) during commissioning or in the starting up period (high in chloride) before the wells produce any H_2S. The tendency to repassivation is further investigated in the following free exposure tests.

(a)

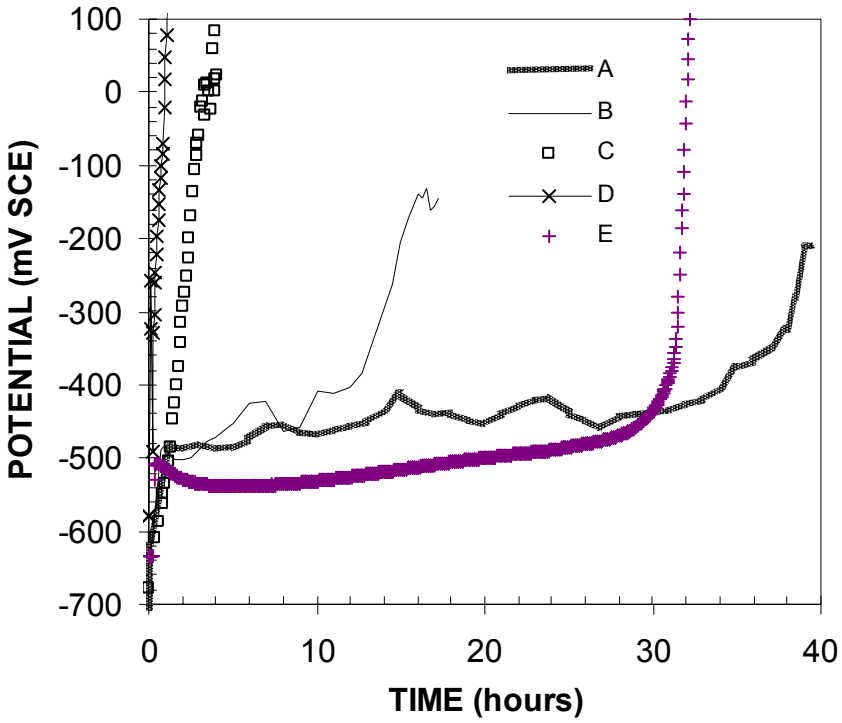

(b)

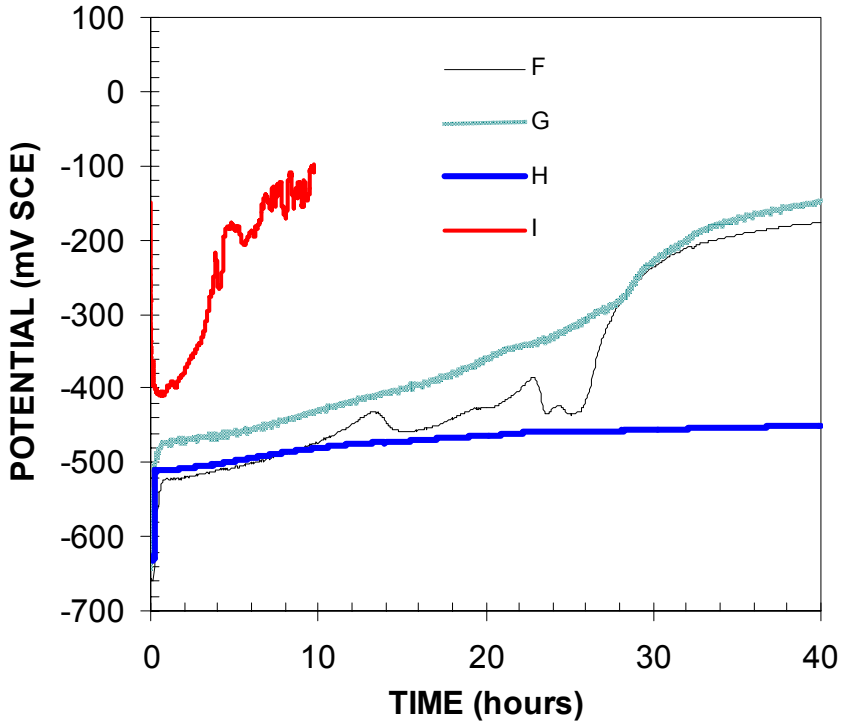

(c)

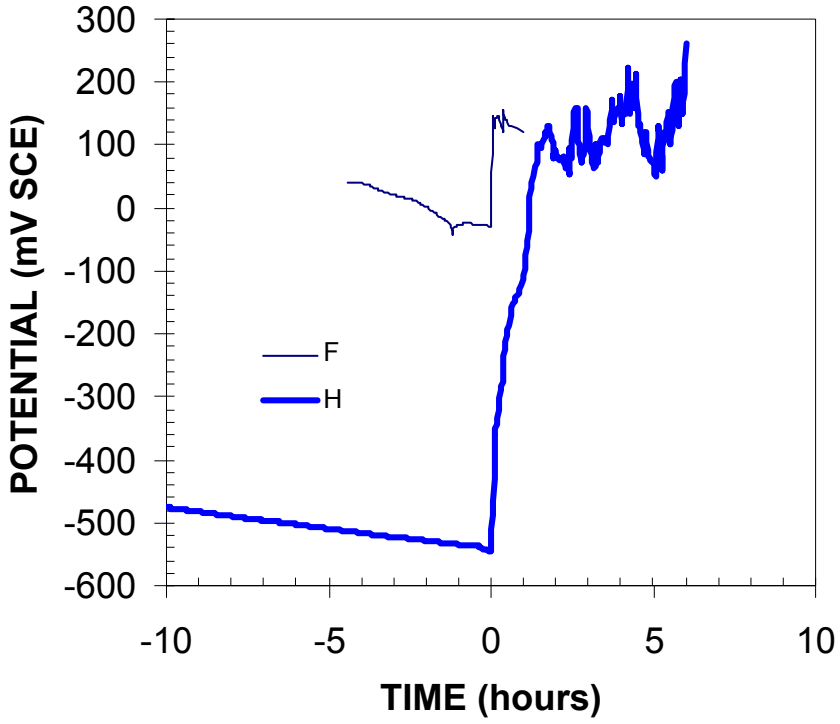

Figure 6.5. Summary of the results obtained in the (a) galvanostatic corrosion tests and (b) the free exposure tests, respectively, in 1*M* NaCl and 7m*M* Na_2SO_4. The experimental conditions are defined in Table 6.3. Figure (c) shows the potential transients for specimens F and G as the galvanostat was turned on (i.e. 0 hours in the figure) after about 290 hours of free exposure in the actual test solutions and a following nitrogen purging (i.e. for some hours).

6.4.1.2 Free exposure

The different samples and test conditions employed are summarized in Table 6.3. The free-exposure potential transients are summarized in Figure 6.5 (b). Generally, the potential transients display the characteristics of a repassivation process and bear a close resemblance to the galvanostatic transients in Figure 6.5 (a).

In the 1% O_2 solutions the potential first increased rapidly as the solution was saturated with the actual gas mixture and then started to level off until some sort of plateau was reached after a few minutes. Subsequently, the potential increased steadily until it increased rapidly and finally levelled off at about –200mV SCE approaching the upper limit potential. There was no significant difference between the results obtained at 22°C (F) and 5°C (G), and the subsequent galvanostatic measurement demonstrated that the samples were fully

passivated during the exposure, as shown in Figure 6.5 (c) for sample (G), which had been subjected to about 290 hours of exposure. This figure shows that the potential immediately increased to a pitting potential at about 100mV SCE as the galvanostat was turned on.

In the test where the solution was saturated with CO_2 gas (H) the potential stabilized at about −470mV SCE and remained constant throughout the free exposure (i.e. for about 290 hours), demonstrating a lower oxidizing power compared to 1%O_2. The subsequent galvanostatic measurement shown in Figure 6.5 (c) demonstrated that the sample was fully passivated during the exposure, inasmuch as the potential immediately increased to a pitting potential at about 100mV SCE as the galvanostat was turned on.

Finally, for the specimen that were immersed directly in the aerated solution (I), the potential decreased to a sort of plateau in half an hour at −350 to −400mV SCE, before it increased and exceeded −200mV SCE in 4-5 hours, proving that the increased oxidized power enhanced the passivation process.

6.5 CONCLUSIONS

Test results from earlier investigations show that root surfaces of SMSS weldments are not fully passive in the as-welded condition. It appears that high temperature oxidation during welding determines the surface condition of the root surface. This region is therefore particularly vulnerable for S-induced pitting corrosion. Specifically adsorbed sulfur atoms from dissolved H_2S molecules are believed to hinder repassivation and accelerate active dissolution.

The present results indicate that the root surface may repassivate during the commissioning period and the start up period of the flowline.

The previously underestimated effect of the root surface as regards localized corrosion in slightly sour service brings in a great uncertainty in the standard environmentally cracking tests. Rather than testing the soundness of the weld it might end being a test of minor differences in the applied root shielding gas. A consequence is it a great difficulty in validating the actual weldments and in performing any optimisation of the welding parameters apart from the root shielding gas. The relevancy of the test may also be questioned. It may also be difficult to obtain reproducible results.

Results from previous studies substantiate that there is a relationship between the repassivation and the temperature of the test solution. This is a possible explanation of why the SMSS weldments are found to be more corrosion resistant at elevated temperatures.

Based on the present findings, it is proposed to include surface modification in all corrosion tests used for qualification of SMSS weldments. The new test procedure should be based on the common knowledge about the environmental conditions prior to exposure to H_2S.

6.6 REFERENCES

1. EFC publication no. 17: *Corrosion Resistant Alloys for Oil and Gas Production: Guidance on General Requirements and Test Methods for H_2S Service*. The Institute of Materials, London, 1996.
2. J. Enerhaug, S. L. Eliassen, P. E. Kvaale: *Corrosion/97*, paper no. 60, (Houston, TX: NACE International, 1997).
3. J. Enerhaug, P. E. Kvaale, M. Bjordal, J. M. Drugli, T. Rogne: *Corrosion/99*, paper no. 587, (Houston, TX: NACE International, 1999).
4. J. M. Drugli, T. Rogne, M. Svenning, S. Axelsen, J. Enerhaug *SUPERMARTENSITIC STAINLESS STEELS '99*, Brussels, Belgium, 1999, Belgian Welding Institute, Belgium, pp. 315-322.
5. M. Pourbaix, *Corrosion*, 1970, vol. 26, pp. 431-438.
6. J. Vagn Hansen, E. Maahn, P. Aastrup, P. F. Larsen: *Beskyttelsesgasdækning, og korrosionsbestandighed efter svejsning af rustfrie stålrør*, Report 87.66, Korrosjonssentralen ATV, Denmark, 1987.
7. P. Marcus: *Sulfur-Assisted Corrosion Mechanisms and the Role of Alloyed Elements*. ("Corrosion Mechanisms in Theory and Practice", P. Marcus and J. Oudar eds.). Marcus Dekker, 1995, pp. 239-263.
8. Unpublished data from the Åsgard Field Development Project (1997).
9. M. Bjordal, J. M. Drugli, N.I. Nilsen: *Study of corrosion properties of alloyed 13%Cr stainless steel*. SINTEF report STF24 F00234. Trondheim, 2000.